Veronika Preissegger, BSc

# Crystal chemistry and solubility of C-A-S-H gels bearing $Co^{2+}$, $Cu^{2+}$ and $Zn^{2+}$: An experimental approach

MASTER'S THESIS

to achieve the university degree of

Master of Science

Master's degree programme: Earth Sciences

submitted to

Graz University of Technology

Supervisor

Dr.rer.nat. M.Sc., Andre Baldermann

Institute of Applied Geosciences

Graz, January 2020

# AFFIDAVIT

I declare that I have authored this thesis independently, that I have not used other than the declared sources/resources, and that I have explicitly indicated all material which has been quoted either literally or by content from the sources used. The text document uploaded to TUGRAZonline is identical to the present master‘s thesis.

| | |
|---|---|
| Date | Signature |

This work is dedicated to

Andrea & Franz

and

Matthias, Georg, Michaela & Benedikt.

## Table of content

1. Abstract ........ 1
1. Introduction ........ 3
2. C-(A)-S-H structures – a digression ........ 5
3. Experimental and Analytical Methods ........ 9
    3.1. Experimental ........ 9
    3.2. Analytical Methods ........ 11
        3.2.1. Liquid phase characterization ........ 11
        3.2.2. Solid phase characterization ........ 12
4. Results ........ 15
    4.1. Evolution of the aqueous solution during (Me)-C-A-S-H gel precipitation ........ 15
    4.2. Solid phase characterization ........ 18
        4.2.1. Macroscopic description of precipitates ........ 18
        4.2.2. Mineralogy of precipitates (XRD and FTIR) ........ 19
        4.2.3. Water content of precipitates ........ 24
        4.2.4. Shape and crystal chemistry of precipitates ........ 27
5. Discussion ........ 31
    5.1. Precipitant mineralogy versus solution chemistry ........ 31
    5.2. Crystal chemistry of (Me)-C-A-S-H gels ........ 33
    5.3. Solubility of Me-substituted C-A-S-H ........ 39
    5.4. Me-C-A-S-H phases in waste management technologies ........ 42
6. Acknowledgement ........ 45
7. References ........ 46
8. Table of figures ........ 52
9. List of tables ........ 54
10. Appendix ........ 55

## Abbreviations

| | |
|---|---|
| $a_x$ | Activity of substance x in solution |
| A/S-TEM | Analytical and Scanning Transmission Electron Microscopy |
| Atc | Atacamite |
| ATR | Attenuated Total Reflection |
| CBS | Circular Back Scattered Electron |
| Cc | Calcite |
| C-S-H | Calcium-Aluminium-Silicate-Hydrate |
| DSC | Differential Scanning Calorimetry |
| EC | Electric Conductivity |
| EDS | Energy Dispersive X-ray Spectroscopy |
| EDX | Energy Dispersive X-ray |
| EELS | Electron Energy Loss Spectroscopy Spectra |
| EFTEM | Energy Filtered Transmission Electron Microscopy |
| ESEM | Environmental Scanning Electron Microscopy |
| FEG | Field Emission Gun |
| FELMI-ZFE | Institute for Electron Microscopy and Nanoanalysis and Center for Electron Microscopy |
| FFT | Fast Fourier Transform |
| FTIR | Fourier Transform Infrared |
| GIF | Gatan Imaging Filter |
| HAADF | High Angle Annular dark field |
| HV | High Vacuum |
| IAG | Institute of Applied Geosciences |
| ICP-OES | Inductively Coupled Plasma Optical Emission Spectroscopy |
| $K_{SP}$ | Solubility Constant |
| LFD | Large Filter Detector |
| LV | Low Vacuum |
| Me | Heavy metal |
| Me0.1 | The respective heavy metal and the initial molar Me/Si ratio |
| MHC | Monohydrocalcite |
| MSWI | Municipal Solid Waste Incineration |
| NIR-MIR | Near- to Mid-Infrared |
| NMR | Nuclear Magnetic Resonance |
| p.a. | Pro analysi |
| Paratc | Paratacamite |
| $Q_x$ | Silicon tetrahedron sharing *x* oxygen atom (b=bridging, p=pairing) |
| Ref_filtr | Reference material – filtrated |
| Ref_zentr | Reference material – centrifuged |
| SCMs | Supplementary Cementitious Materials |
| SI | Saturation Index |
| S/S | Solidification/Stabilization |
| SSAS | Solid Solution in Aqueous Solution |
| STA | Simultaneous Thermal Analysis |
| STEM | Scanning Transmission Electron Microscopy |
| T | Temperature |
| TEM | Transmission Electron Microscopy |
| TGA | Thermogravimetric Analysis |
| XRD | X-ray Diffraction |

# 1. Abstract

Heavy metal ions (Me: Co, Cu, Zn) bearing calcium aluminium silicate hydrate (C-A-S-H) gels were synthesized by the sol-gel method using Me/Si molar ratios from zero up to 0.6 and a constant Al/Si molar ratio of 0.05 at 23 ± 1 °C. The chemical key characteristics of the reactive fluid (i.e. pH, EC, T and solute concentration) were monitored over a reaction time of 1 hour. At the beginning, the reactive fluid was strongly oversaturated with respect to a jennite-type C-(A)-S-H phase changing to a tobermorite-type C-(A)-S-H phase at equilibrium conditions, which were established after 10-30 minutes. After termination of the short-term experiments (1 hour) the precipitates were analysed for their mineralogy, structure, water content and geochemical composition by XRD, FTIR, ESEM, TEM and STA methods. The threshold for $Co^{2+}$ and $Cu^{2+}$ incorporation in C-A-S-H gels was reached at an initial molar Me/Si ratio of about 0.3 and for $Zn^{2+}$ at approximately 0.6 or even higher. At molar ratios > 0.3, other Me-bearing minerals formed beside Me-C-A-S-H, such as atacamite (Cu-series) and potentially poorly crystallized Co-hydroxides (Co-series). The Zn-series yielded no discrete reaction by-products bearing Zn. From the experimental data obtained in this study it can be concluded that the respective Me ions preferentially substitute for $Ca^{2+}$ in the C-A-S-H structure, having molar (Me+Ca)/(Al+Si) ratios in the range from 0.88 to 1.03. The structural water content of pure C-A-S-H is about 17 wt.%, similar to published values, but it tends to be higher in Me- C- A- S- H as the Me content increases (18-24 wt.%). From these data, solubility constants ($K_{SP}$) for the precipitated (Me)-C-A-S-H gels were calculated. It is evident that the $K_{SP}$ for Me bearing C-A-S-H is significantly lower compared to the pure C-A-S-H phase. The log$K_{SP}$ values are in the order of -8.6 to -11.3 for the Co-series, -9.1 to -11.6 for the Cu-series and -8.9 to -14.1 for the Zn-series, while pure C-A-S-H has a log$K_{SP}$ of -8.3. This indicates that newly formed C-A-S-H gels have a high immobilization potential for Me - and also Ca, Si, and Al - under alkaline conditions, which is highly relevant for example in wastewater treatment, toxic waste stabilization and assessment of nuclear waste repositories.

## Zusammenfassung

Die schwermetalldotierten (Me: Co, Cu, Zn) Calcium Aluminium Silicate Hydrat Syntheseprodukte C-A-S-H wurden mit der Sol-Gel Methode bei 23 ± 1 °C generiert, wobei initiale molare Me/Si Verhältnisse von null bis 0.6 mit einem konstanten molaren Al/Si Verhältnis von 0.05 vorgegeben wurden. Während des Reaktionsfortschritts in den Experimenten wurden chemische wie physikalische Parameter (d.h. pH, EC, T und gelöste

Ionenkonzentration) der wässrigen Lösung über einen Zeitraum von einer Stunde fortlaufend erfasst. Am Beginn der jeweiligen Experimente konnte eine Übersättigung an einer Jennit-ähnlichen C-(A)-S-H Phase festgestellt werden, während bei Annäherung an das chemische Gleichgewicht eine Tobermorit-ähnliche Struktur stabiler erschien. Ein annähernd chemisches Gleichgewicht zwischen der Festphase und Lösung stellte sich nach rund 10-30 Minuten ein. Beendet wurden die Kurzzeitexperimente nach jeweils einer Stunde, woraufhin die mineralogische, strukturelle und geochemische Zusammensetzung sowie der Wassergehalt der Präzipitate mittels XRD, FTIR, ESEM, TEM und STA bestimmt wurde. Die Ergebnisse zeigen, dass die Grenzwerte für den Einbau von $Co^{2+}$ und $Cu^{2+}$ in C-A-S-H Gelen bei einem initialen molaren Me/Si Verhältnissen von 0,3 erreicht wurden. Für $Zn^{2+}$ liegt der Wert bei 0.6 oder sogar höher. Bei einem höheren Me/Si Wert kommt es zur Präzipitation zusätzlicher Festphasen, wie z. B. Atacamit (Cu-Serie) und womöglich schlecht kristallines Co-Hydroxid (Co-Serie). Die Zn-Serie zeigt keine Kopräzipitate. Die Substitution von $Ca^{2+}$ trägt dominant zur Fixierung von $Co^{2+}$, $Cu^{2+}$ und $Zn^{2+}$ in den C-A-S-H Strukturen bei, da in dieser Studie mit höherer Me-Konzentration im Feststoff ein Anstieg in gelöstem $Ca^{2+}$ einhergeht. Die errechneten molaren (Me+Ca)/(Al+Si) Verhältnisse liegen zwischen 0.88 und 1.03. Die ermittelten Werte des strukturell gebundenen Wassers ergeben für Me-C-A-S-H tendenziell höhere Werte (~18-24 Gew.%) als für reine C-A-S-H Phasen (~17 Gew.%). Anhand der experimentellen Daten wurden die Löslichkeitskonstanten ($K_{SP}$) der gebildeten (Me)-C-A-S-H Phasen ermittelt. Hierbei ergaben sich deutlich geringere Löslichkeiten im Vergleich zu reinem C-(A)-S-H. Die $\log K_{SP}$ liegen innerhalb der Co-Serie im Bereich von -8.6 bis -11.3, für die Cu-Serie im Bereich von -9.1 bis -11.6 und für die Cu-Serie im Bereich von -8.9 bis -14.1, während reines C-A-S-H einen $\log K_{SP}$ von -8.3 aufweist. Die vorliegende Studie zeigt, dass C-A-S-H Gele in der Lage sind Schwermetalle – und auch Ca, Si und Al – unter alkalinen Bedingungen zu immobilisieren, was zum Beispiel relevant ist in der Abwasserbehandlung, der Stabilisierung toxischer Abfälle und in der Endlagerdebatte von atomaren Abfällen.

## 1. Introduction

Calcium silicate hydrate (C-S-H) is a main constituent and important hydraulic binding agent in hydrated Portland cement-based concrete [1], which is the most important construction material in recent times [2]. Besides its widespread and multi-faceted application in building industry, cement-based materials have nowadays been used for the treatment of wastewater [3]-[6] and acid mine drainage solutions [7], [8] as well as for toxic waste stabilization [7], [9]-[14] and installation of confinement barriers in radioactive waste disposal sites [15]-[17]. In times of an increasing demand of construction materials on the one hand [18]-[21], and the awareness of needs for global warming reduction and appropriate handling of limited natural resources on the other hand, the utilization of alternative, eco-friendly and sustainable cement-based materials is becoming increasingly more important [1]. However, newly developed cement mixes are often enriched in distinct heavy metals (Me: e.g., Zn, Pb, Cr, and Fe among others), compared to ordinary Portland cement, because supplementary cementitious materials (SCMs) added to the cement, such as municipal solid waste incineration (MSWI), fly ash, granulated blast furnace slag, industrial waste materials, silica fume and limestone/dolostone powder, frequently contain higher Me contents than the raw materials originally used for cement production [1], [22]-[24]. Such higher Me dosages in construction materials could, if released to the environment and not properly monitored, become a potential risk for the aquatic and terrestrial ecosystems and thus for human health.

However, concrete and/or cementitious materials are not only confronted with currently increasing Me loads derived from cement production or concrete manufacturing. The contact of concrete with Me-bearing aqueous solutions [5] or contaminated sediments, soils and rocks [7] may also induce severe environmental problems, as the mobilization, transportation and sequestration mechanisms of Me at the concrete-water interface are still hotly debated in the scientific literature and by far not fully understood. Thus, advanced knowledge about the fate of Me during the hydration, hardening and subsequent alteration of concrete under various environmental conditions is an issue of strongly increasing relevance [1],[25]. In this light, several research studies have been conducted with the focus on elucidating the mineralogical and crystal-chemical mechanisms and the underlying physicochemical conditions controlling Me immobilization and/or incorporation in natural and synthetic C-(A-)S-H structures [1], [26]-[29]. Very recently, Baldermann et al. [26] conducted a systematic co-precipitation study, which dealt with the fixation of different Me, such as Co, Cr and Zn, in synthetic C-(A)-S-H phases, by considering the effects of different initial molar ratios of Ca/(Si+Al) (0.6–

1.6) and Me/Si (0.0–2.0) at constant Al/Si ratio (0.05). They figured out that in the absence of Me (Me/Si = 0) and at low (Me/Si = 0.02) to intermediate (Me/Si = 0.2) concentrations of Me in solution, a 14 Å tobermorite-like material with a defect structure is formed, similar to poorly evolved C-A-S-H gels. However, the degree of polymerization of C-A-S-H was found to generally decrease with increasing loads of Me, which indicates that Ca substitution by Me changes the C-A-S-H structure. Finally, at a molar Me/Si ratio of 2.0, either trioctahedral Co- and Zn-smectite-type mineral phases or a X-ray amorphous Cr-gel formed [26], denoting the transition from C-A-S-H to clay minerals or completely distorted (gel-like) structures. However, based on these limited experimental datasets the threshold for Me incorporation in C-A-S-H phases could not be reasonably resolved, meaning that the crystal chemistry, thermodynamic properties and (meta)stability of these Me-bearing C-A-S-H phases still remain poorly constrained, which calls for further experimental studies on this topic.

Therefore, in extension to the work of Baldermann et al. [26], this study aims to further investigate the threshold and mechanism(s) of Me incorporation in synthetic C-A-S-H gels, utilizing Co, Cu and Zn. Wet-chemical, mineralogical, geochemical, micro-/nano-structural and thermo-analytical techniques were applied to trace and assess the progress of structural incorporation (e.g. via isomorphous substitution) of Me in precipitating C-A-S-H versus co-precipitation of other Me-bearing mineral phases. Based on these novel experimental datasets solubility properties of the Me-doted C-A-S-H gels are calculated, and the environmental implications of Me incorporation in natural and synthetic C-A-S-H phases are discussed.

## 2. C-(A)-S-H structures – a digression

Several mineral phases exist within the CaO – $SiO_2$ – $H_2O$ system (see Figure 1), being of natural and/or technical relevance [1]. Many efforts have been undertaken in order to resolve the nature of C-S-H and its gel-like precursor substances, as these materials are well known to take a key role in the hydration process of cement and as they are responsible for the physical, chemical and mechanical performance of the hardened cement paste [30]-[38].

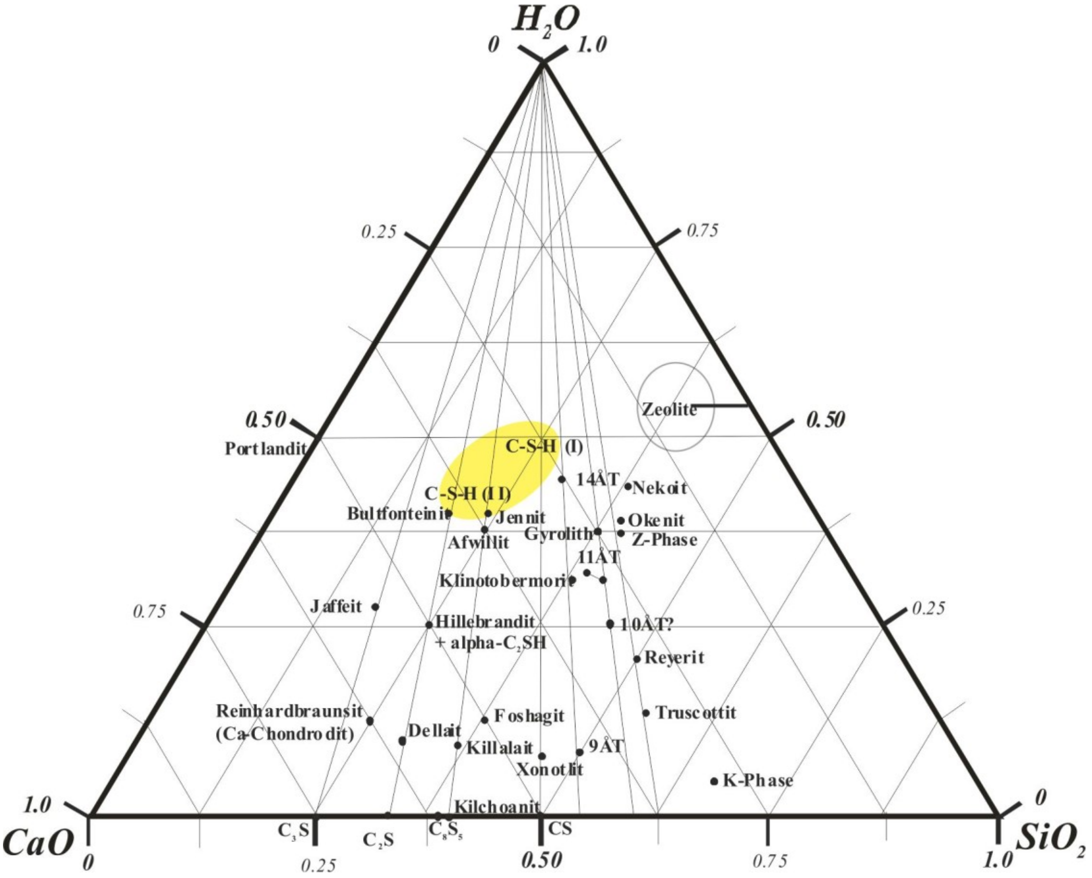

Figure 1: Mineral phases in the ternary system CaO, $H_2O$ and $SiO_2$ modified after [39]. The yellow area marks the predominance field of C-S-H structures.

Generally, C-S-H gel is a poorly crystalline substance, compared to its more evolved C-S-H (I) (0.75<Ca/Si<1.5), C-S-H (II) (Ca/Si>1,5) and tobermorite-type (Ca/Si = 0.83) counterparts [30], which exhibit a more cross-linked structure and thus a higher degree of structural order. To resolve crystal-chemical details of such overall poorly ordered materials, nuclear magnetic resonance (NMR) spectroscopy has been proven to be an useful tool [31], [38]. It was found that Si atoms mainly occupy $Q_1$ and $Q_2$ positions, resulting into a sheet-like structure, which is very often referred to as “dreierketten chain” [40]. Some Si and also Al in tetrahedral sites are bound further in a $Q_3$ position, that is, a structural element, which cross-links adjacent silicate chains to form a more polymerized network (see Fig. 2) [41]. A conceptual structural model for C-S-H gels (at an atomic scale) was found to resemble that of 14 Å tobermorite $[Ca_5(Si_60_{18}H_2) \bullet 8H_2\ O]$ at Ca/Si molar ratios from 0.55-0.65 to 1.0 and of jennite $[Ca_9(Si_6O_{18}H_2)(OH)_8 \bullet 6H_2O]$ at a Ca/Si molar ratio between 1.1 and 1.5-1.65, respectively [31], [37]. While older studies preferred a jennite-type structural model or a mixture of tobermorite- and jennite-type structural sites to explain the complex crystal structure of C-S-H gels [42], Cong and Kirkpatrick (1996) proposed a 'defect tobermorite model' instead [40].

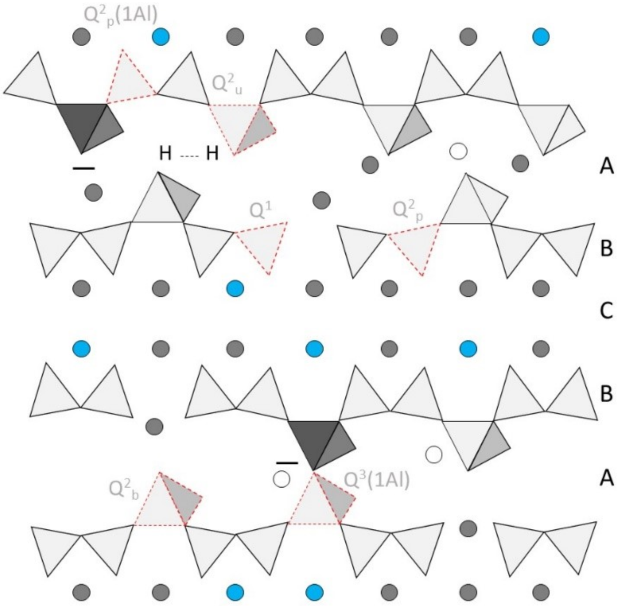

Figure 2: Structural model of C-A-S-H gels adapted from [26] and [43]. A = interlayer; B = 'dreierketten' chain; C = CaO sheet; $Q^1$ = silicon tetrahedron sharing one oxygen atom; $Q^2$ = silicon tetrahedron sharing two oxygen atoms; $Q^3$ = silicon tetrahedron sharing three oxygen atoms; b = bridging; p = pairing; (1Al) = silicon in tetrahedral coordination neighboring an aluminium occupied tetrahedron; blue circles = possible isomorphic substitution of $Ca^{2+}$ ions by heavy metals (Me); grey circles = $Ca^{2+}$ in CaO layer; blanc circles = molecular / interlayer water.

In natural surroundings, tobermorite forms through hydrothermal processes or metasomatic overprinting of basic rock types, but also in the contact zone of limestone and magmatic plutons [35], [44]. Dependent on the hydration degree, clino-tobermorite as well as 9 Å, 10 Å, 11 Å and 14 Å tobermorite can be distinguished [30], [44], [45]. The basic characteristic of the tobermorite group minerals (see Figure 2) is the CaO-layer, which is connected to the adjacent wollastonite-type 'dreiereinfachketten' [1]. These dreierketten chains consist of Si in tetrahedral coordination, whereby individual tetrahedrons can be assigned to pairing (p) or bridging (b) positions [38]. As for C-S-H gels and the defect tobermorite model, 14 Å tobermorite lacks of bridging positions [i.e. $Q_2$(b) is vastly lacking], which leads to the de-polymerization of the tetrahedral network and thus structural disorder. The higher the Ca/Si molar ratio the more $Q_2$(b) positions are omitted [40]. C-S-H gel (as a single phase) is limited to solid Ca/Si molar ratios from about 0.55 to 1.65 [37]: at lower or higher ratios amorphous silica and portlandite will start to co-precipitate [40], [46]. Beside the Ca/Si molar ratio, also the temperature is of great relevance for C-S-H phase formation. At higher temperatures (e.g. 70 °C to 140 °C) crystalline tobermorite with a reduced water content is the dominant phase, whereas at < 70 °C highly disordered and fully hydrated C-S-H gel forms, given that the Ca/Si molar ratio stays close to 1 (see Figure 3) [30], [35].

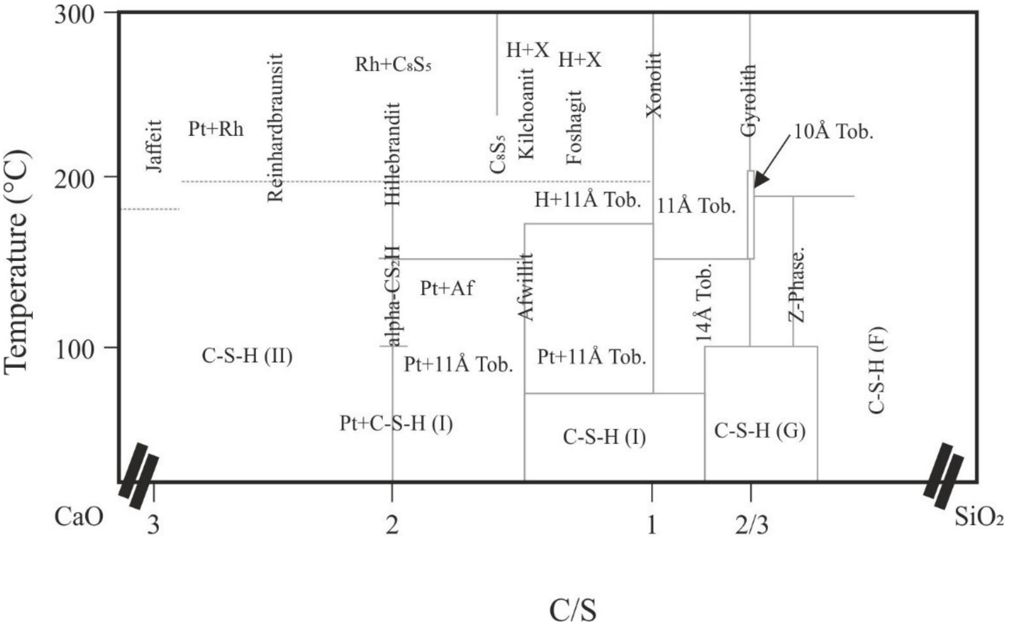

Figure 3: Predominance fields of C-S-H phases with varying Ca/Si (C/S) molar ratio and temperature (adapted from [39]). Pt = Portlandite; RH = Reinhardbrausite; H = $H_2O$; X = Xenolite.

More recently, the incorporation of cations other than $Ca^{2+}$, such as $Mg^{2+}$, $Al^{3+}$, $Na^+$ and $K^+$, in C-S-H structures has gained awareness due to its application in cement industry, i.e. M-A-S-H and N-A-S-H phases have been introduced, where M and N denote structural bound Mg and Na, respectively [43], [46] – [48]. Aluminium preferentially substitutes for Si in the tetrahedral site of a bridging position, but it can also be present in other positions, like the interlayer site [43]. At low Al concentrations (≤ 0.05), C-A-S-H forms without any co-precipitates, however, the interlayer thickness rises from about 11.9 Å to 12.7 Å in the presence of hydrated Al-complexes [43]. Furthermore, polymerization of C-S-H is enhanced in the presence of Al, whereas the incorporation of $K^+$ in the interlayer leads to a structural degradation [43]. Apart from these common substituents, the incorporation of Me (Co, Cr and Zn among many others) in C-S-H and C-A-S-H structures and the structural site occupancy are still a matter of intense debate [26], [49]. Baldermann et al. [26] observed the formation of tobermorite-like structures with incorporated Me at Me/Si molar ratios of ≤ 0.2 and proposed that Me uptake by C-A-S-H follows a combination of isomorphous substitution in the CaO layer, ion exchange in the interlayer sites and surface (ad)sorption and surface precipitation [26]. Independent evidence for significant incorporation of $Zn^{2+}$ into the interlayer of C-S-H phases is given by Ziegler et al. [49]. Zhao et al. [50] investigated the adsorption mechanism of Cr(VI) by C-A-S-H structures, which were synthesised at 180 °C and argued that Cr adsorption onto the tobermorite surface is followed by Cr absorption via exchange reactions with $Ca^{2+}$, but also the complexation with the O atoms of bridging tetrahedrons may be important [50]. Very recently, Mancini et al. (2019) have demonstrated that (i) $Fe^{3+}$ is strongly sorbed into the C-S-H structure, (ii) $Fe^{3+}$ occupies the interlayer with an octahedral geometry, if the Ca/Si ratio is high and (iii) $Fe^{3+}$-rich phases precipitate on the surface of C-S-H, if the Ca/Si ratio is low, also suggesting that the immobilization mechanisms of Me in contact with C-S-H and C-A-S-H phases are rather complex.

## 3. Experimental and Analytical Methods

### 3.1. Experimental

The synthesis of the Me-doped C-A-S-H gel phases was performed via a sol-gel process (see Figure 4), following the experimental protocol reported in Baldermann et al. [25]. Therefore, a 100 mmol/l $Si(OH)_4$ stock solution was prepared from the dissolution of sodium-metasilicate-pentahydrate ($Na_2SiO_3 \cdot 5H_2O$, p.a. from Roth, Karlsruhe, Germany) in ultrapure water (Milli-Q Plus UV, 18.2 MΩ at 25 °C). In order to prevent the $Si(OH)_4$ stock solution from carbon dioxide ($CO_2$) absorption, bubbling with $N_2$ gas (≥ 99,999 % from AirLiquide, Paris, France) acted as a countermeasure. For each experiment, 200 ml of the $Si(OH)_4$ stock solution was transferred to a sealable 500 ml PVC-reactor (from Rotilab). Immediately afterwards (e.g. within the following five minutes), adequate amounts of calcium chloride ($CaCl_2$, p.a., from Merck, Darmstadt, Germany) and aluminium chloride hexahydrate ($AlCl_3 \cdot 6H_2O$, p.a., from Roth) were poured into the reactor to achieve molar ratios of Ca/Si equal to 1.0 and Al/Si of 0.05, respectively. This experimental setup was used for the precipitation of a pure C-A-S-H gel (i.e. reference material without Me). Except for this reference experiment, different quantities of either copper chloride dihydrate ($CuCl_2 \cdot 2H_2O$, p.a., from Roth), cobalt chloride hexahydrate ($CoCl_2 \cdot 6H_2O$, p.a., from Roth) or zinc chloride ($ZnCl_2$, p.a., from Merck) were added in powder form into the reactors, once the Ca- and Al-bearing salts were introduced, to precipitate Me-bearing C-A-S-H gels. The molar Me/Si ratios used in this second set of experiments were 0.05, 0.1, 0.15, 0.2, 0.25, 0.3, 0.4, 0.5 and 0.6. Higher Me/Si ratios were not tested, because the latter denotes the maximum bearing capacity of Me by C-A-S-H gels (see results section for further details). All reactive solutions were stirred continuously at 300 rpm over the duration of the experiments, which was 1 hour of reaction time. All experiments were performed at initially 23 ± 3 °C.

In order to track changes of the aqueous solution composition over the duration of the experiments, pH, temperature (T) and electric conductivity (Cond.) were monitored online (see below). Fluid samples (about 1 ml) were taken regularly every 0.5, 1, 5, 10, 30 and 60 minutes after salt addition with a 10 ml bearing syringe (B. Braun, 142 Omnifix® Solo, Melsungen, Germany) in order to follow temporal changes of the chemical composition of the reactive fluids. The liquid samples were filtered through 0.45 $\mu m$ cellulose acetate membrane syringe filters (Sartorius, Göttingen, Germany, filter diameter: 25 mm) and acidified by the addition of 20 $\mu l$ concentrated $HNO_3$ of suprapure grade (69 %, from Roth, ROTIPURAN®, Karlsruhe, Germany). An aliquot of each acidified liquid sample was further diluted to a 2 % $HNO_3$ matrix in preparation for subsequent chemical analysis.

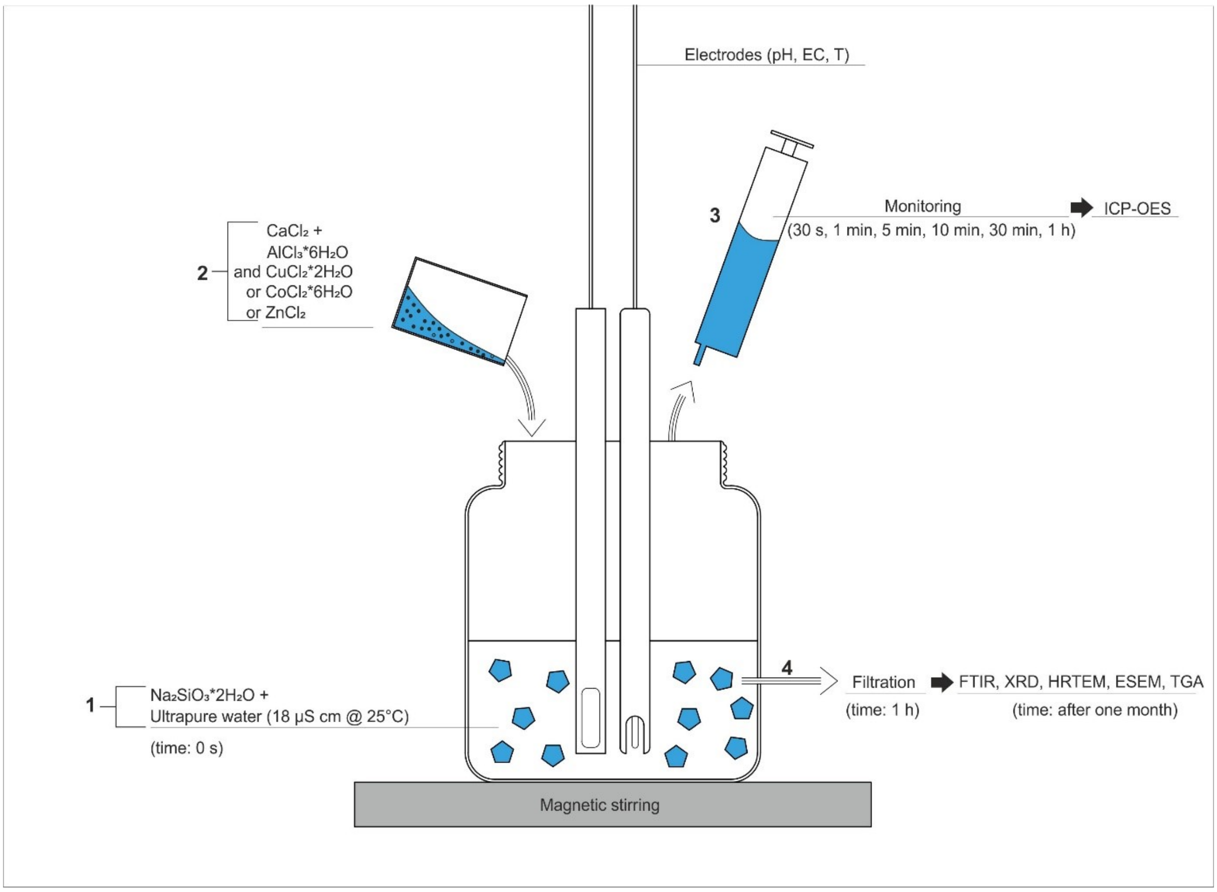

Figure 4: Schematic overview showing the experimental setup and multi-methodological approach used in this study for the precipitation and characterization of Me-bearing C-A-S-H gel phases and aqueous solutions. 1; Preparation of $Si(OH)_4$ stock solution; 2: Addition of Ca-, Al- and Me-salts as powders; 3: Hydrochemical monitoring and fluid sampling; 4: Sample filtration and preparation for solid-phase characterization methods.

After 1 hour of reaction time, all experiments were terminated. The precipitates were separated by filtration using a suction filtration unit and 0.45 $\mu m$ cellulose acetate filters (Sortorius Stedim Biotech; filter diameter: 50 mm). The solid remaining on the filter was washed with ultrapure water until the EC value of the filtrate water was lower than 1000 $\mu S/cm$ (e.g. within minutes to avoid partial dissolution of the precipitates). As for the drying process, the solid samples were put into 40 ml PE jars and stored in a closed desiccator until weight constancy was reached (approximately 1-2 months). The desiccator further contained a saturated $CaCl_2$ solution to ensure gentle drying of the precipitates at about 33 % relative humidity.

## 3.2. Analytical Methods

### 3.2.1. Liquid phase characterization

The solution pH, EC and temperature were measured in-situ with a WTW SenTix 41 glass electrode and a WTW LF 330 m connected to a WTW pH/cond 3320 multi parameter device, which was calibrated against pH 4.01, 7.00, and 10.00 NIST buffer standard solutions at 23 °C. The chemical composition of the reactive fluids was measured in acidified aliquots by means of inductively coupled plasma optical emission spectroscopy (ICP-OES) using a PerkinElmer Optima 8300 DV (Waltham, MA, USA). Analysis and data processing were performed at the Institute of Applied Geosciences (IAG), Graz University of Technology [52]. In total, 178 fluid samples were analysed for their concentrations of aqueous Ca, Al, Si, Na, Co, Cu and Zn. The analytical precision (2σ, 3 replicates) is better than ± 2 % for Co and Si and ± 4 % for Al, Ca, Na, Cu and Zn analyses, respectively, relative to replicate measurements of NIST 1640a, in-house and SPS-SW2 Batch 130 standards [53].

Hydrochemical modelling to further calculate the solubility products ($K_{SP}$) for (Me)-C-A-S-H was performed with the computer program PHREEQ-C (Version 2.18.3-5570). Therefore, a combined version of the databases minteqv4 and CEMDATA07 [54], [55] was used.

The Me ion removal efficiency was calculated with the following equation (1),

$$\%removal = \frac{(c_0 - c_e)}{c_0} \cdot 100 \qquad (1)$$

where $\%removal$ is the amount of Me removed from solution at the end of each experiment (given in %) and $c_0$ and $c_e$ are the initial and final concentrations of the Me of interest (in mg/l). The final solution was defined by almost constant concentrations of aqueous species through reaction time (steady-state conditions), thus being closest to "equilibrium" conditions. It has to be point out that for an amorphous phase a thermodynamic equilibrium is - in a strict meaning - not valid.

### 3.2.2. Solid phase characterization

*Fourier Transform Infrared (FTIR) Spectroscopy*

In order to get qualitative information about characteristic molecular bonding within the synthetic (Me)-C-A-S-H gels, Attenuated Total Reflection Fourier Transform Infrared (ATR-FTIR) spectroscopy was applied on a PerkinElmer Frontiers device (Waltham, MA, USA). IR spectra were recorded on fine powder materials in the near- to mid-infrared (NIR-MIR) range with wavenumbers from $4000\ cm^{-1}$ to $650\ cm^{-1}$ at a resolution of 1-2 $cm^{-1}$. For data evaluation, the obtained IR spectra were compared with published literature on C-A-S-H with and without Me, if available [14], [56]-[58].

*X-ray Diffraction (XRD)*

The mineralogical composition and the crystallinity degree of the solid phases were determined by X-ray diffraction (XRD) using a PANalytical X'Pert PRO diffractometer (Almelo, the Netherlands) operated at 40 kV and 40 mA (Co-Kα radiation source) and outfitted with a spinner stage, 0.5° antiscattering and divergence slits, primary and secondary soller and a high-speed Scientific X'Celerator detector. XRD patterns of randomly oriented samples, prepared with the standard top-loading technique, were recorded over a range of 4-60° $2\theta$ with a step size of 0.02° $2\theta$ and a scan speed of 4 steps/s. For the interpretation of the XRD patterns, the PANanalytical X'Pert Highscore Plus software [version 3.0d (3.0.4), Almelo, the Netherlands] and published literature [14], [26], [36], [59] on C-A-S-H phases was used.

*Environmental Scanning Electron Microscopy (ESEM)*

Selected samples (Ref, Co0.2, Co0.6, Cu0.2, Cu0.6, Zn0.2, Zn0.6) were analysed by environmental scanning electron microscopy (ESEM) in order to identify the main particle form and to track changes in the chemical composition of the final precipitates upon Me addition (note here that the number in the sample coding denotes the Me/Si molar ratio initially used for C-A-S-H gel synthesis). Compared to conventional SEM operation conditions, where high vacuum (HV) and coated samples are required, in ESEM, low vacuum (LV) conditions are used, which allow to investigate water-bearing and temperature-sensitive materials without further preparation (i.e. coating is not needed), as sample charging and outgassing can be significantly reduced [60]. As for this study, a FEI ESEM Quanta 450 FEG (FEI, Hillsboro, OR, USA) was used, which is fitted with a thermal field emission gun (FEG) operated at an accelerating voltage of 15 kV. Images of the respective sample surfaces were captured with a large filter (secondary electron) detector (LFD) and a circular back scattered electron (CBS) detector, respectively. Furthermore, a ThermoFisher Pathfinder EDX (Waltham, MA, USA) detector was used for resolving the chemical composition of (Me-bearing) C-A-S-H. Therefore, EDX spectra were acquired on selected single spots per samples at an analytical precision of < 2 at.% for all elements of interest, which included Ca, Al, Si and Me. Measurements were conducted at the Institute for Electron Microscopy and Nanoanalysis and Center for Electron Microscopy (FELMI-ZFE), Graz University of Technology.

*Analytical and Scanning Transmission Electron Microscopy (A/S-TEM)*

The crystal-chemistry and nano-structure of (Me)-C-A-S-H gels as well as proof of co-precipitates at high initial Me loads versus distribution of Me within C-A-S-H gels precipitated at low initial Me loads were analysed by transmission electron microscopy (TEM) performed on the following samples: Ref, Co0.1, Co0.3, Co0.5, Cu0.1, Cu0.3, Cu0.5, Zn0.1, Zn0.3 and Zn0.5. Therefore, small aliquods of the dried solids (about 1 mg) were dispersed in ethanol and subjected to ultrasonic treatment (about five minutes) to ensure complete dispersion of the particles. By using a pipette, a few droplets of the suspension were gathered and placed onto a C-coated standard TEM Cu grid. The instrument used was a FEI Tecnai F20, field emission gun, operated at an acceleration voltage of 200 kV and outfitted with a single-crystal $LaB_6$ Schottky Field Emitter, an ultra-Scan CCD camera for high-resolution imaging in TEM mode and an EDAX EDX detector for chemical analysis. TEM-EDX spectra were acquired using 30 s count time, at an analytical uncertainty of ± 2 % for most of the major elements [26],[61]. Scanning transmission electron microscopy (STEM) images were detected with a high angle annular dark field (HAADF) detector. The microscope is equipped with a Gatan imaging filter (GIF) for the acquisition of elemental maps (energy filtered transmission electron microscopy, EFTEM) as well as electron energy loss spectroscopy spectra (EELS).

### *Simultaneous Thermal Analysis (STA): Thermogravimetric Analysis (TGA) and Differential Scanning Calorimetry (DSC)*

The amount of structurally bond water versus water molecules adsorbed onto the surface of (Me)-C-A-S-H phases was analysed by means of simultaneous thermal analysis (STA). Measurements of selected samples (~30 mg of Ref_filtr, Co0.4, Cu0.4, Zn0.1 and Zn0.4) were performed under permanent $N_2$ flow, applying a heating rate of 10°/min in the temperature range from 25 °C up to 1000 °C in a first round. In a second round the samples Co0.4, Cu0.4 and Zn0.4 were dried in the oven at 40°C for one night and then heated up from 30 °C up to 1000 °C. The second round was done to ensure almost complete removal of excess water that remained on the C-A-S-H gel surface from gentle drying. The analytical apparatus used was a PerkinElmer STA 8000 simultaneous thermal analyzer. For data evaluation, which included analysis of the thermogravimetric (TG) and differential scanning calorimetry (DSC) curves, the Pyris Series – STA 8000 software was used.

## 4. Results

### 4.1. Evolution of the aqueous solution during (Me)-C-A-S-H gel precipitation

Herein the temporal changes of the chemical composition of the aqueous solutions during (Me)-C-A-S-H gel precipitation and maturation are presented. In Figure 5, plots of the dissolved ion concentrations (Na, Ca, Al, Si and Me) and reactive fluid pH against the reaction time are shown for experiments conducted at low initial Me/Si molar ratios (e.g. Me/Si = 0.05) and high Me/Si molar ratios (e.g. Me/Si = 0.5), respectively. A compilation of all experimental data obtained in this study is given in the appendix (Figure AP 1-Figure AP 3).

The pH of the $Si(OH)_4$ stock solution was in the range from 12.3 to 12.8 (± 0.2 pH units) for all experiments, with a mean pH of 12.5. A drastic and abrupt drop in pH of about 1-2 pH units (up to ~3 pH units in the case of Zn0.5) occurred within the first seconds after addition of the Ca-, Al- and Me-salts in all experiments (Fig. 5). However, in the reference experiment (without Me) the decrease in pH was less pronounced, reaching a value of about 11.2 after 1 h of reaction time, whereas a systematic and high drop in pH was seen for all experiments run with high Me loads. As for the Co-series a rather gradual drop in pH was observed over time, while the evolution of the pH curves as observed for the Cu- and especially the Zn-series was noticeably more complex: A sudden decrease in pH in the first minutes after salt addition up to pH values as low as 9.3 to 10.1 is followed by a pH increase by up to 2 pH units within 1 to 30 min of reaction time, reaching stable pH values thereafter until the end of the experiments (e.g. pH 10.1 to 11.3, depending on the Me used). Noteworthy, the time needed to reach a constant pH value in the reactive fluids increased at elevated Me concentrations initially introduced into the respective C-A-S-H synthesis experiments, which led to a delayed achievement of steady-state conditions (Fig. 5).

The $Na^+$ concentration in the aqueous solution did virtually not change over time in any of the conducted experiments, signifying the conservative behavior of this element (Fig. 5). As for the other cations (Al, Si and Me; except for Ca) a fast and quantitatively important decrease in concentration took place within the first minute(s) after salt addition. At the end of the experiments, Al and Me were almost quantitatively removed from the reactive solution. The Si concentration decreased more slowly and rather continuously over the duration of the experiments, compared to Al and Me, until chemical steady-state conditions (defined here as achievement of "equilibrium"; see discussion above) were reached after about 10 to 30 min of reaction time.

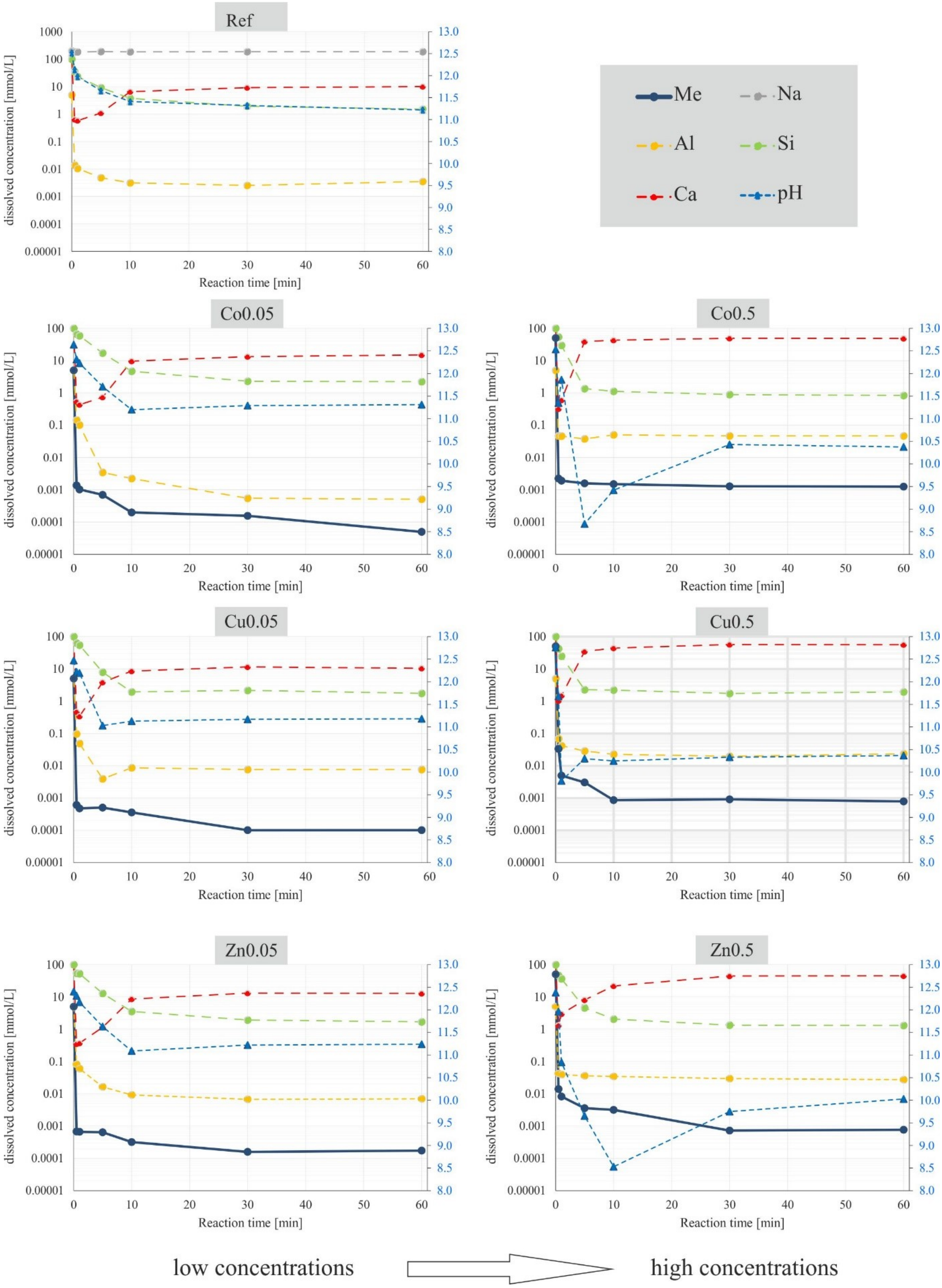

Figure 5: Temporal evolution of the elemental concentrations and reactive fluid pH for the reference experiment (Ref, upper left) and experiments run at Me/Si molar ratios of 0.05 (left panel) and 0.5 (right panel), respectively.

In contrast to all other elements, the $Ca^{2+}$ concentrations decreased rapidly after salt addition, but increased afterwards until the achievement of near-equilibrium conditions after about 10-30 min (Fig. 5). From these experimental results, the removal efficiency for all elements of interest were calculated after the attainment of chemical steady-state conditions (60 min) and are presented in Table 1. The mean removal efficiencies for Si and Al are 98.4 % and 99.6 % respectively. The removal efficiency for Ca was found to drop from about 90 % to 40 % as the initial Me input was increased. The removal efficiency for all types of Me used was close to 100 % in all experiments (see Table 1).

Table 1: Compilation of experimental solution data obtained after 60 min. Note the high removal efficiencies for aqueous Al, Si and Me.

| | Initial composition of exp. solution | | | | | Final composition of exp. solution | | | | | Removal efficiency | | | |
|---|---|---|---|---|---|---|---|---|---|---|---|---|---|---|
| | Ca | Al | Si | Me | pH | Ca | Al | Si | Me | pH | Ca | Al | Si | Me |
| Exp. | mM/L | mM/L | mM/L | mM/L | | mM/L | mM/L | mM/L | mM/L | | %rem | %rem | %rem | %rem |
| Ref | 100.0 | 5.0 | 100.0 | | 12.5 | 9.6264 | 0.0030 | 1.7230 | | 11.2 | 90.374 | 99.940 | 98.277 | |
| Co0.05 | 100.0 | 5.0 | 100.0 | 5 | 12.6 | 14.1099 | 0.0005 | 2.2676 | 0.0001 | 11.3 | 85.890 | 99.989 | 97.732 | 99.998 |
| Co0.1 | 100.0 | 5.0 | 100.0 | 10 | 12.7 | 15.7635 | 0.0059 | 1.8725 | 0.0002 | 11.2 | 84.236 | 99.882 | 98.128 | 99.998 |
| Co0.15 | 100.0 | 5.0 | 100.0 | 15 | 12.6 | 18.9440 | 0.0140 | 1.7160 | 0.0001 | 11.0 | 81.056 | 99.720 | 98.284 | 99.999 |
| Co0.2 | 100.0 | 5.0 | 100.0 | 20 | 12.8 | 25.2711 | 0.0235 | 1.2626 | 0.0000 | 11.0 | 74.729 | 99.530 | 98.737 | 100.000 |
| Co0.25 | 100.0 | 5.0 | 100.0 | 25 | 12.5 | 26.6218 | 0.0256 | 1.4143 | 0.0007 | 10.8 | 73.378 | 99.488 | 98.586 | 99.997 |
| Co0.3 | 100.0 | 5.0 | 100.0 | 30 | 12.5 | 27.6180 | 0.0335 | 1.4214 | 0.0007 | 10.7 | 72.382 | 99.330 | 98.579 | 99.998 |
| Co0.4 | 100.0 | 5.0 | 100.0 | 40 | 12.6 | 45.6829 | 0.0402 | 1.1447 | 0.0009 | 10.6 | 54.317 | 99.197 | 98.855 | 99.998 |
| Co0.5 | 100.0 | 5.0 | 100.0 | 50 | 12.5 | 48.8643 | 0.0464 | 0.8622 | 0.0013 | 10.4 | 51.136 | 99.071 | 99.138 | 99.997 |
| Co0.6 | 100.0 | 5.0 | 100.0 | 60 | 12.5 | 55.7877 | 0.0338 | 0.6141 | 0.0018 | 10.1 | 44.212 | 99.325 | 99.386 | 99.997 |
| Cu0.05 | 100.0 | 5.0 | 100.0 | 5 | 12.5 | 10.9502 | 0.0076 | 1.9509 | 0.0001 | 11.2 | 89.050 | 99.847 | 98.049 | 99.998 |
| Cu0.1 | 100.0 | 5.0 | 100.0 | 10 | 12.4 | 15.5818 | 0.0014 | 2.0804 | 0.0002 | 11.0 | 84.418 | 99.972 | 97.920 | 99.998 |
| Cu0.15 | 100.0 | 5.0 | 100.0 | 15 | 12.3 | 18.7325 | 0.0020 | 2.1691 | 0.0001 | 10.9 | 81.268 | 99.959 | 97.831 | 100.000 |
| Cu0.2 | 100.0 | 5.0 | 100.0 | 20 | 12.5 | 30.1380 | 0.0025 | 1.7051 | 0.0003 | 10.7 | 69.862 | 99.949 | 98.295 | 99.998 |
| Cu0.25 | 100.0 | 5.0 | 100.0 | 25 | 12.7 | 31.4226 | 0.0090 | 1.7620 | 0.0003 | 10.8 | 68.577 | 99.820 | 98.238 | 99.999 |
| Cu0.3 | 100.0 | 5.0 | 100.0 | 30 | 12.7 | 34.4720 | 0.0119 | 1.8082 | 0.0004 | 10.6 | 65.528 | 99.761 | 98.192 | 99.999 |
| Cu0.4 | 100.0 | 5.0 | 100.0 | 40 | 12.8 | 45.8466 | 0.0101 | 1.5727 | 0.0007 | 10.5 | 54.153 | 99.798 | 98.427 | 99.998 |
| Cu0.5 | 100.0 | 5.0 | 100.0 | 50 | 12.8 | 56.6106 | 0.0216 | 1.8323 | 0.0008 | 10.4 | 43.389 | 99.569 | 98.168 | 99.998 |
| Cu0.6 | 100.0 | 5.0 | 100.0 | 60 | 12.7 | 58.2223 | 0.0350 | 1.7720 | 0.0010 | 9.9 | 41.778 | 99.300 | 98.228 | 99.998 |
| Zn0.05 | 100.0 | 5.0 | 100.0 | 5 | 12.4 | 12.9779 | 0.0069 | 1.8159 | 0.0002 | 11.2 | 87.022 | 99.863 | 98.184 | 99.997 |
| Zn0.1 | 100.0 | 5.0 | 100.0 | 10 | 12.4 | 14.1030 | 0.0174 | 1.7717 | 0.0006 | 11.0 | 85.897 | 99.652 | 98.228 | 99.994 |
| Zn0.15 | 100.0 | 5.0 | 100.0 | 15 | 12.5 | 20.2246 | 0.0159 | 1.7588 | 0.0007 | 11.0 | 79.775 | 99.682 | 98.241 | 99.995 |
| Zn0.2 | 100.0 | 5.0 | 100.0 | 20 | 12.5 | 13.4919 | 0.0126 | 2.0070 | 0.0008 | 11.0 | 86.508 | 99.748 | 97.993 | 99.996 |
| Zn0.25 | 100.0 | 5.0 | 100.0 | 25 | 12.4 | 26.0451 | 0.0171 | 1.3611 | 0.0007 | 10.7 | 73.955 | 99.658 | 98.639 | 99.997 |
| Zn0.3 | 100.0 | 5.0 | 100.0 | 30 | 12.5 | 29.2453 | 0.0224 | 1.4991 | 0.0009 | 10.8 | 70.755 | 99.553 | 98.501 | 99.997 |
| Zn0.4 | 100.0 | 5.0 | 100.0 | 40 | 12.5 | 36.9306 | 0.0339 | 1.3284 | 0.0010 | 10.4 | 63.069 | 99.322 | 98.672 | 99.998 |
| Zn0.5 | 100.0 | 5.0 | 100.0 | 50 | 12.4 | 44.6988 | 0.0284 | 1.3215 | 0.0007 | 10.0 | 55.301 | 99.431 | 98.679 | 99.999 |
| Zn0.6 | 100.0 | 5.0 | 100.0 | 60 | 12.4 | 54.6619 | 0.0343 | 1.5568 | 0.0009 | 9.3 | 45.338 | 99.314 | 98.443 | 99.999 |

## 4.2.Solid phase characterization

### 4.2.1. Macroscopic description of precipitates

In general, the precipitates were very fine grained (i.e. nano-crystalline) and displayed a soft to greasy appearance right after filtration. The water loss of samples, as obtained after 34 days (15.03 – 18.04. 2019) of drying in the desiccator at room temperature, varied between 2 and 21 wt%, relative to the original weight of the wet material. Samples received from solutions loaded with higher Me/Si molar ratios generally lost more weight due to dehydration than samples synthetized at lower Me/Si values (see appendix Table AP 1). However, outside the desiccator (e.g. when treated with a pestle and mortar for further solid-phase analysis) the precipitates exhibited a paste-like consistency and displayed hygroscopic attributes. As for such materials, with compositions resembling C-A-S-H phases, the term "C-A-S-H gel" is widely used in the literature, and therefore it was adopted in the consecutive work [56]. However, when dried in the oven at 40 °C for one day the precipitates tended to form brittle crusts, which could be easily crushed to fine powders lacking any cohesion.

The most obvious optical characteristic of the synthesized products was the color (see Figure 6): (i) The reference material (without Me) had a translucent, whitish color. (ii) Materials from the Cu-series appeared azure blue in color; variations in the color intensity (pale blue to intense azure blue) were dependent on the amount of Cu initially added to the respective experiments. (iii) The Co-bearing gels showed a significant color change from purple-blue at low Co concentrations to lilac at high Co/Si molar ratios (e.g. > 0.4). It is worthy to note that the color switch was also related to the curing time. For example, for the sample Co0.6 it took about one day before a change in color took place, compared to Co0.5 (two days) and Co0.4 (several days). Furthermore, patches (2-3 mm in diameter) of lilac–colored material were observed within the purple-blue matrix after one month of drying even for samples prepared at the lowest Co concentrations. The latter two observations may indicate that the materials produced from the Co-series lack homogeneity. (iv) The precipitates from the Zn-series were white in color, and no further subdivision dependent on color was made.

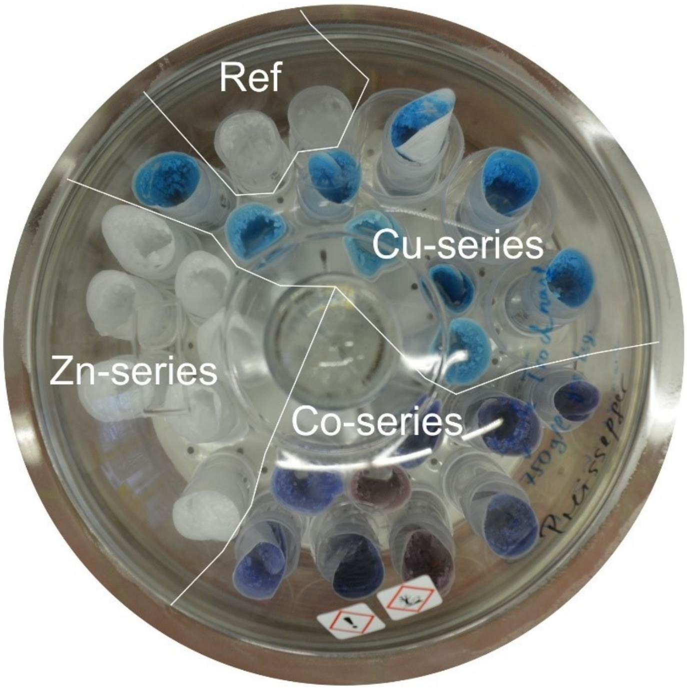

Figure 6: C-A-S-H gels stored in a desiccator (plan view) for drying. Note the significant variation in color of the precipitates as a function of the type of Me used. Azure blue = Cu-series; white = Zn-series and reference material; purple-blue and lilac = Co-series. The stronger the color`s intensity, the higher the amount of Me introduced in the system.

### 4.2.2. Mineralogy of precipitates (XRD and FTIR)

*X-ray diffraction*

XRD patterns of precipitates obtained from the reference experiment as well as from selected materials from the Co-, Cu- and Zn-series are shown in Figure 7 (for a full compilation of XRD data the reader is referred to Figure AP 4 - Figure AP 6 in the appendix). From these data, the poorly crystallized to X-ray amorphous (gel-like) nature of the precipitates is observable throughout all experiments conducted. As for the reference material (Ref_zentr, Ref_filtr) an intense asymmetric peak appears at around 3.07 Å, which belongs to the C-A-S-H structure. This reflection is partly overlapping with a weak 3.03 Å peak that is indicative of small amounts of calcite present in this sample (see Figure 7). Broad and diffuse reflections with a low intensity occur at 5.88 Å and 2.80 Å. These peaks are characteristic for tobermorite-type C-A-S-H gels [14], [26], [36]. The very weak 5.88 Å peak disappears with increasing Me content in the C-A-S-H structure, independent of the type of Me ion used for synthesis. This indicates a progressive collapse of the C-A-S-H structure at higher Me ion loads and a related transition toward a defect, amorphous material, i.e. a highly disordered tobermorite-like structure [26]. Small peaks at around 23.86° 2θ (~4.33 Å) and 55.16° 2θ (~1.93 Å ) are barely present in some samples. These peaks are characteristic for hexagonal monohydrocalcite [$CaCO_3$ $H_2O$] [59].

As described in chapter 4.2.1, the precipitates from the Co-series had two different colours. When analysed by XRD a slight shift of the main reflection from ~3.05 Å (when lilac) to 3.03 Å (when purple-blue) is noticeable (see Figure 7). Furthermore, the precipitates from the Co-series show a distinct sign of phase separation during C-A-S-H precipitation and maturation, because at a Me/Si ratio above 0.3, broad reflections develops at 2.65 Å and 3.23 Å, in addition to the main reflection at ~3.05 Å (see Figure 7). Therefore, it is possible that above a certain threshold value of Co in the tobermorite-type C-A-S-H structure, a second C-A-S-H phase emerges, which is relatively enriched in Co. Theoretically, the substitution of the larger Ca ion (0.97 Å) by the smaller Co ion (0.82 Å) would result in a reduction of the unit cell parameters of the C-A-S-H structure, which could explain the observed trend from 3.05 Å down to 3.03 Å. However, the peaks at 2.65 Å and 3.23 Å could belong to β-$Co(OH)_2$, which is more stable than α-$Co(OH)_2$ in a highly alkaline environment [62]. Revealing the precise nature of this Co-rich co-precipitate is difficult, mainly because of the low crystallinity degree of this material.

As for the Cu-series there is evidence for mineral phase segregation already at a Me/Si molar ratio of 0.1. However, co-precipitation of a segregated Cu-phase among Cu-bearing C-A-S-H gel becomes more obvious at a Me/Si molar ratio above 0.25, as seen by an increase of the peak intensities at 5.49 Å, 2.77 Å and 2.27 Å, relative to the broad reflection at 3.06 Å, which signifies the dominance of a tobermorite-type C-A-S-H structure with incorporated Cu. The unequivocal proof for the co-precipitation of atacamite [$Cu_2(OH)_3Cl$] is seen at a Me/Si molar ratio exceeding 0.3, which denotes the maximum load of Cu in a tobermorite-type C-A-S-H structure.

As for the Zn-series no mineral phase segregation has been observed, such as co-precipitation of Zn-hydroxides [$Zn(OH)_2$] or a sauconite-like material (Zn-smectite: $Na_{0.3}Zn_3[SiAl)_4O_{10}](OH)_2{\cdot}4H_2O$), even at the highest Me/Si molar ratio of 0.6 [14], [26]. Indeed, the only mineral phase that has been formed in the experimental series with Zn is a highly defect (tobermorite-type) C-A-S-H structure with incorporated Zn, as evidenced by the main reflection at 3.07 Å.

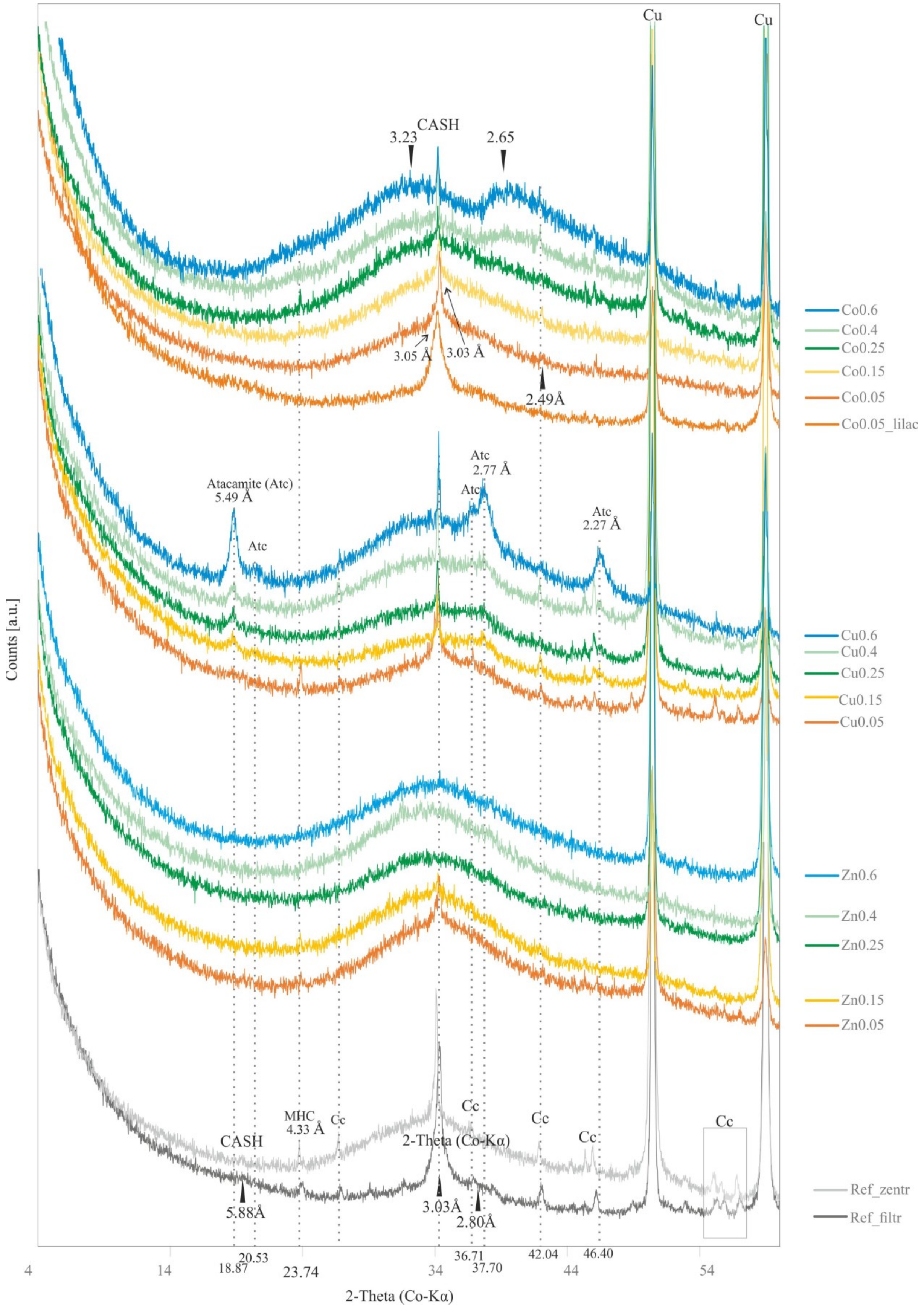

Figure 7: XRD patterns of the reference material (Ref) and Me-bearing precipitates obtained after drying for about one month in the desiccator. Atc – Atacamite, Paratc – Paratacamite, Cc – Calcite, MHC – Monohydrocalcite, CASH – Calcium aluminium silicate hydrate.

Co-precipitation of calcite is generally negligible in all experiments conducted, although trace amounts of this mineral phase have been identified in some precipitates from the Cu-series. The XRD pattern of materials collected right after filtration (not shown in here), however, revealed the absence of calcite, meaning that this secondary phase primarily arose during the drying process in the desiccator.

*Fourier Transformation Infrared Spectroscopy*

FTIR analysis of the synthesized materials was performed (i) directly after the filtration of the samples at the end of the experiments (wet material: FTIR 1) and (ii) after 1-1.5 months of drying in a desiccator (dry material: FTIR 2). This repeated measurement was done to verify that the materials did not suffer from the drying process, for example, via carbonation of the labile C-A-S-H gels and/or C-A-S-H phase decomposition to form silica gels, carbonates and Me-(oxy)hydrates. The FTIR spectra (FTIR 1) obtained from the wet materials are presented in the appendix Figure AP 7-Figure AP 9. The FTIR spectra (FTIR 2) of the dry materials are shown in Figure 8.

The main FTIR bands, which are characteristic for all types of synthesized C-A-S-H gels with and without Me, occur in the range of 2600 – 4000 cm$^{-1}$ (hydroxyl stretching region) and 650 – 1800 cm$^{-1}$ (lattice vibration region). All samples show a broad and intense IR band in the range of 2900 to 3700 cm$^{-1}$. This IR band is attributed to O–H stretching vibrations in $H_2O$ or hydroxyl molecules that are weakly bonded onto the C-A-S-H surface or in the interlayer [14]. As for the Co-series a reduction of the intensity of the hydroxyl stretching region can be observed for samples precipitated at a Me/Si molar ratio of < 0.3. At higher Co concentrations an additional IR band can be seen at 3636 cm$^{-1}$, which can be most likely assigned to the hydroxyl groups in β-cobalt hydroxide structures [63]. The precipitates of the Cu-series, on the other hand, already showed weak IR bands developed at 3449 cm$^{-1}$ and 3350 cm$^{-1}$, when the initial Me/Si molar ratio exceeded 0.4, which could be assigned to atacamite [58]. The precipitates of the Zn-series did not show any distinct IR bands in the hydroxyl stretching region.

Structural details about the precipitated Me-bearing C-A-S-H phases can be obtained from the analysis of the lattice vibration region (Figure 8). The IR band centred at around 940–960 cm$^{-1}$ is attributed to Si–O and Si-O-Al stretching vibrations in C-A-S-H gels [56]. García-Lodeiro et al. [56] observed that the position of the Si–O band is dependent on the pH of the parent solution, whereby a lower pH (9.26) comes along with higher frequencies of the Si–O band (1041 $cm^{-1}$) and vice versa (pH 11.14 → 975 $cm^{-1}$). This trend is consistent with this study. Generally, the IR band at around 970 $cm^{-1}$ is related to Si–O stretching vibrations of the $Q_2$ tetrahedral positions within C-A-S-H phases [57]. The absence of silica-rich co-precipitates (e.g. amorphous silica) in all samples is arguably indicated by the IR spectra, because no IR band was detected at 1070 $cm^{-1}$ [56]. Rarely, another IR band is seen at around 827 $cm^{-1}$, which is probably related to by Si–O symmetric stretching vibrations [56]. Out-of-plane bending of $CO_3^{2-}$ functional groups is evidenced by the IR band at 875 $cm^{-1}$ [14], [57], corresponding to monohydrocalcite and/or calcite, according to the XRD results (see Figure 7). Also, the IR bands at around 1400 $cm^{-1}$ and 1500 $cm^{-1}$ belong to carbonates (i. e. asymmetric stretching of $CO_3^{2-}$) [56], [57]. A band around 1632-1638 $cm^{-1}$ occurs in all samples and is related to H-O-H bending vibration in water molecules [57]. Note that this band behaves like the band at 2900 to 3700 $cm^{-1}$. A more pronounced band in this region is consistent with the development of a 14 Å tobermorite-like structure [57]. Materials from the Co-series, which differed in colour, exhibit different amounts of interlayer water (see Figure 8), which is indicative of a phase separation as observed by XRD. Bands at around 1550 $cm^{-1}$ only occur in Me incorporated precipitates but cannot be assigned to a functional group.

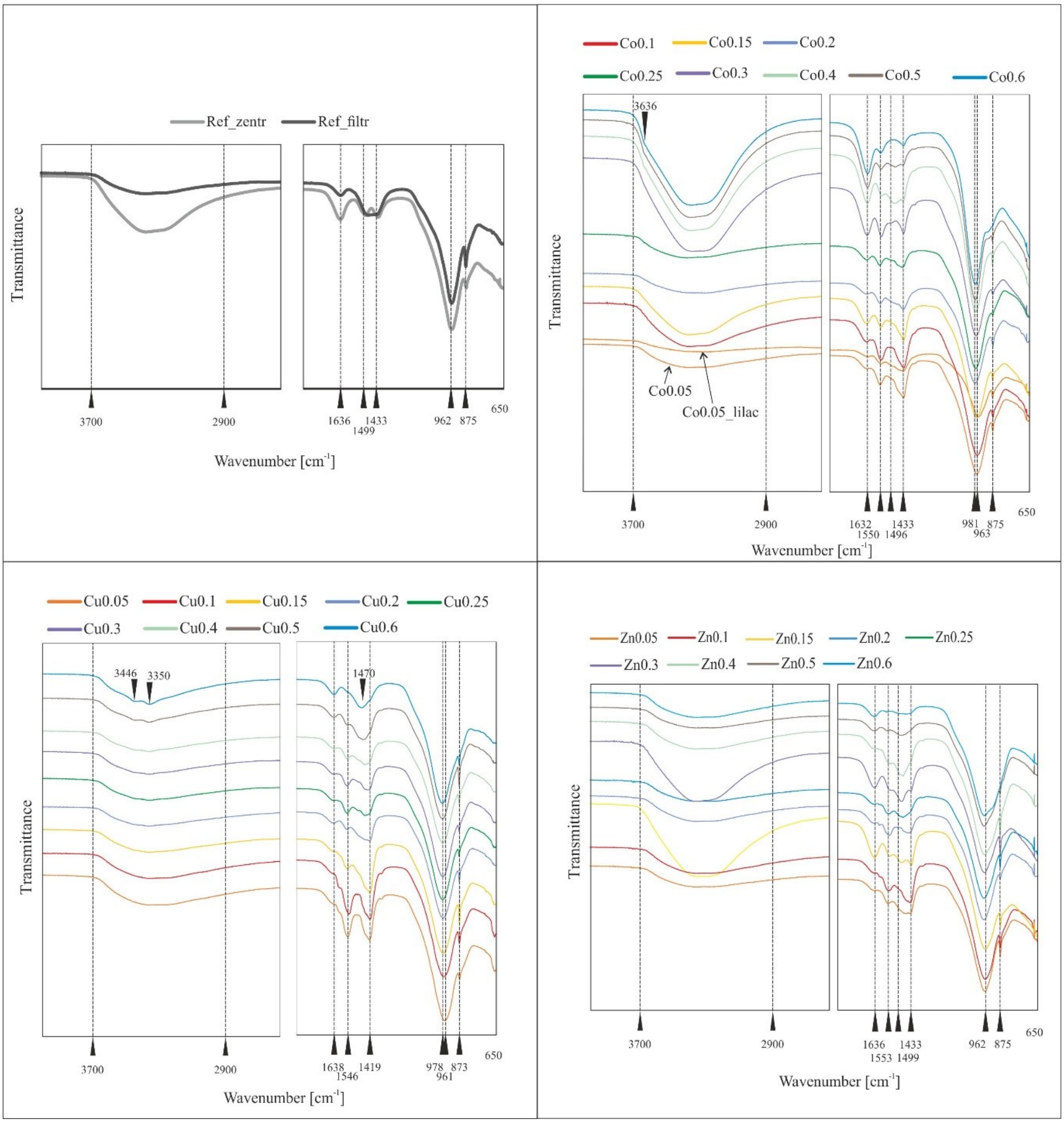

Figure 8: FTIR spectra of the reference material (Ref) and Me-bearing precipitates obtained after drying for about one month in the desiccator. See text for explanations.

### 4.2.3. Water content of precipitates

The results of the thermogravimetric analysis (TGA) of materials dried in the desiccator are shown in Figure 9. All samples experienced a high overall weight loss when heated up from 25 °C to 1000°C. The reference sample (Ref_filtr) and sample Zn0.1 lost about 63-69 wt% of the original weight, compared to samples Co0.4, Cu0.4 and Zn0.4, which lost about 78-81 wt%. A trend to higher amounts of adsorbed molecular water can thus be inferred for C-A-S-H phases containing higher Me loads.

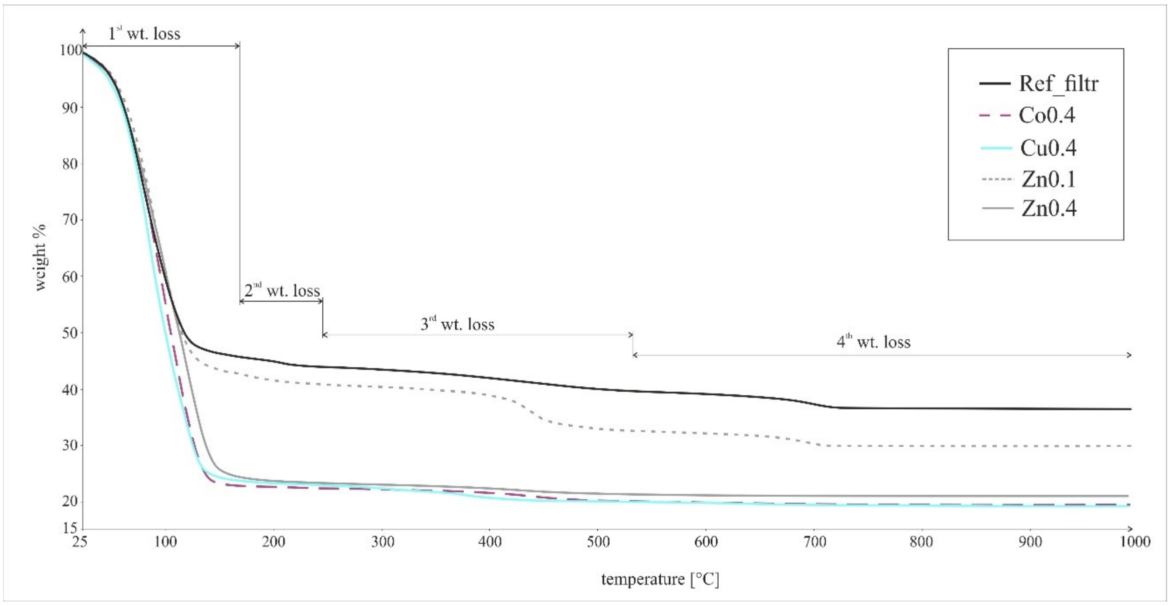

Figure 9: Thermogravimetric (TG) curves of selected samples.

From the TG results (Figure 9) four different temperature intervals were distinguished, which are listed in Table 2, each corresponding to a distinct mineral reaction. The most pronounced weight loss in all samples occurred in the temperature range from 25 °C to 170 °C, which is due to the removal of mostly physically bound molecular water in the synthesized products [39], [47], [64]. The second, less pronounced weight loss is seen at around 180-240 °C, which occurs due to the thermal decomposition of the C-A-S-H gels [64]. In samples having high loads of Me this weight loss seems to be shifted to lower temperatures and therefore overlaps with the main dehydration (see appendix Figure AP 10 and Figure AP 11). The third weight loss, which is due to the decomposition of C-A-S-H gels, occurs in the temperature range from 240 °C to 535 °C [64]. Particularly, a strong weight loss was observed at 400-500 °C (e.g. 8.33 wt.% in sample Zn0.1), which is usually attributed to the decomposition of portlandite [$Ca(OH)_2$] [65], [66]. However, portlandite could not be identified in this sample by XRD and FTIR techniques. Therefore, this weight loss might be attributed to the decomposition of monohydrocalcite to liberate $H_2O$. The fourth weight loss occurred at around 535-1000 °C, where calcium carbonate ($CaCO_3$), such as calcite, decomposes [47],[67]. In the samples Ref_filtr and Zn0.1 a weight loss of about 2.6-3.2 wt. % occurred in this temperature range, whereas in samples Zn0.4, Cu0.4 and Co0.4 only a small weight loss (< 1 wt%) due to $CO_2$ liberation was detected. Overall, the TG results are consistent with the XRD and FTIR data.

Table 2: Summary of calculated weight losses and related temperature ranges for selected samples, as obtained from TG curves. Note that the DSC signal was negative in the reported temperature intervals, reflecting endothermic reactions. Blue = partly wt. loss due to monohydrocalcite (MHC). Orange= wt. loss due to $CaCO_3$ or MHC decomposition.

| Sample | total wt. loss 25-1000 °C [wt%] | 1st wt. loss 25-170 °C [wt%] | 2nd wt. loss 170-240 °C [wt%] | 3rd wt. loss 240-535 °C [wt%] | 4th wt. loss 535-1000 °C [wt%] | wt. loss 105-1000 °C [wt%] | calculated water in (Me)C-A-S-H [wt%] |
|---|---|---|---|---|---|---|---|
| Ref_filtr | 63.1 | 54.0 | 1.7 | 4.3 | 3.2 | 20.0 | 17.4 |
| Co0.4 | 80.1 | 76.5 | - | 2.9 | 0.5 | 30.9 | 30.6 |
| Cu0.4 | 80.4 | 75.3 | - | 3.8 | 0.7 | 26.3 | 25.8 |
| Zn0.1 | 69.9 | 57.2 | 1.7 | 8.3 | 2.7 | 27.1 | 24.2 |
| Zn0.4 | 78.2 | 75.3 | - | 2.6 | 0.4 | 35.7 | 35.5 |

For the determination of the amount of chemically bound water within the Me-bearing C-A-S-H phases and Me-free reference material the temperature range from 105 to 1000 °C was considered here, as proposed by Vollpracht [65] for the loss of chemical bound water in C-S-H (see appendix Table AP 3-Table AP 7 for calculation). After subtraction of the weight loss due to monohydrocalcite and calcite decomposition, the content of chemically bound water is ~18 wt% for the reference sample with no Me incorporated. For samples, which contain Me, the chemically bound water content ranges from 25 to 35 wt%. Stumm [39] reported a water content of about 15-20 wt% for samples with Zn incorporated, however, the molar (Zn+Ca)/Si ratio of the synthesized Cu-bearing C-A-S-H was somewhat lower (about 0.66) compared this study (about 1.0). Generally, Ca-rich C-A-S-H phases exhibit a higher amount of molecular water [37].

Due to the conspicuously high water content the samples Co0.4, Cu0.4 and Zn0.4 were dried at 40 °C and measured again by STA. This results (see Table 3) show considerably lower values for structural bound water in Me-C-A-S-H, which is in the order of 18-24 wt%.

From the combination of the TG data and mass balance considerations based on ICP-OES results (e.g. taking the removal efficiencies of Me, Al, Ca and Si for each sample into account), the molar proportions of the individual components mentioned above in (Me)-C-A-S-H precipitates were determined (see Table 4, Figure AP 13-15). These molar proportions were then standardized to the average $SiO_2$ content in C-A-S-H, which is 1.

Table 3: Summary of calculated weight losses of the selected samples after drying and related temperature ranges for selected samples, as obtained from TG curves. Orange= wt. loss due to $CaCO_3$ decomposition.

| Sample | total wt. loss 30-1000°C [wt%] | wt. loss 30°C-105°C [wt%] | 1st wt. loss 105°C-300°C [wt%] | 2nd wt. loss 300°C-596°C [wt%] | 3rd wt. loss 596°C-744°C [wt%] | wt. loss 105°C-1000°C [wt%] | calculated water in (Me)C-A-S-H [wt%] |
|---|---|---|---|---|---|---|---|
| Co0.4 | 24.4 | 4.4 | 7.3 | 10.9 | 2.1 | 20.0 | 18.3 |
| Cu0.4 | 28.7 | 3.8 | 10.0 | 12.5 | 1.5 | 24.9 | 23.7 |
| Zn0.4 | 23.2 | 4.0 | 9.5 | 8.0 | 1.5 | 19.2 | 17.9 |

Table 4: Calculated molar compositions of (Me)-C-A-S-H precipitates.

| Sample | mol. prop. CaO | mol prop. CoO, CuO, ZnO | mol prop. $SiO_2$ | mol. prop. $Al_2O_3$ | mol. prop. water |
|---|---|---|---|---|---|
| Ref_filtr | 0.92 | 0.00 | 1.00 | 0.03 | 1.33 |
| Co0.4 | 0.54 | 0.40 | 1.00 | 0.03 | 1.49 |
| Cu0.4 | 0.54 | 0.40 | 1.00 | 0.03 | 2.10 |
| Zn0.4 | 0.64 | 0.40 | 1.00 | 0.03 | 1.59 |

### 4.2.4. Shape and crystal chemistry of precipitates

*Environmental scanning electron microscopy*

Backscattered electron images and EDX spectra obtained by ESEM analysis of selected (Me)-C-A-S-H gel samples are presented in Figure 10. The reference material without Me consisted of fine-grained (nanometer-sized) C-A-S-H particles having tiny, snowflake-shaped calcite crystals attached on its surface (see Figure AP 16), which is due to carbonation of the C-A-S-H phases upon drying. As for the samples Co0.2, Co0.6, Zn0.2 and Zn0.6 a homogeneous, nano-crystallized matrix made of C-A-S-H with incorporated Me was observed (see Figure 10 a,b,e,f), without regions that were relatively enriched in Me (denoting the absence of discrete Me-(oxy)hydrates). Samples Zn0.2 and Zn0.6 frequently contained agglomerated, flocculent particles (yellow circles in Figure 10 e,f), typical for C-A-S-H gels precipitated at room temperature [68]. In contrast, precipitates from the Cu-series were characterized, even at relatively low Cu/Si molar ratios of 0.2, by the presence of nodules rich in Cu (see Figure 10 c), which were identified as atacamite (Atc) by XRD. At a molar Cu/Si ratio of 0.6, the poly-phase character of materials produced from the Cu-series was more pronounced, and clusters of Cu-bearing C-A-S-H and co-precipitated atacamite were abundant (see Figure 10 d).

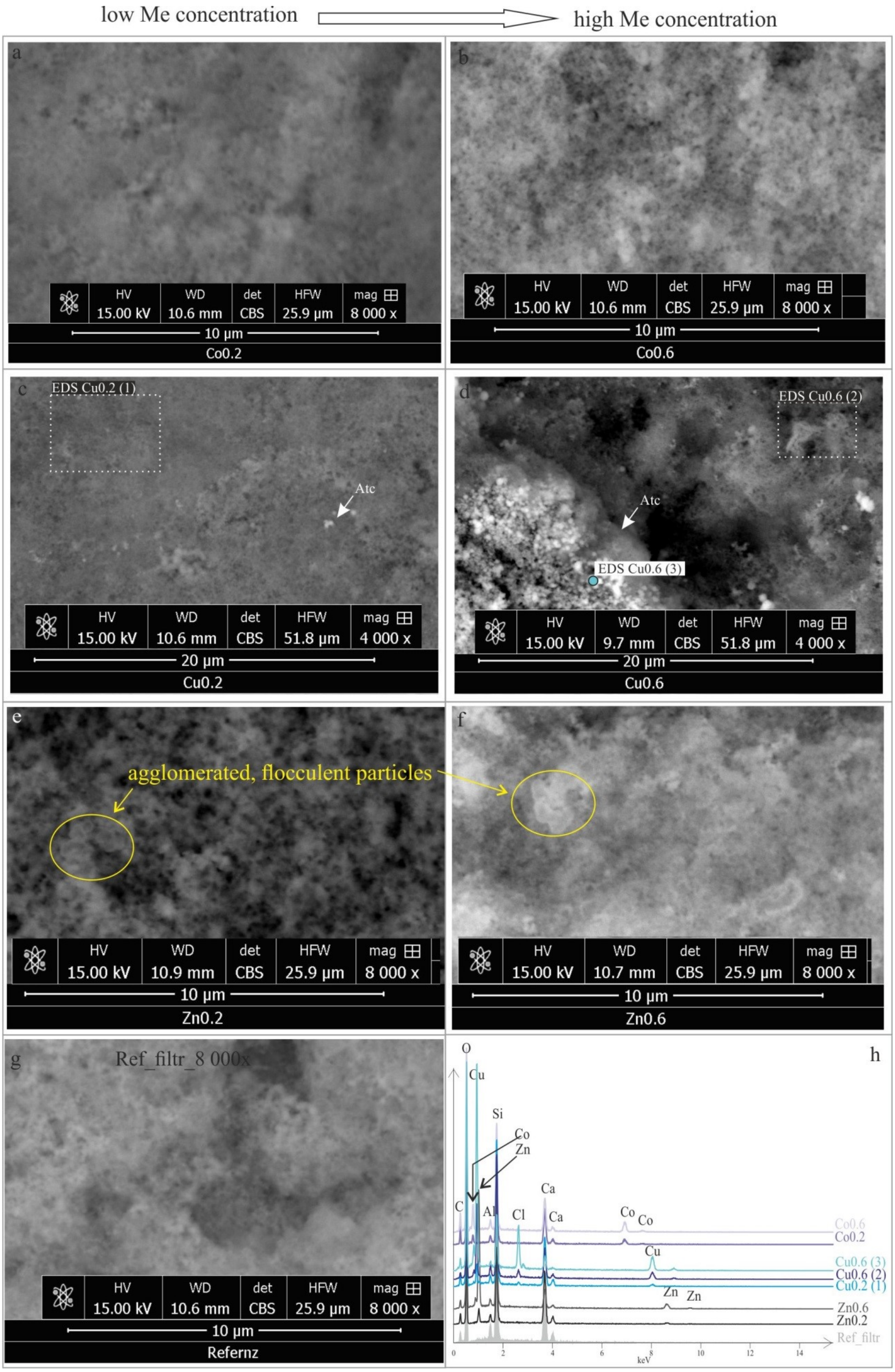

Figure 10: BSE images of a-b) Co-bearing C-A-S-H, c-d) Cu-bearing C-A-S-H, e-f) Zn-bearing C-A-S-H materials and g) the reference material without Me. h = EDS spectra of the respective materials. Yellow circles= Agglomerated, flocculent particles, typical for C-A-S-H gels precipitated at room temperature [68].

*Transmission electron microscopy*

The particle shape, the chemical composition as well as the degree of crystallinity of C-A-S-H with and without Me are shown in Figure 11 and Figure 12, respectively, for the reference material, the Co-series, the Cu-series and the Zn-series. More detailed illustrations as well as EDS spectra of the C-A-S-H gels bearing low to high Me concentrations are presented in the appendix Figure AP 17 to Figure AP 19. As for the particle form, the reference material showed agglomerates of fine-grained, flocculent particles, with an average particle diameter of approximately 50-100 nm (Figure 11).

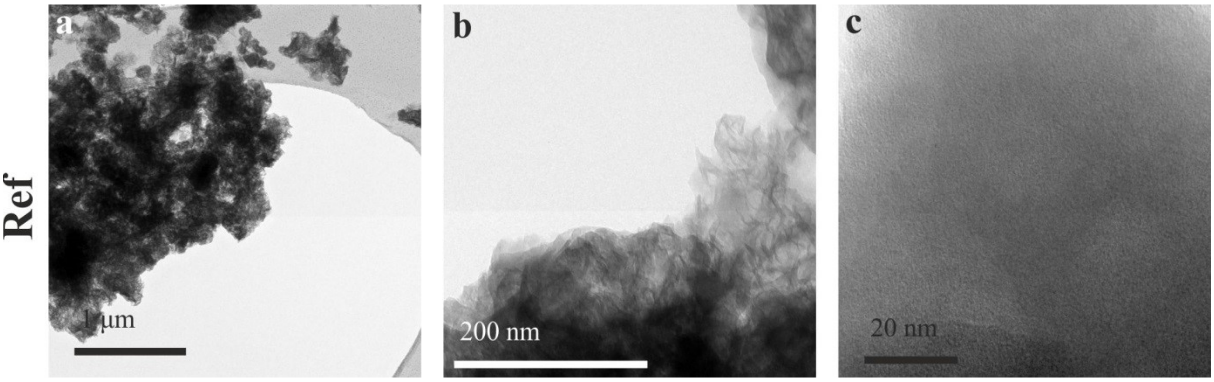

Figure 11: TEM images of the reference material.

Similar particle forms were developed within the Co-series (see Figure 12 a-c). The tiny flakes, however, form snowball-like clusters with a size of about 50-100 nm (see Figure 12 a). The bright spots in Figure 12 c could arise from β-$Co(OH)_2$ co-precipitates such as implied by XRD and FTIR analysis. The EDS spectra (see appendix Figure AP 17) show the systematic increase of the structural Co content in the respective Co-C-A-S-H samples. Also, minor traces of Na and Cl were detected in the precipitates from the Co-series, which correspond to halite impurities.

The fine-grained, flaky character of C-A-S-H particles could also be observed in the Cu-series (see Figure 12 d-f). However, the particles frequently displayed smooth edges, resulting in a more bubble-like appearance of C-A-S-H (see Figure 12 d). In the sample Cu0.5 a significant phase separation was observed. The bright snowball-shaped clusters (see Figure 12 f) represent areas that are strongly enriched in Cu, denoting the existence of atacamite as a co-precipitate. Traces of halite are also present in these samples as seen from EDS analysis (see Figure AP 18), which could not be removed by washing.

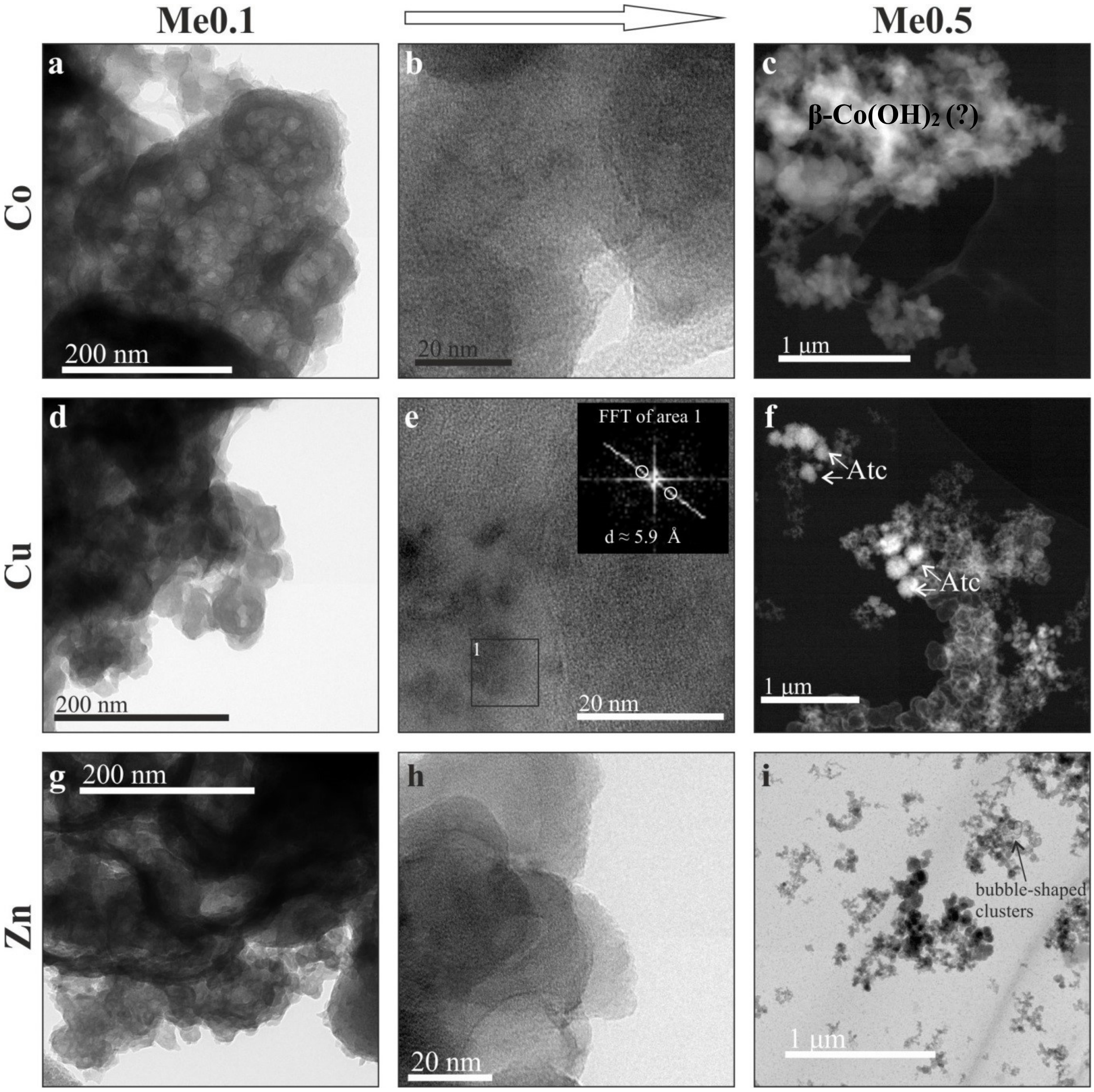

Figure 12: TEM images of a-c = Co-series (c=HAADF image of Co0.5), d-f = Cu-series (f = HAADF image of Cu0.5). Inserted FFT pattern correspond to C-A-S-H in e. TEM images g-i = Zn-series.

Particle aggregates present in the samples of the Zn-series (see Figure 12 g-i) tend to be even finer compared to the other C-A-S-H precipitates (30-40 nm), however, also coarser bubble-shaped hollow spheres (see Figure 12 i) with a size of about 100-200 nm were identified. The EDS spectra obtained for both particle types, labelled as Zn0.3 (1) and Zn0.3 (2) in Figure AP 19, revealed similar ratios of Zn/Si and Ca/Si, precluding a phase separation.

In general, all observed materials investigated lacked long-range order, meaning that they had an amorphous character. Very rarely, crystallized domains were observed in the C-A-S-H gels. For example, the d-spacing of about 5.9 Å (see Figure 12 e), as calculated from FFT pattern, likely correspond to the (201) plane in C-A-S-H [50].

# 5. Discussion

## 5.1. Precipitant mineralogy versus solution chemistry

The precipitated (Me)-C-A-S-H gels exhibited mineralogical, chemical and structural characteristics similar to a defect tobermorite with incorporated Me, as seen by the lack of the (002) reflection in the XRD pattern [40], [37], the IR bands and water contents typical for C-A-S-H gels and SEM/TEM-EDS-based compositions. Strictly speaking these gel-like precipitates are metastable [37], i.e. they will transform to more crystallized phases in the short-to medium-term (months to few years). However, an apparent chemical steady state between the aqueous phase and the solid phase was reached after about 10-30 minutes of reaction time in all experiments (see chapter 4.1), signifying that (Me)-C-A-S-H gel precipitation is a fast process. However, there is evidence for a segregated evolution of the (Me)-C-A-S-H phases, if considering that the Ca/Si molar ratio of the aqueous solutions changed significantly over time, i.e. a fast uptake of $Ca^{2+}$ and $Si(OH)_4$ by the early (jennite-type) precipitates within the first minutes is followed by a period where $Ca^{2+}$ is released back to the reactive solution whereas the concentration of $Si(OH)_4$ continued to decrease until equilibrium conditions were reached (see Figure 13). This indicates a transition toward a tobermorite-like structure via a dissolution/re-precipitation mechanism as the (Me)-C-A-S-H gels gain maturity. This process is further indicated by the results of hydrochemical modelling, which are shown in Figure 13. It can be seen that the formation of a jennite-type C-S-H (blue curve) is initially favoured over the tobermorite-type C-S-H phase (orange curve) and that this jennite-type (i.e. Ca-rich) precursor phase will transform into the more stable tobermorite-type (Ca-deleted) phase as the reaction progresses, corroborating the ICP-OES results. Furthermore, it can be concluded that the tobermorite-type C-S-H phase is not far off from thermodynamic equilibrium at the end of the experiments (i.e. $SI_{tob2}$ decreased from > 2.0 at the beginning down to ~0.5 at the end).

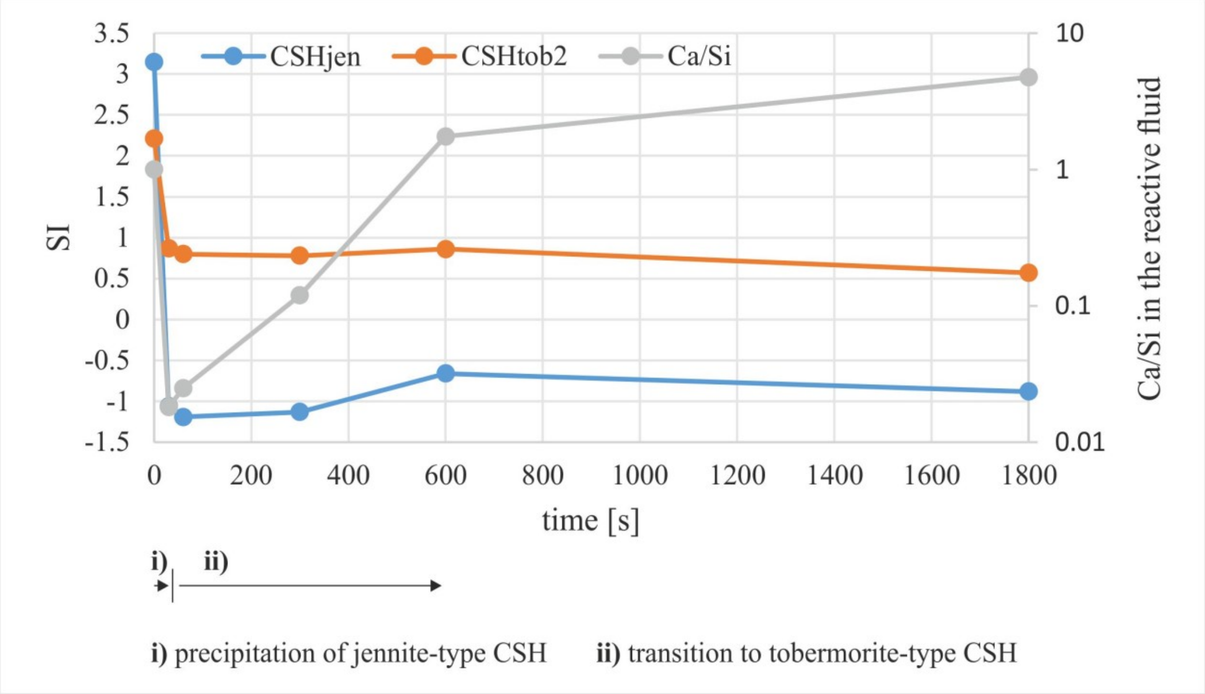

Figure 13: Evolution of the saturation index vs. time for the reference experiment. Presented are the SI values of jennite-type C-S-H (blue) and tobermorite-type C-S-H (orange), which are the two endmembers for C-S-H phases with Ca/Si ratios from 0.83 to 1.63. The change of the Ca/Si molar ratio of the reactive fluid over time is presented in grey.

From the reactive fluid composition obtained at apparent chemical steady state, the respective molar proportions of Me, Ca, Al and Si in the (Me)-C-A-S-H gels were calculated and are summarized in Table 5. The structural water content in the (Me)-C-A-S-H gels was determined on the basis of the STA data (see Table 5) for Ref, Co0.4, Cu0.4, Zn0.1 and Zn0.4, as described in section 4.2.3. As for the rest the water content was interpolated/extrapolated (see Table 5). Phase purity of (Me)-C-A-S-H was determined by mineralogical and electron microscopic analyses to define the threshold value for Me-incorporation in C-A-S-H, which is reached at an initial molar Me/Si ratio of about 0.3 for Co and Cu and above 0.6 for Zn (see Table 5). Note here that any reaction by-products below these threshold values are not taken into account in the calculations, as they only occur in minor quantities (e.g. forming less than 5 % of the total precipitated mass, according to the XRD and FTIR results). In the following, the (hydro-)geochemical datasets are discussed in more detail in relation to the crystal chemistry and solubility of the (Me)-C-A-S-H gels.

Table 5: Summary of (Me)-C-A-S-H gel compositions. Me is assumed to substitute for the Ca position in the C-A-S-H structure. Co-precipitates/secondary phases formed are indicated on the right. Red lines denote the upper threshold values for Me incorporation in C-A-S-H structures. Cc=calcite; MHC=monohydrocalcite; Atc=atacamite.

| (Me)-C-A-S-H composition (molar ratio) | | | | | molar ratio | Traces of other solids (primarily formed secondary during drying) |
|---|---|---|---|---|---|---|
| sample | Ca/(Si+Al) | (Ca+Me)/(Si+Al) | Me/(Si+Al) | mol% substitution of Ca | $H_2O$/Si | |
| Ref_filtr | 0.88 | 0.88 | - | - | 1.33 | Cc, MHC |
| Co0.05 | 0.84 | 0.88 | 0.05 | 5.5 | 1.35 | |
| Co0.1 | 0.82 | 0.91 | 0.10 | 10.6 | 1.37 | |
| Co0.15 | 0.78 | 0.93 | 0.15 | 15.6 | 1.39 | |
| Co0.2 | 0.72 | 0.91 | 0.19 | 21.1 | 1.41 | Cc |
| Co0.25 | 0.71 | 0.95 | 0.24 | 25.4 | 1.43 | MHC |
| Co0.3 | 0.70 | 0.99 | 0.29 | 29.3 | 1.45 | MHC |
| Co0.4 | 0.52 | 0.91 | 0.39 | - | 1.49 | $Co(OH)_2$ (?) |
| Co0.5 | 0.49 | 0.97 | 0.48 | - | | $Co(OH)_2$ (?) |
| Co0.6 | 0.42 | 1.00 | 0.57 | - | | $Co(OH)_2$ (?) |
| | | | | | | |
| Cu0.05 | 0.86 | 0.91 | 0.05 | 5.3 | 1.43 | Cc, MHC |
| Cu0.1 | 0.82 | 0.92 | 0.10 | 10.6 | 1.52 | Cc |
| Cu0.15 | 0.79 | 0.94 | 0.15 | 15.6 | 1.62 | Cc |
| Cu0.2 | 0.68 | 0.87 | 0.19 | 22.3 | 1.72 | Cc |
| Cu0.25 | 0.66 | 0.91 | 0.24 | 26.7 | 1.81 | |
| Cu0.3 | 0.64 | 0.93 | 0.29 | 31.4 | 1.91 | |
| Cu0.4 | 0.52 | 0.91 | 0.39 | - | 2.01 | Atc, Cc |
| Cu0.5 | 0.42 | 0.91 | 0.48 | - | | Atc, Cc |
| Cu0.6 | 0.40 | 0.99 | 0.58 | - | | Atc, Cc |
| | | | | | | |
| Zn0.05 | 0.84 | 0.89 | 0.05 | 5.4 | 1.36 | |
| Zn0.1 | 0.83 | 0.93 | 0.10 | 10.4 | 1.40 | MHC |
| Zn0.15 | 0.77 | 0.92 | 0.15 | 15.8 | 1.43 | |
| Zn0.2 | 0.84 | 1.03 | 0.19 | 18.8 | 1.46 | MHC |
| Zn0.25 | 0.71 | 0.95 | 0.24 | 25.3 | 1.50 | |
| Zn0.3 | 0.68 | 0.97 | 0.29 | 29.8 | 1.53 | |
| Zn0.4 | 0.61 | 0.99 | 0.39 | 38.8 | 1.59 | |
| Zn0.5 | 0.53 | 1.02 | 0.48 | 47.5 | 1.66 | |
| Zn0.6 | 0.44 | 1.02 | 0.58 | 57.0 | 1.72 | |

### 5.2. Crystal chemistry of (Me)-C-A-S-H gels

*The Ca/Si molar ratio*

An apparent equilibrium between a C-S-H or C-A-S-H phase and the reactive solution can be reached within seconds to minutes [69], which is in line with the results obtained in this study. As for the reference material, the final Ca/Si molar ratio of the solid was calculated to be about 0.92 (Ca/Al+Si=0.88), thus slightly lower than the target value of Ca/Si = 1. Baldermann et al. [26] and L'Hôpital et al. [46] obtained values of 0.95 and 0.94 for materials precipitated at comparable initial (Ca/Si+Al) molar ratios (see Table AP 2). Also, the aqueous concentrations of Ca and $Si(OH)_4$ as well as the solution pH measured at apparent chemical steady state with the C-A-S-H materials were rather similar between this study and Baldermann et al. [26]: the molar Ca/Si ratio in solution varied between 5.6 to 7.6 and the difference in pH was only about 0.1-0.6 pH units (see Table AP 2). However, in the study of

L´Hôpital et al. [46] the cation concentrations in solution at equilibrium seemed to be somewhat lower (2.1 mM/L for Ca and 1.15 mM/L for Si), while the Ca/Si molar ratio in the reactive solution was found to be higher (14.0) as was the pH value (11.8). These overall small differences might arise from variations in the experimental conditions used [37], [66]. As expected, the Ca/Si molar ratio in solids derived from experiments conducted with Me showed a systematic decrease as the initial Me concentration was increased (see Figure 14). In C-S-H and C-A-S-H systems without Me, such decreased Ca/Si molar ratio in the solid would suggest the co-existence of amorphous silica [37], as indicated by FTIR data [37] [70]. As for this study, no unambiguous indication of formation of amorphous silica was found, although the occurrence of minor amounts of this phase cannot be fully excluded. Indeed, the obtained mineralogical and chemical results clearly reveal that Ca was preferentially substituted by Me, forming Me-bearing C-A-S-H gels with molar (Ca+Me)/(Si+Al) ratios of 0.88-1.02, typical for tobermorite-type phases.

### *The fate of Na and Cl*

Due to the sol-gel procedure used in this study, Na and Cl were introduced into the system. However, almost no Na was incorporated into the precipitates. Thus, Na remained almost quantitatively in the liquid phase, which demonstrates the conservative behaviour of this element. Garcia – Lodeiro et al. [71] have observed that N-A-S-H gel can be formed in the presence of aqueous Na, however, at high pH values, as achieved in this study, the formation of C-A-S-H is favoured over N-A-S-H. Apart from that alkali cations, such as $Na^+$, can be barely incorporated in the interlayer to account for the charge balance particularly in high $Al^{3+}$-substituted C-A-S-H gels [38]. As seen from this study, virtually no Na was incorporated in the C-A-S-H structure as the Al-load in the C-A-S-H gels was very low (Al/Si = 0.05). Chlorine was also not integrated in the precipitating (Me)-C-A-S-H phases, which indicates that this element exhibits a conservative behaviour, as Na did. However, precipitates from the Cu-series contained the mineral phase atacamite [$Cu_2(OH)_3Cl$].

### *Me incorporation in C-A-S-H gels*

Heavy metal ions, such as Zn, Co and with limitations also Cu, were preferentially incorporated in the C-A-S-H gels, as indicated by XRD, ESEM and TEM results. The divalent metals substituted mainly for the $Ca^{2+}$ position in the CaO layer of the C-A-S-H structure, as it is indicated by the cross-plot of the molar ratios of Ca/(Al+Si) and Me/(Al+Si) shown in Figure 14. Due to the fact that no other mineral phases containing Me were found in most of the precipitates (except for atacamite in the Cu-series and eventually $Co(OH)_2$ in the Co-series at high Me/Si ratios), it might be inferred that Me-C-A-S-H phases form a solid solution. Stumm [39] found that Zn can be successfully incorporated into C-S-H. However, he excluded the idea of isomorphic substitution of $Zn^{2+}$ for tetrahedral Si, even though such environments can exist in C-S-H and C-A-S-H structures. Instead, Stumm [39] concluded that Si-O-Zn bonds beside Si-O-Si and Si-O-Ca bonds dominate in C-S-H, which indicates that Zn incorporation in C-S-H follows uptake in tetrahedral coordination into the interlayer, but not in the CaO-layer. This contrasts the results obtained in this study, where clear evidence for significant Zn substitution in the CaO layer is provided, although a minor occupancy of Zn in tetrahedral and interlayer sites is possible. In the case of Cu and Co, isomorphic substitution in the CaO layer is clearly indicated by the data (Fig. 14). The deviation from the ideal 1:1 substitution line of C-A-S-H from this study shown in Figure 14 could be explained by the formation of traces of Me-bearing co-precipitates, although no mineralogical evidence for their existence was found at low Me/Si molar ratios. Alternatively, Me-complexation and sorption onto C-A-S-H surfaces could result in the relatively higher amounts of Me and Ca than suggested by 1:1 isomorphic substitution [50]. In addition, the presence of minor amounts of Ca-bearing phases, such as carbonates, could explain the enrichment of Ca and Me relative to ideal tobermorite. Finally, it is possible that jennite-type C-A-S-H proto-structures formed very early in the experiments, as discussed in section 5.1, which has a higher (Ca+Me)/Si ratio than the ideal tobermorite member. All Me-C-A-S-H gels experienced a decrease in crystallinity with increasing initial Me concentration (see Figure 7). This is consistent with previous results, where increased Ca/Si molar ratios in C-S-H phases and omitted $Q_2(b)$ positions resulted in a structural breakdown of C-S-H [40]. As the amount of structural bound Ca correlates inversely with Me and as this substitution is linear (see Figure 14) it can be inferred that an increasing Me/Si molar ratio affects the linkage to the tetrahedral network in the same way, meaning that polymerization degree of the dreierketten chains is reduced, e.g. some of the $Q_2(b)$ positions are omitted and the $Q_3$ sites may be distorted. This effect was also reported by [26] and [50] and might be an indication for the preferred incorporation of Me into C-A-S-H structures causing a lower crystallinity degree. Generally, Ca in tobermorite like C-(A)-S-H phases occurs in the interlayer as well as in the CaO layer. As for the uptake of hydrated Cr by C-S-H, mechanisms like absorption onto the surface of C-S-H phases, complexation with tetrahedral bound O atoms, but also substitution for Ca in the interlayer and CaO layer were proposed [50]. In the present case, however, no change in the Me-C-A-S-H (hk0) cell dimension was observed, which would be expected if the (hydrated) Me predominantly substitutes for Ca in the interlayer [26]. Me ions thus preferentially occupy positions in the CaO layer.

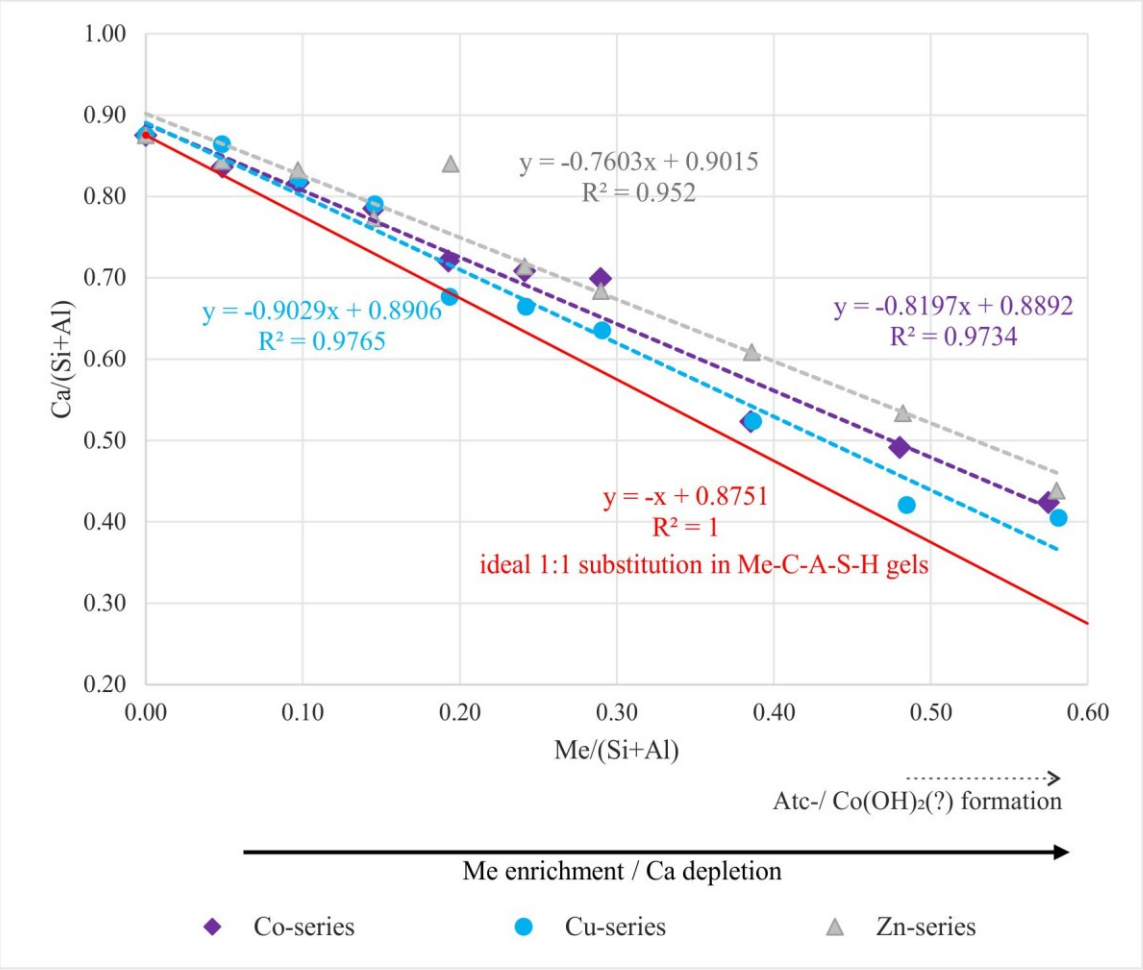

Figure 14: Substitution of Ca by Me in synthetic Me-C-A-S-H phases.

*Me threshold for (Me)-C-A-S-H*

Within the system $CaO-SiO_2-H_2O$, the molar Ca/Si ratio ranges from 0.6 to 1.5 for C-S-H gels [40], [43]. The respective pH value of the solution in equilibrium with such phases ranges from about 10.0 to 12.3, which denotes the stability field of pure C-S-H [37]. Aluminium, up to a molar ratio of about 0.1, can substitute for Si in tetrahedral position to form C-A-S-H structures [43]. As discussed above, Me can readily substitute for Ca in the C-A-S-H system to form a single phase Me-C-A-S-H gel. However, the obtained data indicate that the latter substitution is limited, meaning that a certain threshold value for Me uptake by C-S-H and C-A-S-H phases exists.

Stumm [39] found that in the case of 25 % substitution of $Ca^{2+}$ by $Zn^{2+}$, which equals a molar Me/Si ratio of about 0.15 in the present study, zincite (ZnO) formed. However, for the synthesis and preparation of the material a different experimental setup, drying at elevated temperatures (60 °C) as well as a lower initial Ca/Si molar ratio was used [39]. In Baldermann et al. [26] and in this study neither the formation of ZnO nor $Zn(OH)_2$ could be observed, suggesting that Zn is structurally bound in C-A-S-H. Indeed, a decrease in crystallinity correlated well with the increase in the Zn content, up to molar Zn/Si ratios of 0.6, in (Me)-C-A-S-H. This indicates further that the threshold for Zn uptake by C-A-S-H is greater than 0.6.

The determination of the threshold value for Co incorporation in C-A-S-H may arise from the analysis of the XRD data, where mineral phase segregation was evident at a molar Co/Si ratio of about 0.3 and higher. Although it was impossible to precisely identify the nature of the discrete Co-bearing mineral phases it is most likely that two coexisting C-A-S-H phases, one being relatively enriched in Co, or $Co(OH)_2$ are formed. Co-complexes can exhibit a variety in colour due to electronic and orbital changes of Co during coupling with a ligand [72]. During the experiment a transition in colour of the precipitates, from bluish (for solids with lower Co/Si molar ratios) to pinkish (for solids with higher Co/Si ratios), was observed, with the latter probably coming from $Co(H_2O)_6^{2+}$ complex formation [73] that attaches onto the surface of C-A-S-H as soon as no more Co could be incorporated in the C-A-S-H crystal lattice. Also, $\beta$-$Co(OH)_2$ is known for its pinkish color [62].

The occurrence of single phase Cu-C-A-S-H is limited by the formation of atacamite, which was detected at a molar Cu/Si ratio of about 0.3. However, minor amounts of atacamite were probably precipitated already at a Cu/Si molar ratio of 0.2, as indicated by the XRD data. In the absence of $Cl^-$, Stumm [39] observed the formation of tenorite (CuO) and Cu-free C-S-H already at relatively low initial Cu/(Cu+Ca) ratios of 0.01, and proposed that (at least with a mechanochemical experimental method) no Cu-bearing C-S-H substance can be formed [39]. From the element distribution mappings of Cu, Ca and O (based on TEM-EELS) in Cu0.5 it can be seen that these elements are evenly distributed in the C-A-S-H matrix, which indicates that Cu can be incorporated in C-A-S-H structural sites (see Figure 15). Areas enriched in Cu belong to atacamite. Therefore, it can be reasonable assumed that Cu incorporation into C-A-S-H structures is possible, at least up to a molar Cu/Si ratio of 0.2, without co-precipitation of other Cu-bearing phases. At higher molar Cu/Si ratios, some Cu may be also bound in C-A-S-H structures, but the relative amount of atacamite increases significantly as more Cu is introduced to the system.

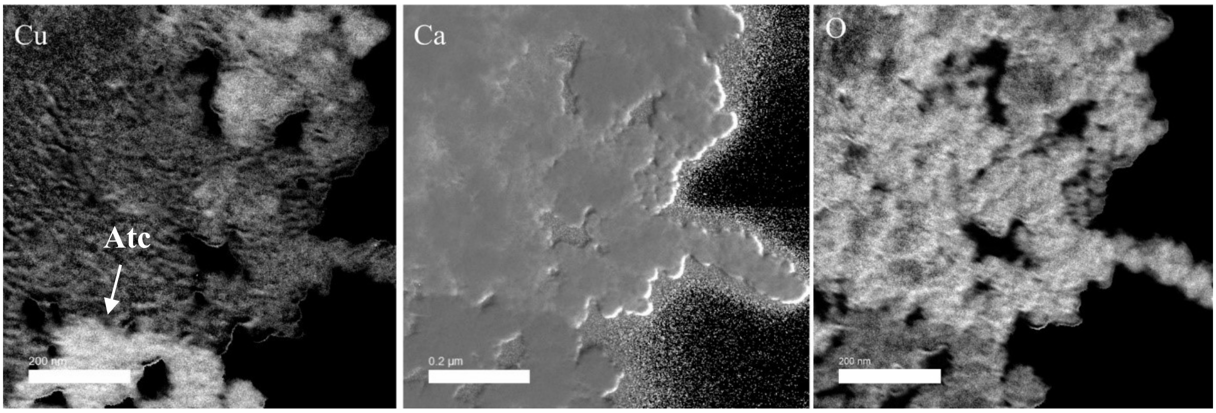

Figure 15: TEM-EELS based element distribution mappings of Cu, Ca and O for sample Cu0.5.

*Water content in Me-C-A-S-H gel*

Water within C-S-H or C-A-S-H can occur as (i) $H_2O$ molecules confined within the interlayer, (ii) hydroxyl groups or $H_2O$ molecules bound to aqueous cationic species within the interlayer and (ii) hydroxyl groups bound to the tetrahedral framework (i.e. silanol groups). The calculated mole proportion of water in the C-A-S-H gel (1.35) without Me is in accordance with previously published values, which is 1.32 for a C-S-H phase with a Ca/Si ratio of 0.85 [37]. The higher the Ca content, the higher is the water content in the C-S-H phase [37]. A slight increase of the Ca/Si ratio from 0.85 to 1.05 shifts the molar water content from 1.3 to 1.5 [37], which is consistent with the results obtained in the present study, if considering that Co and Zn substitute for Ca. The Cu-series is an exception and exhibits a rather high water content of $H_2O/Si$ of 2.1 at molar (Ca+Me)/(Al+Si) ratio of 0.91, which could be due to the presence of atacamite. For C-A-S-H with a molar Ca/(Si+Al) ratio of 0.94, synthesized at 20 °C, a structural water content of 1.4 has been reported [75].

Generally, an increasing Ca/Si ratio in C-S-H and C-A-S-H is associated with the depolymerisation of the dreierketten chains and a decreasing length of the silicate chains [38]. In this study, a systematic increase in molecular water with increasing Me content in C-A-S-H was observed (from 1.3 up to 2.1), which resulted in a decreasing crystallinity degree and a particle size reduction of Me-C-A-S-H. Therefore, it can be reasonably suggested that the substitution of Me over Ca in the Me-C-A-S-H system causes (i) an omission of $Q_b$ positions and thus a lower polymerization degree and (ii) an overall higher specific surface area, where hydrated Me-complexes [38] can get attached onto.

### 5.3. Solubility of Me-substituted C-A-S-H

C-(A)-S-H phases form a continuous series in the range of Ca/Si molar ratios from 1.65 down to 0.55 [37], which strongly affects the solubility of these phases in their compositional series. Solid solution in aqueous solution (SSAS) modelling allows assessing the performance of C-S-H in a hardened cement paste over its lifespan [37]. This knowledge is particularly important when cement based materials are used as confinement barriers in precarious situations, such as in nuclear waste repositories [26], [37], [55], [74] (see discussion below). Although the solubility model of Walker et al. [37] adequately describes the solubility relationships (and stability) of pure C-S-H phases in the range of Ca/Si molar ratios from 0.55 to 1.65, it does not consider the influence of other elements, such as Al and Me, on the solubility of impure C-S-H. Myers et al. [75] prognosticated a lower solubility for C-A-S-H formed at elevated temperatures compared to pure C-S-H and Baldermann et al. [26] argued that a lower solubility probably also applies to Co-, Cr- and Zn-bearing C-A-S-H. However, the magnitude of change in solubility products for C-A-S-H with and without Me has not yet been reported in the scientific literature.

From the chemical compositions of the experimental solutions and related C-A-S-H (with and without Me) obtained at apparent steady state conditions, solubility constants for Me-C-A-S-H phases with molar Me/Si ratios up to 0.6 were calculated. The solubility for pure C-A-S-H is defined according to the equation (2):

$$C_{0.92}A_{0.025}S_1H_{1.33} + 0.67\ H_2O \leftrightarrow 0.92\ Ca^{2+} + 0.05\ Al(OH)_4^- + SiO(OH)_3^- + 0.8(OH)^- \qquad (2)$$

where C = CaO, A = $Al_2O_3$, S = $SiO_2$ and H = $H_2O$, and for Me-bearing C-A-S-H (with Me = Co0.05) it follows the equation (3):

$$Co_{0.05}C_{0.86}A_{0.025}S_1H_{1.35} + 0.6\ H_2O \leftrightarrow 0.86\ Ca^{2+} + 0.05Co^{2+} + 0.05\ Al(OH)_4^- + 1SiO(OH)_3^- + 0.78\ (OH)^- \qquad (3)$$

where Co = CoO. Note that thermodynamic equilibrium conditions are required for solving the solubility equations. Therefore, chemical steady state conditions, as obtained after 10-30 min of reaction time in all experiments, are concluded to represent these conditions. Also, fully isomorphic substitution of Ca by Me (see Figure 14) is taken into account. The solubility constants ($K$) were calculated according to equation (4):

$$K = \frac{\sum a_{product}^{n}}{\sum a_{educt}^{n}} \tag{4}$$

where $a_{product}$ is the activity of the product species, $a_{educt}$ is the activity of the educt species and $n$ denotes the mole proportion of the relevant species according to the equations (3) and (4), respectively. Under the given experimental conditions, the activity of $H_2O$ and of C-A-S-H with(out) Me is assumed to be 1, thus the ion activity product (IAP) for C-A-S-H formation was determined as equation (5):

$$K = (Ca^{2+})^{0.92} \cdot \left(Al(OH)_4^-\right)^{0.05} \cdot \left(Si(OH)_3^-\right)^{1} \cdot (OH^-)^{0.8} \tag{5}$$

and for Me-bearing C-A-S-H (with Me = Co0.05) it is equation (6):

$$K = (Co^{2+})^{0.05} \cdot (Ca^{2+})^{0.86} \cdot \left(Al(OH)_4^-\right)^{0.05} \cdot \left(Si(OH)_3^-\right)^{1} \cdot (OH^-)^{0.78} \tag{6}$$

The results of the solubility constants calculations for the reference material and for Me-C-A-S-H phases with molar Me/Si ratios of 0.3 for Co and Cu up to 0.6 for Zn are provided in Table AP 8. A comprehensive presentation of $K_{SP}$ vs. (Ca+Me)/(Si+Al), Me/(Si+Al) and pH in combination with data from the literature ([37], [75]) is given in Figure 16. Walker et al. [37] reported a $\log K_{SP}$ value of -8.2 for C-S-H with molar Ca/Si ratio of 0.85, which is quite similar to the $\log K_{SP}$ value of -8.3 derived from this study for pure C-A-S-H with a Ca/Si ratio of 0.92 and Al/Si ratio of 0.05. The $\log K_{SP}$ values for Me-doted C-A-S-H are generally lower by about half up to six orders of magnitude (~-8.5 up to -14.1) compared to the pure phase and as the Me concentration increases. However, it is worth mentioning that the determination of the amount of structural bound water in Me-C-A-S-H is analytically challenging and that minor amounts of co-precipitates could be present in the samples, which both affect the $\log K_{SP}$ values.

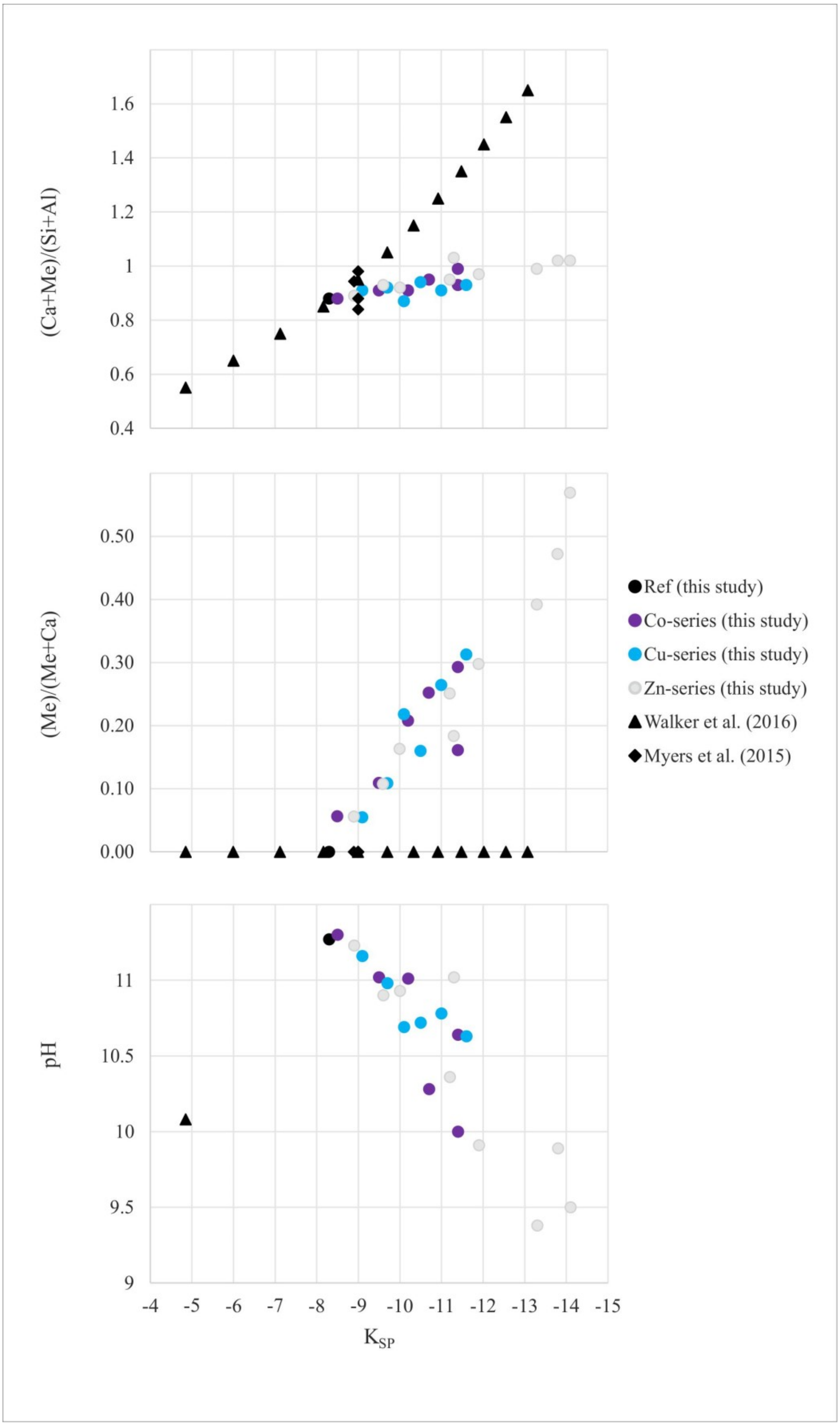

Figure 16: Calculated solubility products ($K_{SP}$) for Me-C-A-S-H compared to reported C-(A)-S-H data from the literature [37][75].

## 5.4. Me-C-A-S-H phases in waste management technologies

The chemical/mechanical resistance and leachability of C-S-H and C-A-S-H are important factors in waste management, as cementitious materials are nowadays successfully used in e.g. toxic waste solidification/stabilization (S/S) technologies [7][9]-[14]. During lifetime, the matrix of Me-bearing S/S waste undergoes various aging and alteration processes, which cause a large variety of chemical compositions of C-(A)-S-H due to e.g. decalcification, leaching and carbonation processes [15]. The subsequent loss in Ca greatly influences the solubility of C-(A)-S-H, as indicated earlier, i.e. a lower Ca content in C-S-H increases the solubility [37]. If the landfilled S/S toxic waste comes in contact with aggressive, e.g. low mineralized or acidic, water from the outer environment, the modified and aged C-(A)-S-H will dissolve rapidly [16]. As a consequence, toxic wastes could be released back into the aquatic and terrestrial environments, such as soils and groundwater.

However, it was already shown that Me-bearing (Me = Fe) cement pastes experienced a slower degradation due to leaching, compared to pure Ca-based systems [16]. On the other hand, Contessi [7] figured out that untreated contaminated soil exhibited a lower Me leachability in acidic environments than S/S-modified soil in the short-term, although on the long-term the S/S material performed better as the leachability decreased over time, in contrast to the untreated soil. The results obtained in this study support this first viewpoint. Moreover, they clearly document that Co-, Cu- and Zn-containing C-A-S-H waste have a much lower solubility and hence a higher resistance against leaching, which is in agreement with Żak & Deja [14]. However, note that the uptake of Me by C-A-S-H gels is selective and follows the order: Cu < Co < Zn. Accordingly, Cu is less incorporated into the C-A-S-H structure and thus probably exhibits a higher mobility than Co and Zn in aqueous systems.

In groundwater treatment scenarios, cementitious modules are increasingly more considered for the remediation of Me-loaded waters derived from human activities, such as raw material exploitation [5], [8]. Permeable reactive barriers [8], for example, have been installed in the last decades in many locations worldwide as part of the aquifer in the sub ground. C-S-H phases present in the concrete matrix of such materials are therefore exposed to subsequent leaching processes due to permanent (ground)water flow through the barrier [16]. During interaction of the mostly acidic (ground)water with the perforated alkaline modules, spatiotemporal changes in solution pH (i.e. pH buffering) and in the solute concentrations (Me, Ca, Al, Si) are expected. Under such conditions, Me tend to be immobilized, e.g. by the precipitation of secondary Me-bearing mineral phases [8]. In order to account for an efficient remediation process it is important that these newly formed minerals exhibit a high retention potential for Me. Especially poorly crystallized C-(A)-S-H gels, such as obtained during this study, seem to have high Me uptake capacities [3]. A similar conclusion was drawn by Faucon et al. [16], who have shown that C-S-H developed in a degraded concrete layer in contact with a corrosive aqueous solution preferentially incorporated Me ions, such as $Fe^{3+}$ [16], which slowed down the degradation kinetics of the concrete barrier.

The accurate assessment of the performance of low- and deep-seated radioactive waste repositories also requires a fundamental knowledge about C-(A)-S-H phase solubility in concrete structures [15][16][17]. Radioactive waste disposal sites are designed as multi-layer structures, where a concrete vault is mantled by a clay layer, such as bentonite [15], [55]. This often called multi-barrier system is prone to multi-faceted chemical reactions (e.g. dissolution and formation of secondary phases [55], [77], [78]), particularly at solid-liquid interfaces, where strong gradients in pH and in the solute concentrations are developing. Hardened cement paste, for instance, is equilibrated with a highly alkaline pore solution at pH $\approx$12 [17], [79], whereas the pH of bentonite-derived solutions is typically much lower, e.g. ~9.5 [76]. Furthermore, ion exchange reactions and diffusion processes take place at the concrete-bentonite interface, during which the concrete buffer loses Ca and strength and the bentonite buffer frequently sees a reduction in the swelling pressure due to Na for Ca exchange in the interlayer of montmorillonite, that is, the main constituent in commercial bentonite [16]. The micro-environment developing between the modified bentonite and concrete is usually beneficial for the formation of C-A-S-H, which incorporates Me released from the degraded clay or the waste [15]. As seen from this study, such newly formed Me-C-A-S-H phases are stable down to pH $\sim$10.5 (see Figure 16). Below this threshold value for pH, Me-C-A-S-H phases will start dissolving and Me ions could be released back to the environment, if no other removal mechanisms are active. In essence, the fact that C-A-S-H structures can easily incorporate Me ions in large quantities, such as Co, Cu and Zn, and that the solubility of Me-C-A-S-H is orders of magnitude lower than that of pure C-A-S-H allows concluding that Me-C-A-S-H act both as a physical and chemical barrier for Me ions.

## Summary and Conclusions

Calcium aluminium silicate hydrate (C-A-S-H) gels were synthesized at room temperature using Me/Si molar ratios from 0.0 up to 0.6 (Me = Cu, Co or Zn) and a constant Al/Si molar ratio of 0.05. The following conclusions can be drawn:

1) A near equilibrium stage between reactive solution and Me-C-A-S-H gels was reached after about 10-30 minutes of reaction time. At the end of the experiments after 1 hour, removal efficiencies of nearly 100 mol% were reached for Al, Si and Me, whereas Ca was reduced by 5 to 57 % as the Me concentration increased.

2) During the early precipitation period (i.e. within the first minutes), the aqueous Ca/Si ratio decreased strongly, indicative of formation of a jennite-type C-A-S-H phase. This reactive intermediate was then transformed (via dissolution/re-precipitation) into a tobermorite-type C-A-S-H phase as the reaction continued and as Ca was released back to the solution.

3) The colour of the precipitates was strongly dependent on the type of Me incorporated in the C-A-S-H structure, with Co, Cu and Zn yielding pinkish-, bluish- and white-coloured precipitates. These poorly ordered (Me)-C-A-S-H gels had (Me+Ca)/(Si+Al) molar ratios from 0.88 to 1.03. An increasing Me/Si molar ratio in C-A-S-H came along with a higher amount of chemical bound water (17 up to 24 wt%), a lower crystallinity degree and an overall finer particle size (~100 to < 50 nm). The main uptake mechanism of Me is governed by isomorphic substitution for Ca in the CaO layer of C-A-S-H. To further characterize the chemical environment of $Co^{2+}$, $Cu^{2+}$ and $Zn^{2+}$ in the C-A-S-H structure NMR studies have to be carried out.

4) At a Me/Si molar ratio of about 0.3 significant co-precipitation of atacamite was observed for the Cu-series and of poorly crystalline Co-rich C-A-S-H or $Co(OH)_2$ for the Co-series. As for the Zn-series no such additional solid phase formation was observed. Independent of the type of Me used for C-A-S-H synthesis, carbonates such as calcite and monohydrocalcite formed in minor amounts in some of the experiments.

5) The calculated solubility (given as logK) for the pure C-A-S-H is -8.3, consistent with published literature, whereas an increase in the Me/Si ratio in the solids comes along with much lower logK values, i.e. -11.3, - 11.6 and -14.1 for Co0.3, Cu0.3 and Zn0.6, respectively.

6) C-(A)-S-H gels bear high Me immobilization potential which comes along with a favourable low solubility. This is important in wastewater treatment, toxic waste S/S technologies and waste repositories. However, different types of Me do not perform equally within the $CaO – SiO_2 – H_2O$ – system. Further studies on Me incorporation in C-(A)-S-H structures are essential to fully understand the potential, limits and long-term behaviour of Me fixation in C-(A)-S-H gels, in order to make predictions on environmental implications.

## 6. Acknowledgement

Special thanks go to A. Landler, F. Steindl, M. Hierz and A. Wolf (Graz University of Technology) for the assistance during laboratory work. Also, the author is grateful for the support during data acquisition by S. Eichinger, J. Jernej (Graz University of Technology) and I. Letofsky-Papst as well as S. Šimić (Institute for Electron Microscopy and Nanoanalysis and Center for Electron Microscopy). For reviewing thanks go to M. Dietzel. Finally, I want to honour A. Baldermann for all his efforts as supervisor and who assisted me throughout the study to gain my Master's degree.

## 7. References

[1] Achternbosch M., Bräutigam K.-R., Hartlieb N., Kupsch C., Richers U., Stemmermann P., Gleis M. (2003): Heavy metals in cement and concrete resulting from co-incineration of wastes in cement kilns with regard to the legitimacy of waste utilisation; Forschungszentrum Karlsruhe GmbH; Karlsruhe.

[2] Verein Deutscher Zementwerke e. V. (2002): Zement-Taschenbuch 2002; Verlag Bau+Technik GmbH; Düsseldorf.

[3] Coleman N.J., Li Q., Raza A. (2014): Synthesis, structure and performance of calcium silicate ion exchangers from recycled container glass; Physicochem. Robl. Miner. Process, 50(1), 5-16.

[4] Femina Carolin C., Senthil Kumar P., Saravanan A., Janet Joshiba G., Naushad Mu. (2017): Efficient techniques for the removal of toxic heavy metals from aquatic environment: A review; Journal of Environmental Chemical engineering, 5, 2782-2799.

[5] Qi G., Lei X., Li L., Yuan Ch., Sun Y., Chen J., Chen Ji., Wang Y., Hao J. (2015): Preparation and evaluation of a mesoporous calcium-silicate material (MCSM) from coal fly ash for removal of Co(II) from wastewater; Chemical Engineering Journal, 279, 777-787.

[6] Svatovskaya L., shershneva M., Baydarashvily M., Sychova a., Sychov M., Gravit M. (2015): Geoecoprotective Properties of Cement and Concrete against Heavy Metal Ions, Procedia engineering, 117, 345-349.

[7] Contessi S., Calgaro L., Dalconi M. C., Bonetto A., Bellotto M. P., Ferrari G., Marcomini A., Artioli G. (2020): Stabilization of lead contaminated soil with traditional and alternative binders; Journal of Hazardous Materials, 382, 120990.

[8] Shabalala A. N., Ekolu S. O., Diop S., Solomon F. (2017): Pervious concrete reactive barrier for removal of heavy metals from acid mine drainage – column study; Journal of Hazardous Materials, 323, 641-653.

[9] Chiu A. C. F., Akesseh R., Moumouni I. M., Xiao Y. (2019): Laboratory assessment of rice husk ash (RHA) in the solidification/ stabilization of heavy metal contaminated slurry; Journal of Hazardous Materials, 371, 62-71.

[10] Kulik D. A., Kersten M. (2001): Aqueous Solubility Diagrams for Cementitious Waste stabilization systems: II, End-Member Stoichiometries of Ideal Calcium Silicate Hydrate Solid Solutions, J. Am. Ceram. Soc., 84 [12], 3017-26.

[11] Papandreou A., Stournaras C. J., Panias D. (2007): Copper and cadmium adsorption on pellets made from fired coal fly ash; Journal of Hazardous Materials, 148, 538-547.

[12] Park Ch.-K. (2000): Hydration and solidification of hazardous wastes containing heavy metals using modified cementitious materials; Cement and Concrete Research, 30, 429-435.

[13] Yousuf M., Mollah A., Vempati R. K., Lin T.-C., Cocke D. L. (1995): The interfacial chemistry of solidification/stabilization of metals in cement and pozzolanic material systems; Waste Management, 15 (2), 137-148.

[14] Żak R., Deja J. (2015): Spectroscopy study of Zn, Cd, Pb and Cr ions immobilization on C-S-H phase; Spectrochimica Acta Part A: Molecular and Biomolecular Spectroscopy, 134, 614-620.

[15] Fernández R., Ruiz A.I., Cuevas J. (2016): Formation of C-A-S-H phases from the interaction between concrete or cement and bentonite; Clay Minerals, 51, 223-235.

[16] Faucon P., Adenot f., Jacquinot J. F., Petit J. C., Cabrillac R., Jorda M. (1998): Long-term behaviour of cement pastes used for nuclear waste disposal: Review of physico-chemical mechanisms of water degradation; Cement and Concrete Research, 28 [6], 847-857.

[17] Haga K., Sutou S., Hironaga M., Tanaka S., Nagasaki S. (2005) Effects of porosity on leaching of Ca from hardened ordinary Portland cement paste; Cement and Concrete Research, 35, 1764-1775.

[18] Friembichler F., Spaun S., Steigenberger J., Huber F., Jus U., Stuzka C., Malina U. (2012): Zement, Zementerzeugung in Österreich; Zement+Beton Handels- und Werbeges.m.b.H (Hrsg.); Wien.

[19] Vereinigung der Österreichischen Zementindustrie, VÖZ (Juli 2019): Zementindustrie: Vorreiter und Visionär in puncto Klimaschutz, Pressemeldungen; Wien; source: https://www.zement.at/services/presse/58-2019/555-zementindustrie-vorreiter-und-visionaer-in-puncto-klimaschutz (09.10.2019).

[20] Schneider M., Mohr M. (2018): Zementindustrie im Überblick 2018/2019; Verein Deutscher Zementwerke e. V. (Hrsg.); Berlin.

[21] Statista (2019): Produktion von Zement nach den wichtigsten Ländern weltweit im Jahr 2018* (in Millionen Tonnen); US Geological Survey.

[22] Liu X., Zhao X., Yin H., Chen J., Zhang N. (2018): Intermediate-calcium based cementitious materials prepared by MSWI fly ash and other solid wastes: hydration characteristics and heavy metals solidification behavior; Journal of Hazardous Materials, 349, 262-271.

[23] Mangialardi T. (2003): Disposal of MSWI fly ash through a combined washing-immobilisation process; Journal of Hazardous Materials, B98, 225-240.

[24] Aubert J. E., Husson B., Sarramone N. (2007): Utilization of municipal waste incineration (MSWI) fly ash in blended cement – Part 2. Mechanical strength of mortars and environmental impact; Journal of Hazardous Materials, 146, 12-19.

[25] Sprung S., Rechenberg W. (1989): Einbindung von Schwermetallen in Sekundärstoffen durch Verfestigung mit Zement; nach einem Vortrag auf der technisch-wissenschaftlichen Zementtagung `88 des VDZ am 20/21. Januar 1988 in Düsseldorf.

[26] Baldermann A., Landler A., Mittermayr F., Letofsky-Papst I., Steindl F., Galan I., Dietzel M. (2019): Removal of heavy metals (Co, Cr, and Zn) during calcium-aluminium-silicate-hydrate and trioctahedral smectite formation; J Mater Sci, 54, 9331-9351.

[27] Chen Q.Y., Tyrer M., Hills C.D., Yang X.M., Carey P. (2009): Immobilisation of heavy metal in cement-based solidification/stabilisation: A review; Waste Management, 29, 390-403.

[28] Dermatas D., Meng X. (2003): Utilization of fly ash for stabilization/solidification of heavy metal contaminated soils; Engineering Geology, 70, 377-394.

[29] Giergiczny Z., Król A. (2008): Immobilization of heavy metals (Pb, Cu, Cr, Zn, Cd, Mn) in the mineral additions containing concrete composites; Journal of Hazardous Materials, 160, 247-255.

[30] Garbev, K. (2004): Struktur, Eigenschaften und quantitative Rietveldanalyse von hydrothermal kristallisierten Calciumsilikathydraten (C-S-H-Phasen); Inaugural- Dissertation, Universität Heidelberg.

[31] Grutzeck M., Benesi A., Fanning B. (1989): Silicon-29 Magic Angle Spinning Nuclear Magnetic Resonance Study of Calcium Slicate Hydrates; Journal of the American Ceramic Society, 72 [4], 665-68.

[32] Jennings H. M. (2000): A model for the microstructure of calcium silicate hydrate in cement paste; Cement and Concrete Research, 30, 101-116.

[33] Renaudin G., Russias J., Leroux F., Cau-dit-Coumes C., Frizon F. (2009): Structural characterization of C-S-H and C-A-S-H samples – Part II: Local environment investigated by spectroscopic analyses; Journal of Solid State Chemistry, 182, 3320-3329.

[34] Roosz C., Vieillard P., Blanc P. Gaboreau S., Gailhanou H., Braithwate D., Montouillout V., Denoyel R., Henocp P., Madé B. (2018): Thermodynamic properties of C-S-H, C-A-S-H and M-S-H phases: Results from direct measurements and predictive modelling; Applied Geochemistry, 92, 140-156.

[35] Shaw S., Clark S.M, Henderson C.M.B. (2000): Hydrothermal formation of the calcium silicate hydrates, tobermorite ($Ca_5Si_6O_{16}(OH)_2 \cdot 4\,H_2O$) and xonolite ($Ca_6Si_6O_{17}(OH)_2$) an in situ synchrotron study; Chemical Geology, 167, 129-140.

[36] Sun G.K., Francis Young J., James Kirkpatrick R. (2006): The role of Al in C-S-H: NMR, XRD, and compositional results for precipitated samples; Cement and Concrete Research, 36, 18-29.

[37] Walker C. S., Sutou S., Oda C., Mihara M., Honda A. (2016): Calcium silicate hydrate (C-S-H) gel solubility data and a discrete solid phase model at 25°C based on two binary non-ideal solid solutions. Cement and Concrete Research, 79, 1-30.

[38] Walkley B., Provis J.L. (2019): Solid-state nuclear magnetic resonance spectroscopy of cements; Materials Today Advances, 1, 100007.

[39] Stumm A. (2004): Struktureller Einbau von Zink in Calciumsilikathydrate mit einem C/S < 1 und unterschiedlichem Kristallisationsgrad; Dissertation zur Erlangung des akademischen Grades eines Doktors der Naturwissenschaften von der Fakultät für Bauingenieur-, Geo- und Umweltwissenschaften der Universität Fridericiana zu Karlsruhe (TH).

[40] Cong X., Kirkpatrick R. J. (1996): $^{29}$Si MAS NMR Study of the Structure of Calcium Silicate Hydrate; Advanced Cement Based Materials, 3, 144-156.

[41] Myers R. J., Bernal S. A., Nicolas R. S., Provis J. L. (2013): Generalized Structural Description of Calcium – Sodium Aluminosilicate Hydrate Gels: The Cross-Linked Subtituted Tobermorite Model; Langmuir, 29, 5294-5306.

[42] Taylor H. F. W. (1986): Proposed Structure for Calcium Silicate Hydrate Gel; Journal of the American Ceramic Society, 69 [6], 464-67.

[43] L´Hôpital E., Lothenbach B., Le Saout G., Kulik D.A., Scrivener K. (2015): Incorporation of aluminium in calcium-silicate-hydrates; Cement and Concrete Research, 75, 91-103.

[44] McConnell, J. D. C. (1954): The hydrated calcium silicate riversideite, tobermorite, and plombierite; Mineralogical Magazine and Journal of the Mineralogical Society, 30, 293-305.

[45] Merlino S., Bonaccorsi E., Armbruster T. (2001): The real structure of tobermorite 11Å: normal and anomalous forms, OD character and polytypic modifications; European Journal of Mineralogy, 13, 577-590.

[46] L´Hôpital E., Lothenbach B., Kulik D.A., Scrivener K. (2016): Influence of calcium to silica ratio on aluminium uptake in calcium silicate hydrate; Cement and Concrete Research, 85, 111-121.

[47] Baltakys K., Eisinas A., Doneliene J., Dambrauskas T., Sarapajevaite G. (2019): The impact of $Al_2O_3$ amount on the synthesis of CASH samples and their influence on the early stage hydration of calcium aluminate cement; Ceramics International 45, 2881-2886.

[48] Bernard E., Lothenbach B., Cau-Dit-Coumes C., Chlique C., Dauzères A., Pochard I. (2018): Magnesium and calcium silicate hydrates, Part I: Investigation of the possible magnesium incorporation in calcium silicate hydrate (C-S-H) and of the calcium in magnesium silicate hydrate (M-S-H); Applied Geochemistry, 89, 229-242.

[49] Ziegler Felix, Scheidegger André M., Johnson Annette C., Dähn Rainer, Wieland Erich (2001): Sorption Mechanisms of Zinc to Calcium Silicate Hydrate: X-ray Absorption Fine Structure (XAFS) Investigation. Environmental Science and Technology, 35, 1550-1555.

[50] Zhao Z., Wei J., Li F., Qu X., Shi L., Zhang H., Yu Q. (2017): Synthesis, Characterization and Hexavalent Chromium Adsorption Characteristics of Aluminum- and Sucrose- Incorporated Tobermorite; Materials, 10, 597.

[51] Mancini A., Wieland E., Geng G., Dähn R., Skibsted J., Wehrli B., Lothenbach B. (2019): Fe (III) uptake by calcium silicate hydrates; Applied Geochemistry, 104460.

[52] Institute of Applied Geosciences, IAG (2019): https://www.tugraz.at/institute/iag/home/; accessed on 12.04.2019.

[53] Baldermann A., Grießbacher A.C., Baldermann C., Purgstaller B., Letofsky-Papst I., Kaufhold S., Dietzel M. (2018): Removal of barium, cobalt, strontium, and zinc from solution by natural and synthetic allophane adsorbents; Geosciences, 8:309.

[54] Steindl F. (2017): Combination of minteqv4 and CEMDATA07.

[55] Diederik J. (2009): Benchmarking of the cement model and detrimental chemical reactions including temperature dependent parameters – Project near surface disposal of category A waste at Dessel – NIRAS-MP5-03 DATA-LT(NF) Version 1, NIROND-TR 2008-30 E.

[56] García-Lodeiro I., Fernández-Jiménez A., Blanco M. T., Palomo A. (2008): FTIR study of the sol-gel synthesis of cementitious gels: C-S-H and N-A-S-H; Journal of Sol-Gel Science and Technology, 45, 63-72.

[57] Yu P., Kirkpatrick R., J., Poe B., McMillan P. F., Cong X. (1999): Structure of Calcium silicate Hydrate (C-S-H): Near-, Mid-, and Far-Infrared Spectroscopy; Journal of the American Ceramic Society, 82 [3], 742-748.

[58] Martens W., Frost R. L., Williams P. A. (2003): Raman and infrared spectroscopic study of the basic copper chloride minerals – implications for the study of the copper and brass corrosion and “bronze disease”; Neues Jahrbuch für Mineralogie Abhandlungen, 178, 197-215.

[59] Stepkowska E. T., Aviles M. A., Blanes J. M., Perez-Rodriguez J. L. (2007): Gradual transformation of $Ca(OH)_2$ into $CaCO_3$ on cement hydration – XRD study; Journal of Thermal Analysis and Calorimetry, 87 [1], 189-198.

[60] Stokes D.J. (2013): Environmental scanning electron microscopy (ESEM): principles and applications to food microstructures; Woodhead Publishing Limited.

[61] Zentrum für Elektronenmikroskopie, ZFE (2019): Austrian Centre for Electron Microscopy and Nanoanalysis, FELMI-ZFE. https://www.felmi-zfe.at; accessed on 23.05.2019.

[62] Huang Z., Zhao Y., Song Y., Li Y, Wu G., Tang H., Zhao J. (2016): Study on the oxidation process of cobalt hydroxide to cobalt oxides at low temperatures; The Royal Society of Chemistry Advances, 6, 80059-80064.

[63] Zhu Y., Li H., Koltypin Y., Gedanken A. (2002): Preparation of nanosized cobalt hydroxides and oxyhydroxide assisted by sonication; Journals of Materials Chemistry, 12, 729-733.

[64] Gao X., Yu Q.L., Brouwers H.J.H. (2015): Reaction kinetics, gel character and strength of ambient temperature cured alkali activated slag-fly ash blends; Construction and Building Materials, 80, 105-115.

[65] Vollpracht A. (2012): Einbindung von Schwermetallenin Portlandzementstein; Von der Fakultät für Bauingenieurwesen der Rheinisch-Westfälischen Technischen Hochschule Aachen zur Erlangung des akademischen Grades einer Doktorin der Ingenieurwissenschaften genehmigte Dissertation.

[66] Wang H., Wang Y., Cui S., Wang J. (2019): Reactivity and Hydration Property of Synthetic Air Quenched Slag with Different Chemical Compositions; materials, 12, 932.

[67] Murzyn P., Malata G., Wi´sniewska J., Kapeluszna E., Nocu´n-Wczelik W. (2019): Characterization of 40-year-old calcium silicate pastes by thermal methods and other techniques; Journal of Thermal Analysis and Calorimetry.

[68] Yang J., Li D., Fang Y. (2017): Synthesis of Nanoscale CaO-Al2O3-SiO2-H2O and Na2O-Al2O3-SiO2-H2O Using the Hydrothermal Method and Their Characterization; Materials, 10, 695.

[69] Jennings H. M. (1986): Aqueous Solubility Relationships for Two Types of Calcium Silicate Hydrate; Journal of the American Ceramic Society, 69 [8], 614-618.

[70] Walker C. S., Savage D., Tyrer M., Vala Ragnarsdottir K. (2007): Non-ideal solid solution aqueous solution modeling of synthetic calcium silicate hydrate; Cement and Concrete Research, 37, 502-511.

[71] Garcia-Lodeiro I., Palomo A., Fernández-Jiménez A., Macphee D.E. (2011): Compatibility studies between N-A-S-H and C-A-S-H gels. Study in the ternary diagram Na2O–CaO–Al2O3–SiO2–H2O; Cement and Concrete Research, 41, 923-931.

[72] Riordan A. R., Jansma A., Fleischman S., Green D. B., Mulford D. R. (2005): Spectrochemical series of Cobalt (III). An Experiment for High School through College; Chemical Educator, 10, 115-119.

[73] Nuffield Foundation and the Royal Society of Chemistry (2018): The equilibrium between two coloured cobalt species; https://edu.rsc.org/resources/the-equilibrium-between-two-coloured-cobalt-species/1.article, last accessed on 06.11.2019.

[74] Galíndez J. M., Molinero J. (2010): Assessment of the long-term stability of cementitious barriers of radioactive waste repositories by using digital-image-based microstructure generation and reactive transport modelling; cement and Concrete Research, 40, 1278-1289.

[75] Myers R. J., L'Hôpital E., Provis J. L., Lothenbach B. (2015): Effect of temperature and aluminium on calcium (alumino)silicate hydrate chemistry under equilibrium conditions; Cement and Concrete Research, 68, 83-93.

[76] Ouhadi V.R., Yong R.N., Sedighi M. (2006): Desorption response and degradation of buffering capability of bentonite, subjected to heavy metal contaminants; Engineering geology, 85, 102-110.

[77] Fernández R., Rodríguez M., Vigil de la Villa R., Cuevas J. (2010): Geobhemical constraints on the stability of zeolites and C-S-H in the high pH reaction of bentonite; Geochimica et Cosmochimica Acta, 74, 890-906.

[78] Han J., Sun W., Pan G., Caihui W. (2013): Monitoring the Evolution of Accelerated Carbonation of Hardened Cement Pastes by X-Ray Computed Tomography; Journal of Materials in Civil Engineering, 25 [3], 347-354.

[79] Promentilla M. A. B., Sugiyama T., Hitomi T., Takeda N. (2008): Characterizing the 3D Pore Structure of Hardened Cement Paste with Synchrotron Microtomography; Journal of Advanced Concrete Technology, 6 [2], 273-286.

[80] Harris A. W., Manning M. C., Tearle W. M., Tweed C. J. (2002): Testing of models of the dissolution of cements – leaching of synthetic CSH gels; Cement and Concrete Research, 32, 731-746.

[81] Sugiyama D. (2008): Chemical alteration of calcium silicate hydrate (C-S-H) in sodium chloride solution; Cement and Concrete Research, 38, 1270-1275.

## 8. Table of figures

Figure 1: Mineral phases in the ternary system CaO, $H_2O$ and $SiO_2$ modified after [39]. The yellow area marks the predominance field of C-S-H structures. ......................................................... 5

Figure 2: Structural model of C-A-S-H gels adapted from [26] and [43]. A = interlayer; B = 'dreierketten' chain; C = CaO sheet; $Q^1$ = silicon tetrahedron sharing one oxygen atom; $Q^2$ = silicon tetrahedron sharing two oxygen atoms; $Q^3$ = silicon tetrahedron sharing three oxygen atoms; b = bridging; p = pairing; (1Al) = silicon in tetrahedral coordination neighboring an aluminium occupied tetrahedron; blue circles = possible isomorphic substitution of $Ca^{2+}$ ions by heavy metals (Me); grey circles = $Ca^{2+}$ in CaO layer; blanc circles = molecular / interlayer water. ......................................................... 6

Figure 3: Predominance fields of C-S-H phases with varying Ca/Si (C/S) molar ratio and temperature (adapted from [39]). Pt = Portlandite; RH = Reinhardbrausite; H = $H_2O$; X = Xenolite. .......... 7

Figure 4: Schematic overview showing the experimental setup and multi-methodological approach used in this study for the precipitation and characterization of Me-bearing C-A-S-H gel phases and aqueous solutions. 1; Preparation of $Si(OH)_4$ stock solution; 2: Addition of Ca-, Al- and Me-salts as powders; 3: Hydrochemical monitoring and fluid sampling; 4: Sample filtration and preparation for solid-phase characterization methods. ......................................................... 10

Figure 5: Temporal evolution of the elemental concentrations and reactive fluid pH for the reference experiment (Ref, upper left) and experiments run at Me/Si molar ratios of 0.05 (left panel) and 0.5 (right panel), respectively. ......................................................... 16

Figure 6: C-A-S-H gels stored in a desiccator (plan view) for drying. Note the significant variation in color of the precipitates as a function of the type of Me used. Azure blue = Cu-series; white = Zn-series and reference material; purple-blue and lilac = Co-series. The stronger the color`s intensity, the higher the amount of Me introduced in the system. ......................................................... 19

Figure 7: XRD patterns of the reference material (Ref) and Me-bearing precipitates obtained after drying for about one month in the desiccator. Atc – Atacamite, Paratc – Paratacamite, Cc – Calcite, MHC – Monohydrocalcite, CASH – Calcium aluminium silicate hydrate. ............... 21

Figure 8: FTIR spectra of the reference material (Ref) and Me-bearing precipitates obtained after drying for about one month in the desiccator. See text for explanations. ............................... 24

Figure 9: Thermogravimetric (TG) curves of selected samples. ......................................................... 25

Figure 10: BSE images of a-b) Co-bearing C-A-S-H, c-d) Cu-bearing C-A-S-H, e-f) Zn-bearing C-A-S-H materials and g) the reference material without Me. h = EDS spectra of the respective materials. Yellow circles= Agglomerated, flocculent particles, typical for C-A-S-H gels precipitated at room temperature [68]. ......................................................... 28

Figure 11: TEM images of the reference material. ......................................................... 29

Figure 12: TEM images of a-c = Co-series (c=HAADF image of Co0.5), d-f = Cu-series (f = HAADF image of Cu0.5). Inserted FFT pattern correspond to C-A-S-H in e. TEM images g-i = Zn-series. ......................................................... 30

Figure 13: Evolution of the saturation index vs. time for the reference experiment. Presented are the SI values of jennite-type C-S-H (blue) and tobermorite-type C-S-H (orange), which are the two endmembers for C-S-H phases with Ca/Si ratios from 0.83 to 1.63. The change of the Ca/Si molar ratio of the reactive fluid over time is presented in grey. ............................................ 32

Figure 14: Substitution of Ca by Me in synthetic Me-C-A-S-H phases. ............................................. 36

Figure 15: TEM-EELS based element distribution mappings of Cu, Ca and O for sample Cu0.5. ...... 38

Figure 16: Calculated solubility products ($K_{SP}$) for Me-C-A-S-H compared to reported C-(A)-S-H data from the literature [37][75]. ......................................................... 41

Figure AP 1: Temporal evolution of the elemental concentrations and reactive fluid pH for the reference experiment (Ref, upper left) and experiments run at Me/Si molar ratios of 0.05 to 0.6 for the Co-series. 55

Figure AP 2: Temporal evolution of the elemental concentrations and reactive fluid pH for the reference experiment (Ref, upper left) and experiments run at Me/Si molar ratios of 0.05 to 0.6 for the Cu-series. 56

Figure AP 3: Temporal evolution of the elemental concentrations and reactive fluid pH for the reference experiment (Ref, upper left) and experiments run at Me/Si molar ratios of 0.05 to 0.6 for the Zn-series. 57

Figure AP 4: Results XRD for the Co-series (multi-coloured) compared to the reference material (grey). 58

Figure AP 5: Results XRD for the Cu-series (multi-coloured) compared to the reference material (grey). 59

Figure AP 6: Results XRD for the Zn-series (multi-coloured) compared to the reference material (grey). 60

Figure AP 7: Co-series: FTIR 1. 61

Figure AP 8: Cu-series: FTIR 1. 62

Figure AP 9: Zn-series: FTIR 1. 62

Figure AP 10: TG (blue line), DSC (red line) and rate of weight loss (green) of sample Ref_filtr. 63

Figure AP 11: TG (blue line), DSC (red line) and rate of weight loss (green) of sample Zn0.4. 63

Figure AP 12: TG (blue line), DSC (red line) and rate of weight loss (green) of sample Zn0.1. 64

Figure AP 13: TG (blue line), DSC (red line) and rate of weight loss (green) of sample Co0.4. 64

Figure AP 14: TG (blue line), DSC (red line) and rate of weight loss (green) of sample cu0.4. 65

Figure AP 15: TG (blue line), DSC (red line) and rate of weight loss (green) of sample Zn0.4. 65

Figure AP 16: The reference material under ESEM with snowflake-shaped calcite crystals attached on its surface. 66

Figure AP 17: TEM images of a-c = Co0.1, d-f = Co 0.3 (e = HAADF image) and g-i = Co 0.5 (h = HAADF image). j = EDS spectra of Co0.1, Co0.3 and Co0.5 compared to the reference. 67

Figure AP 18: TEM images of a-c = Cu0.1, d-f = Cu0.3 and g-i = Cu 0.5. Inserted FFT pattern correspond to C-A-S-H. h = HAADF image of Cu 0.5. 68

Figure AP 19: TEM images of a-c = Zn0.1, d,f = Zn0.3 (e = HAADF image) and g-i = Zn0.5. j = EDS spectra of Cu0.1, Cu0.3 and Cu0.5 compared to the reference. 69

## 9. List of tables

Table 1: Compilation of experimental solution data obtained after 60 min. Note the high removal efficiencies for aqueous Al, Si and Me. .................... 17

Table 2: Summary of calculated weight losses and related temperature ranges for selected samples, as obtained from TG curves. Note that the DSC signal was negative in the reported temperature intervals, reflecting endothermic reactions. Blue = partly wt. loss due to monohydrocalcite (MHC). Orange= wt. loss due to $CaCO_3$ or MHC decomposition. .................... 26

Table 3: Summary of calculated weight losses of the selected samples after drying and related temperature ranges for selected samples, as obtained from TG curves. Orange= wt. loss due to $CaCO_3$ decomposition. .................... 27

Table 4: Calculated molar compositions of (Me)-C-A-S-H precipitates. .................... 27

Table 5: Summary of (Me)-C-A-S-H gel compositions. Me is assumed to substitute for the Ca position in the C-A-S-H structure. Co-precipitates/secondary phases formed are indicated on the right. Red lines denote the upper threshold values for Me incorporation in C-A-S-H structures. Cc=calcite; MHC=monohydrocalcite; Atc=atacamite. .................... 33

Table AP 1: Water loss of samples, as obtained after 34 days (15.03 – 18.04. 2019) of drying in the desiccator at room temperature. .................... 58

Table AP 2: Comparison of data from this study and the literature. .................... 70

Table AP 3: Results from TGA. .................... 70

Table AP 4: Molar weight of respective oxides in g/mol. .................... 70

Table AP 5: Molar portions of the respective oxides in (Me)-C-A-S-H calculated from mass balance. .................... 70

Table AP 6: Calculated weight portions considering a dry mass ($md$) of 100 g. .................... 72

Table AP 7: Calculated molar portions of the respective oxide in the (Me)CASH materials. .................... 72

Table AP 8: Overview of Me-C-A-S-H solubility constants for gels with Me/Si molar ratios from zero to 0.4 Co and Cu as well as 0.6 for Zn. .................... 73

# 10. Appendix

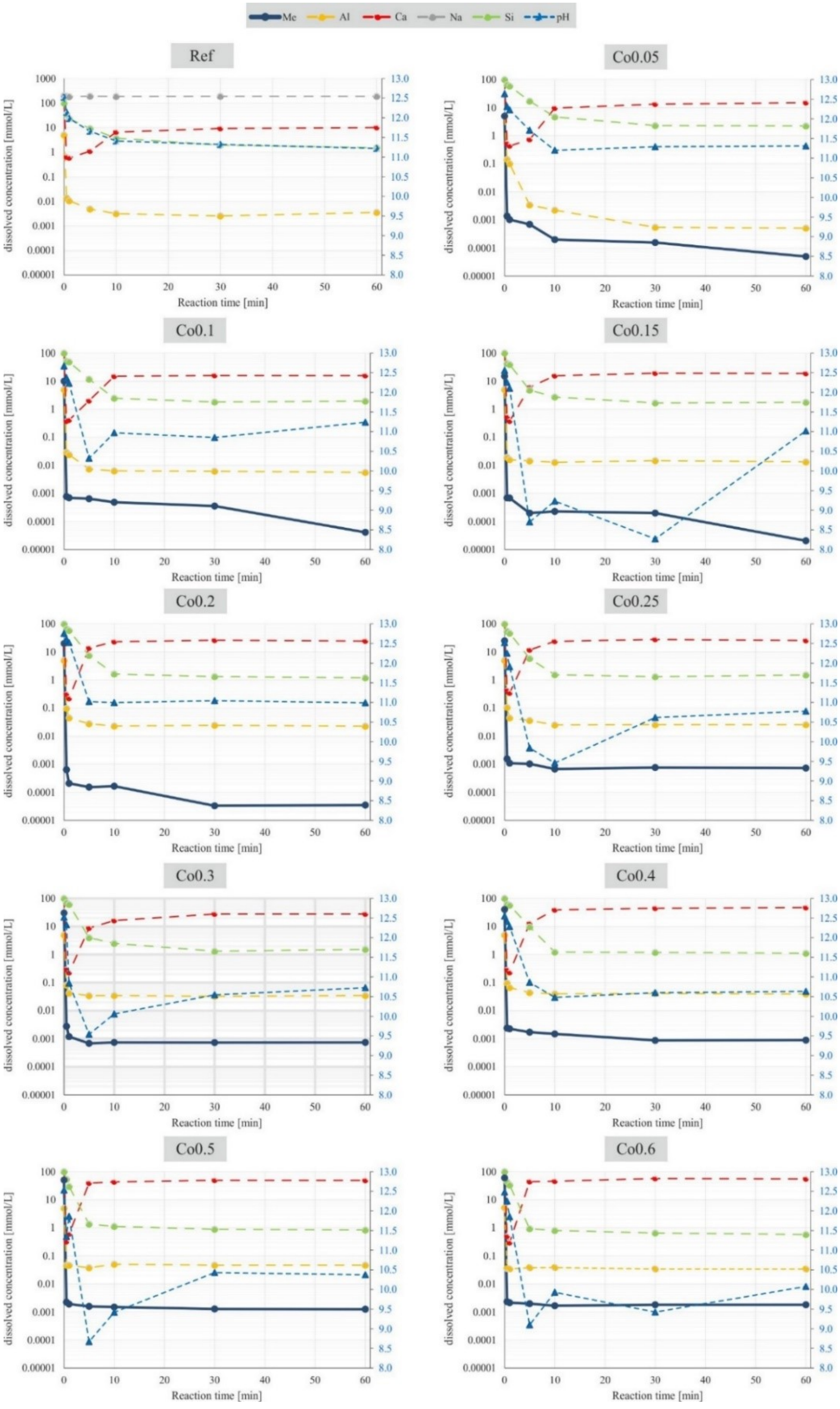

Figure AP 1: Temporal evolution of the elemental concentrations and reactive fluid pH for the reference experiment (Ref, upper left) and experiments run at Me/Si molar ratios of 0.05 to 0.6 for the Co-series.

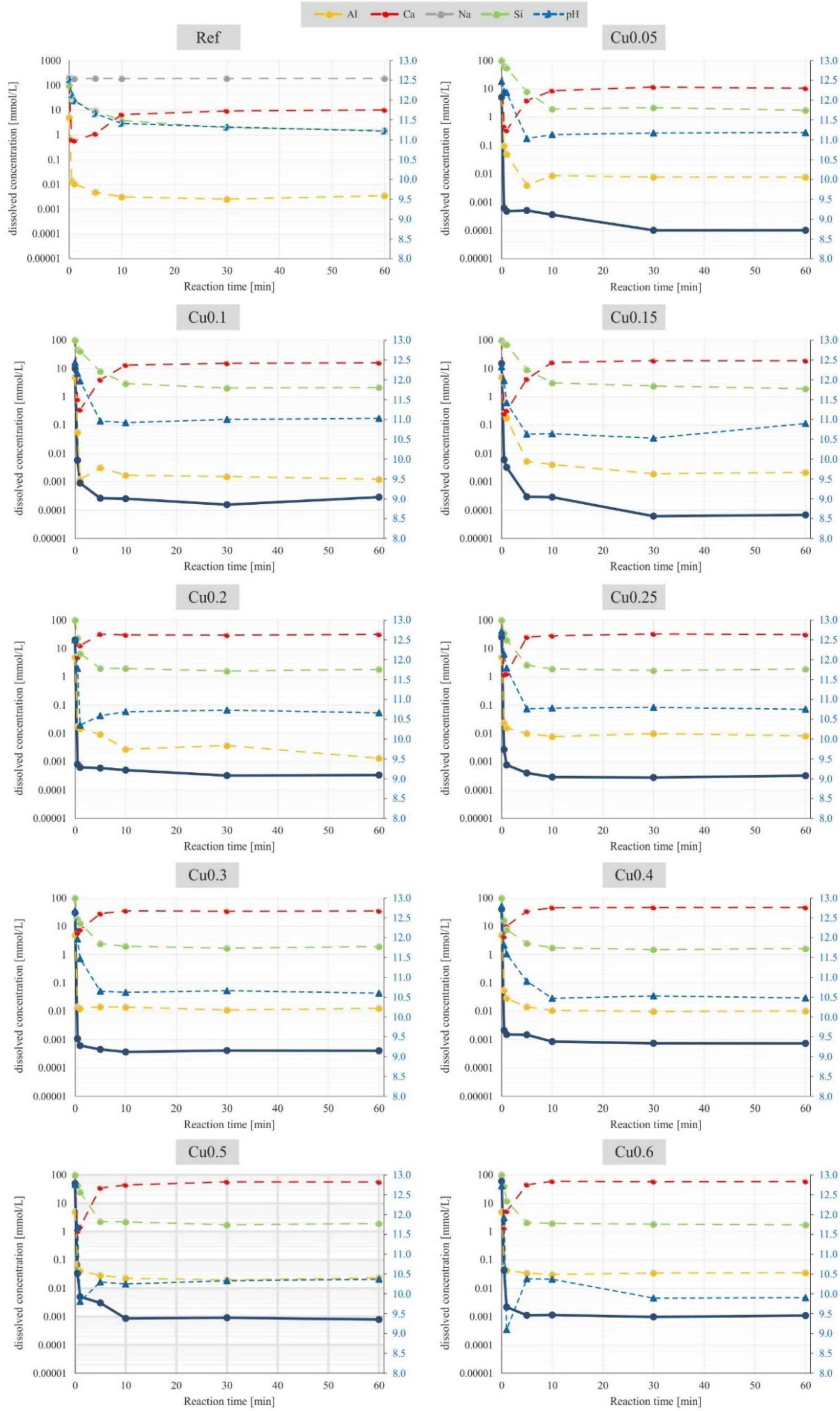

Figure AP 2: Temporal evolution of the elemental concentrations and reactive fluid pH for the reference experiment (Ref, upper left) and experiments run at Me/Si molar ratios of 0.05 to 0.6 for the Cu-series.

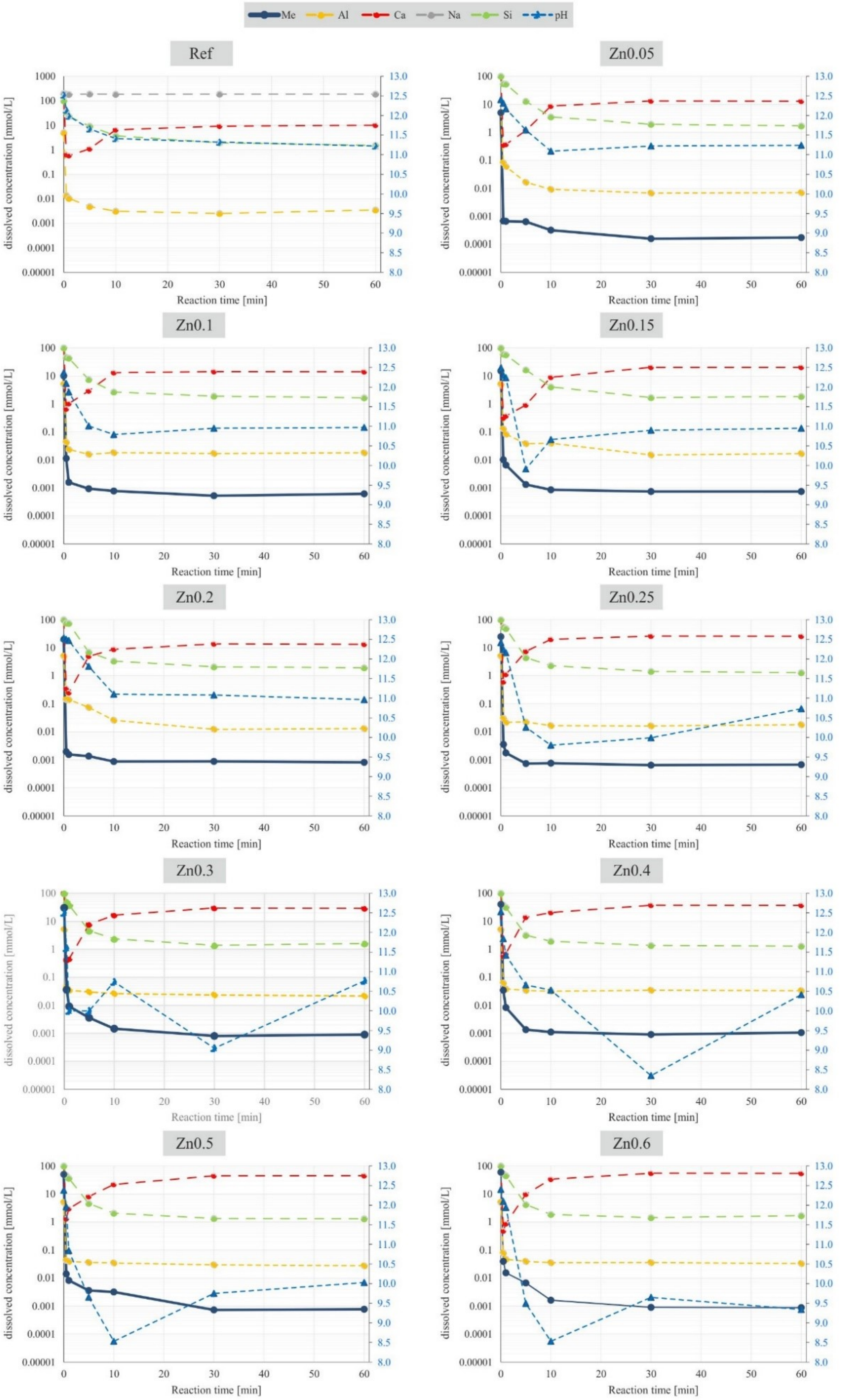

Figure AP 3: Temporal evolution of the elemental concentrations and reactive fluid pH for the reference experiment (Ref, upper left) and experiments run at Me/Si molar ratios of 0.05 to 0.6 for the Zn-series.

Table AP 1: Water loss of samples, as obtained after 34 days (15.03 – 18.04. 2019) of drying in the desiccator at room temperature.

| Me/Si (molar ratio) | 0 | 0.05 | 0.1 | 0.15 | 0.2 | 0.25 | 0.3 | 0.4 | 0.5 | 0.6 |
|---|---|---|---|---|---|---|---|---|---|---|
| | wt% | wt% | wt% | wt% | wt% | wt% | wt% | wt% | wt% | wt% |
| Ref | 2 | - | - | - | - | - | - | - | - | - |
| Co | - | 9 | 4 | 5 | 11 | 8 | 8 | 11 | 11 | 10 |
| Cu | - | 9 | 8 | 8 | 3 | 7 | 11 | 14 | 21 | 19 |
| Zn | - | 9 | 4 | 9 | 5 | 10 | 11 | 12 | 16 | 19 |

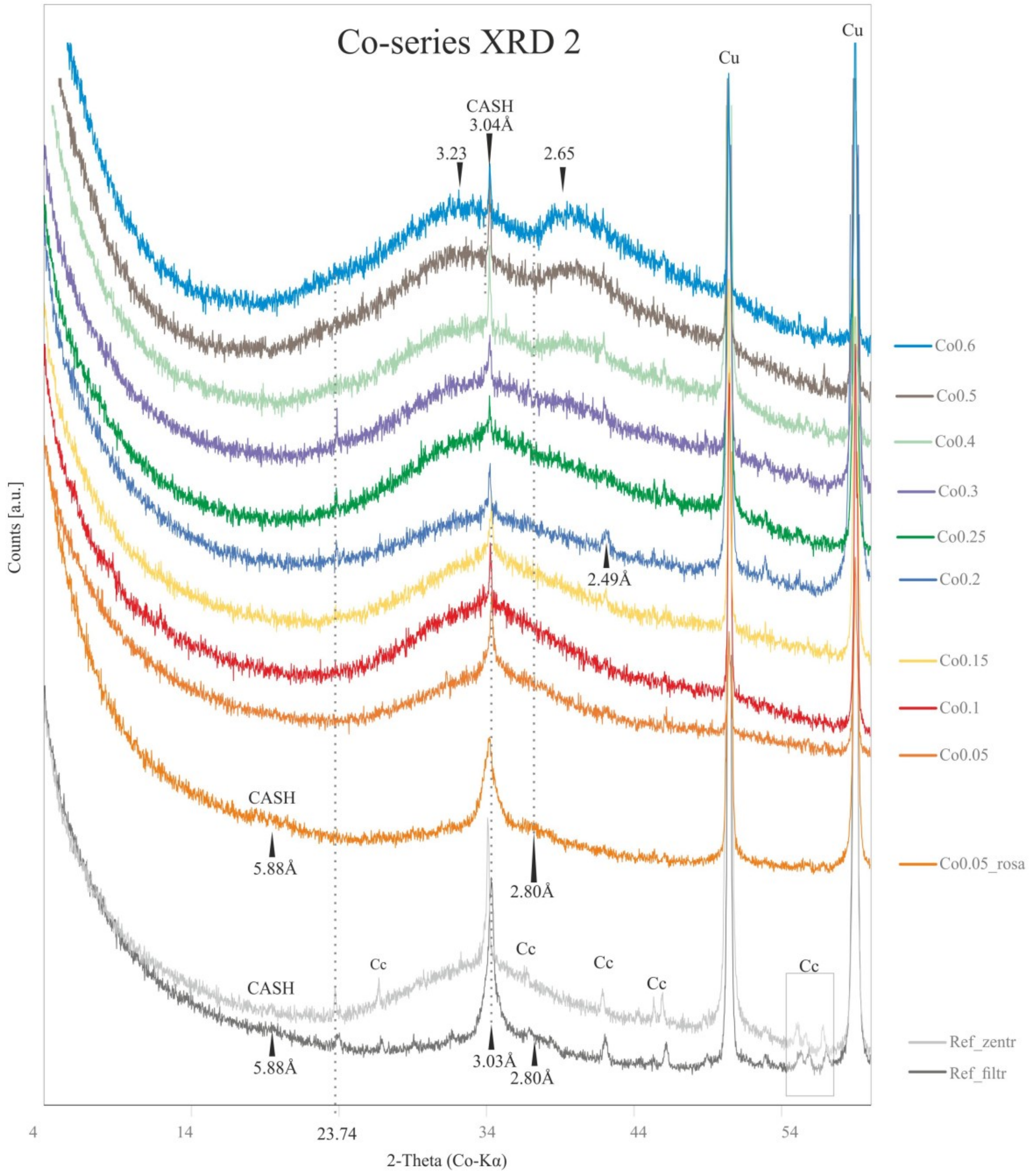

Figure AP 4: Results XRD for the Co-series (multi-coloured) compared to the reference material (grey).

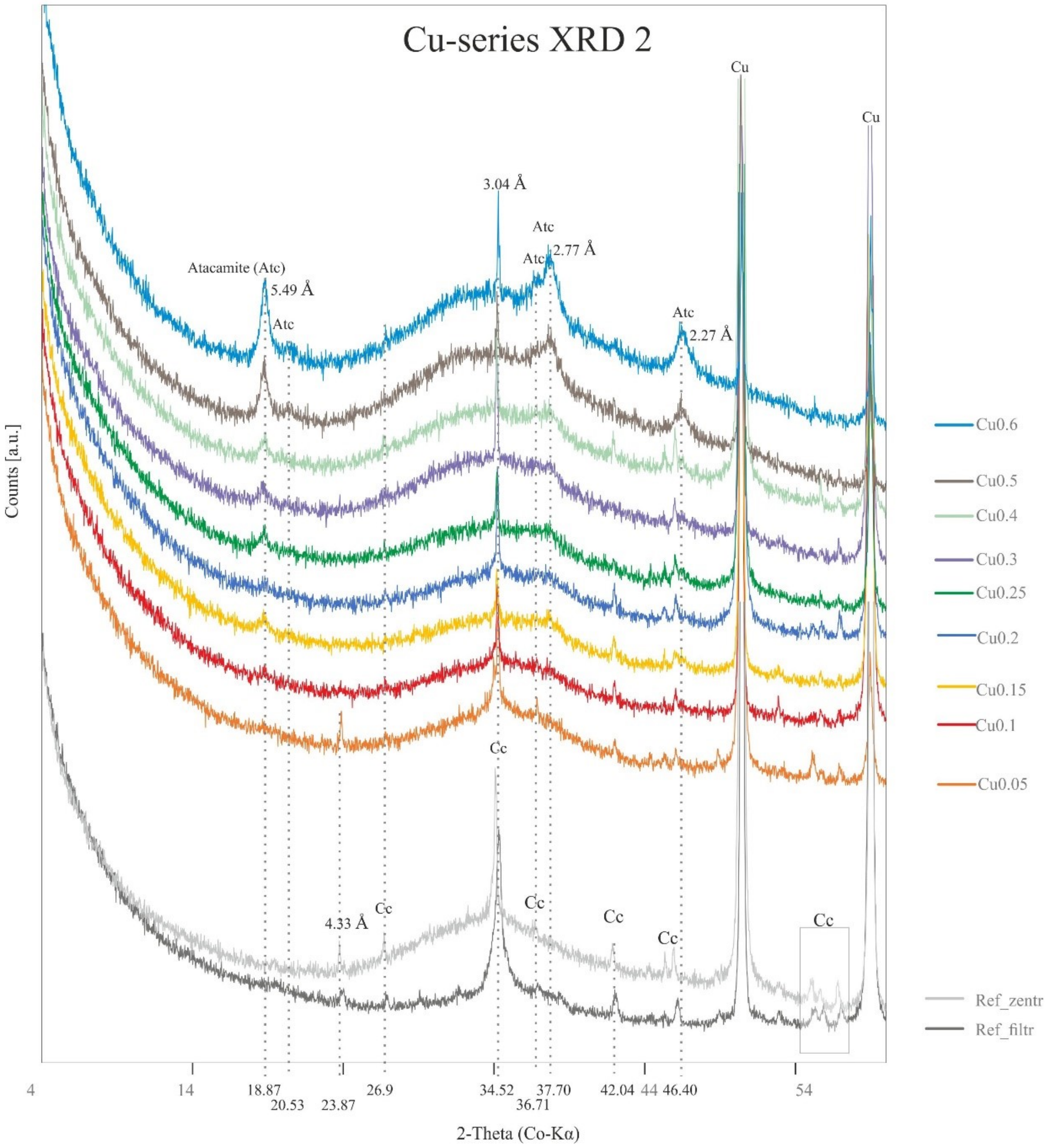

Figure AP 5: Results XRD for the Cu-series (multi-coloured) compared to the reference material (grey).

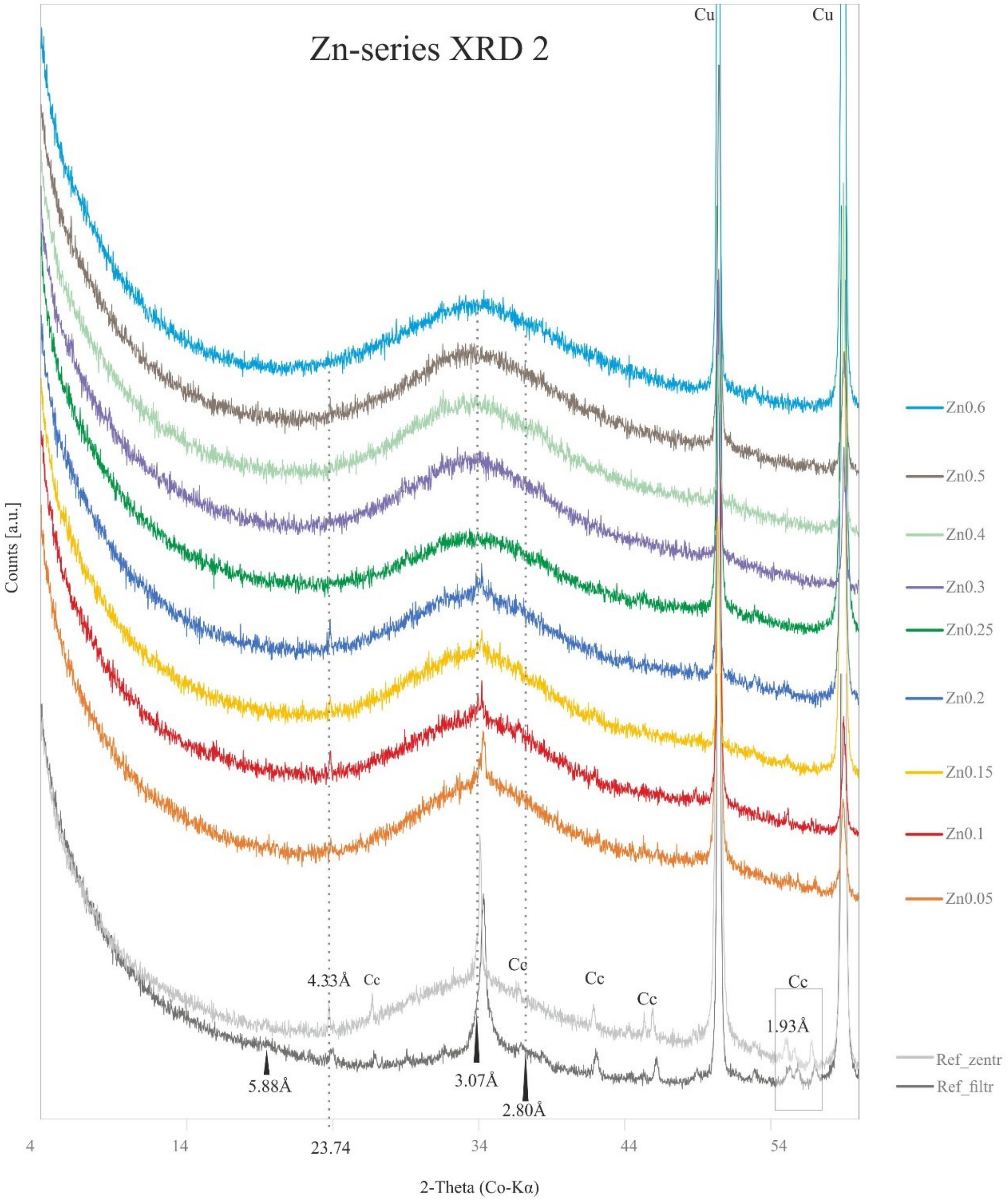

Figure AP 6: Results XRD for the Zn-series (multi-coloured) compared to the reference material (grey).

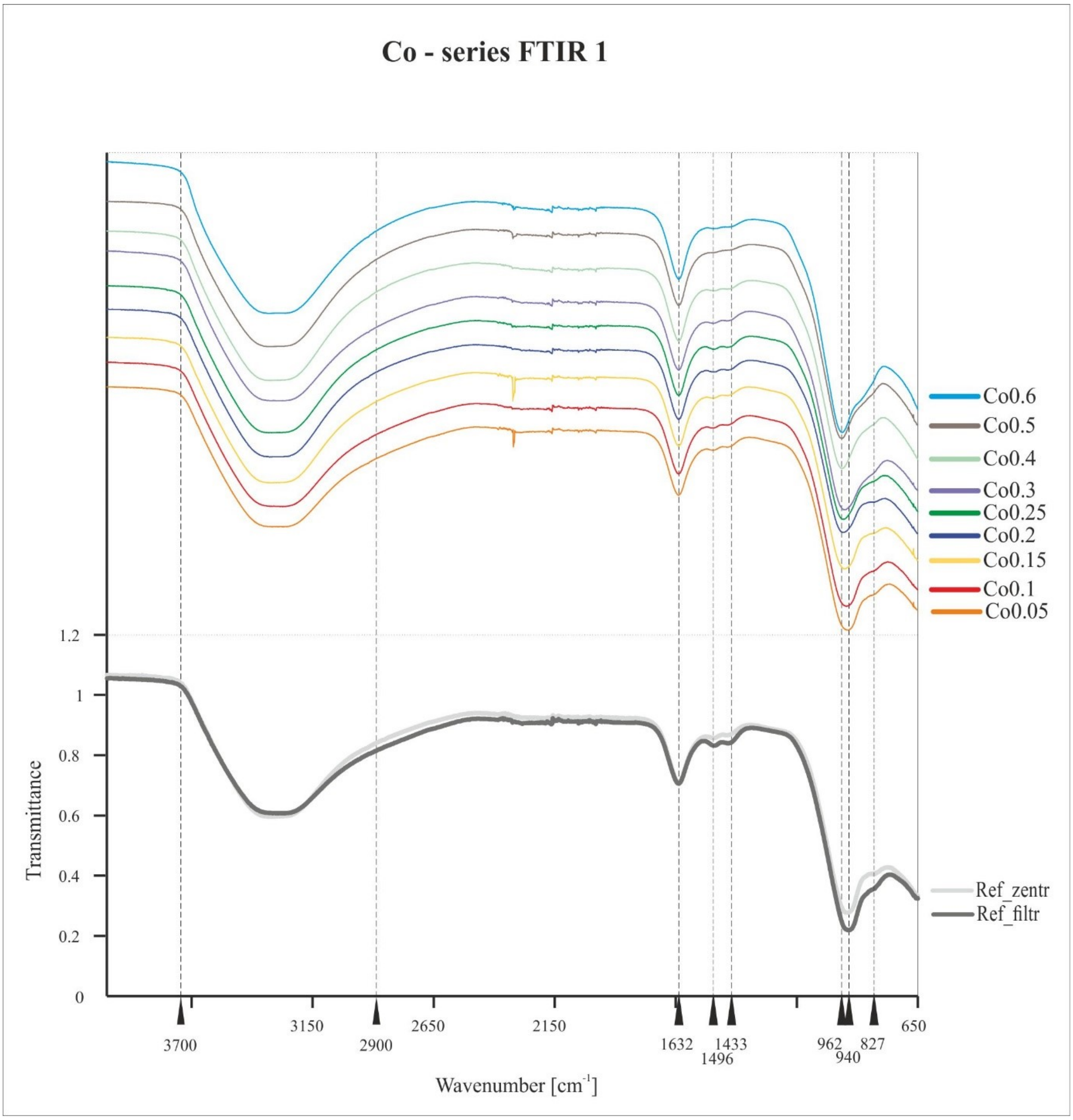

Figure AP 7: Co-series: FTIR 1.

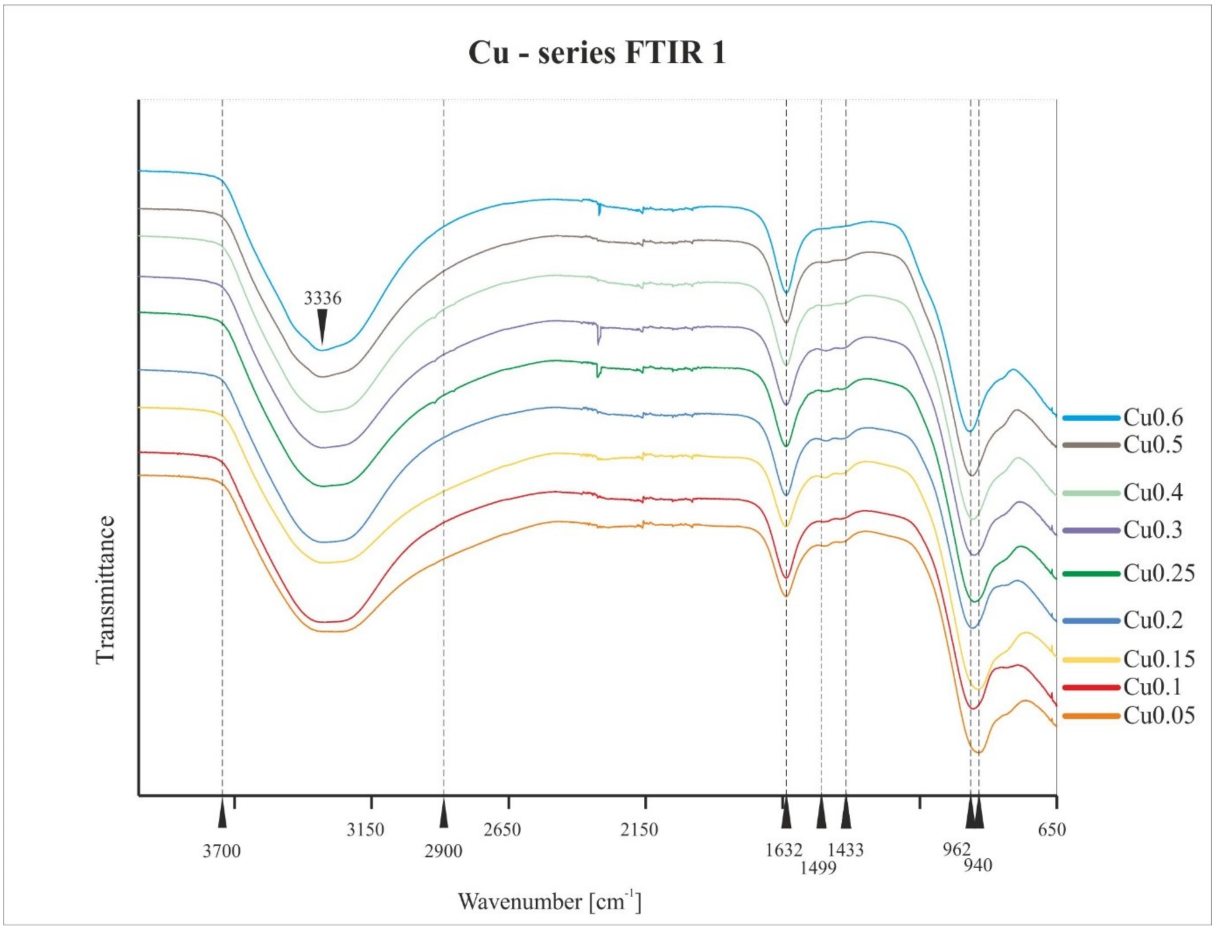

Figure AP 8: Cu-series: FTIR 1.

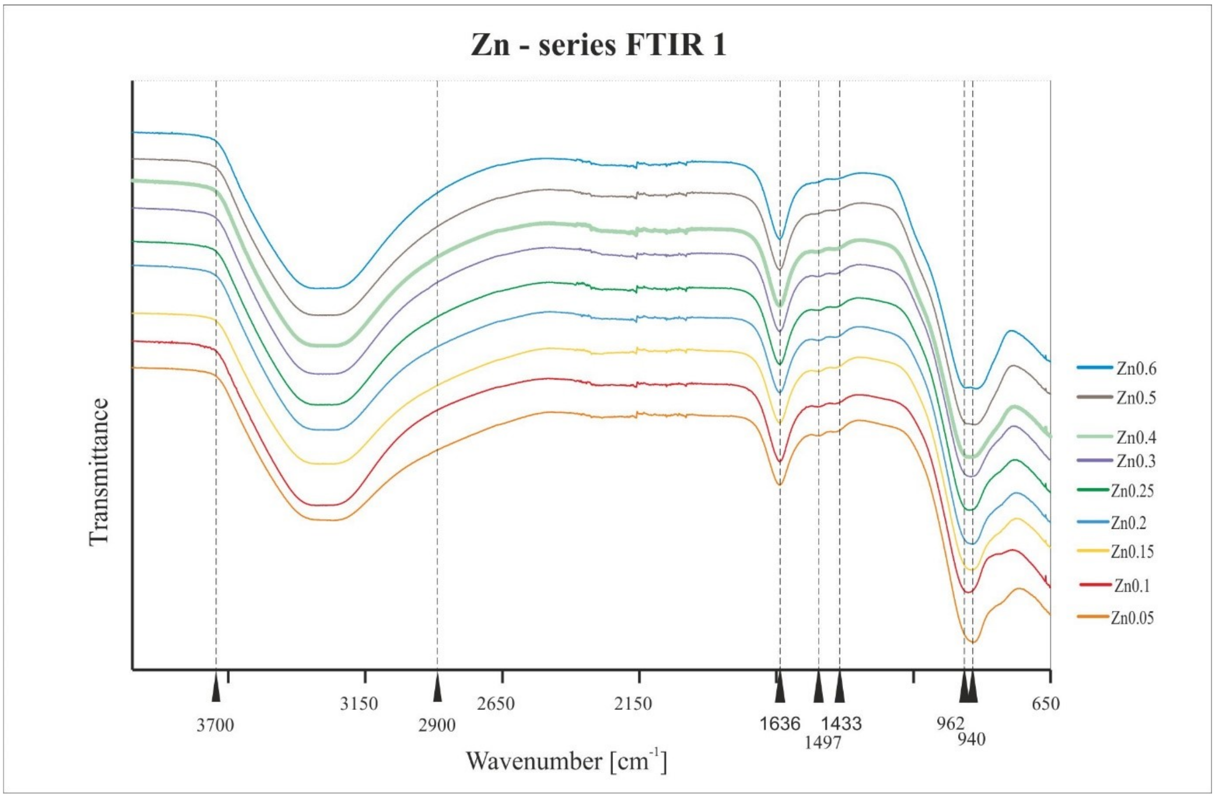

Figure AP 9: Zn-series: FTIR 1.

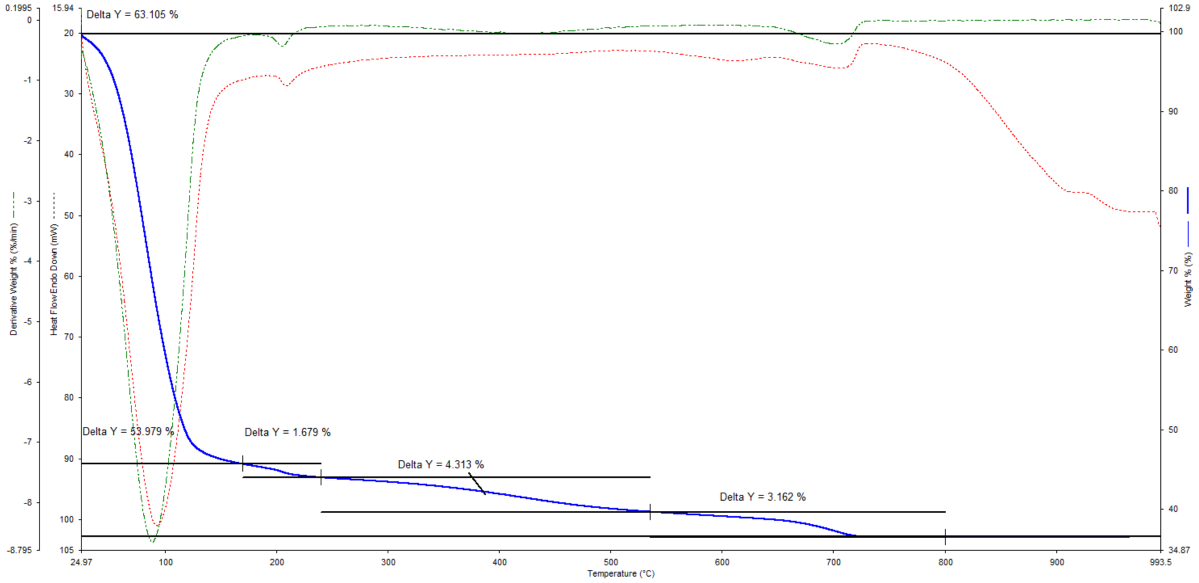

Figure AP 10: TG (blue line), DSC (red line) and rate of weight loss (green) of sample Ref_filtr.

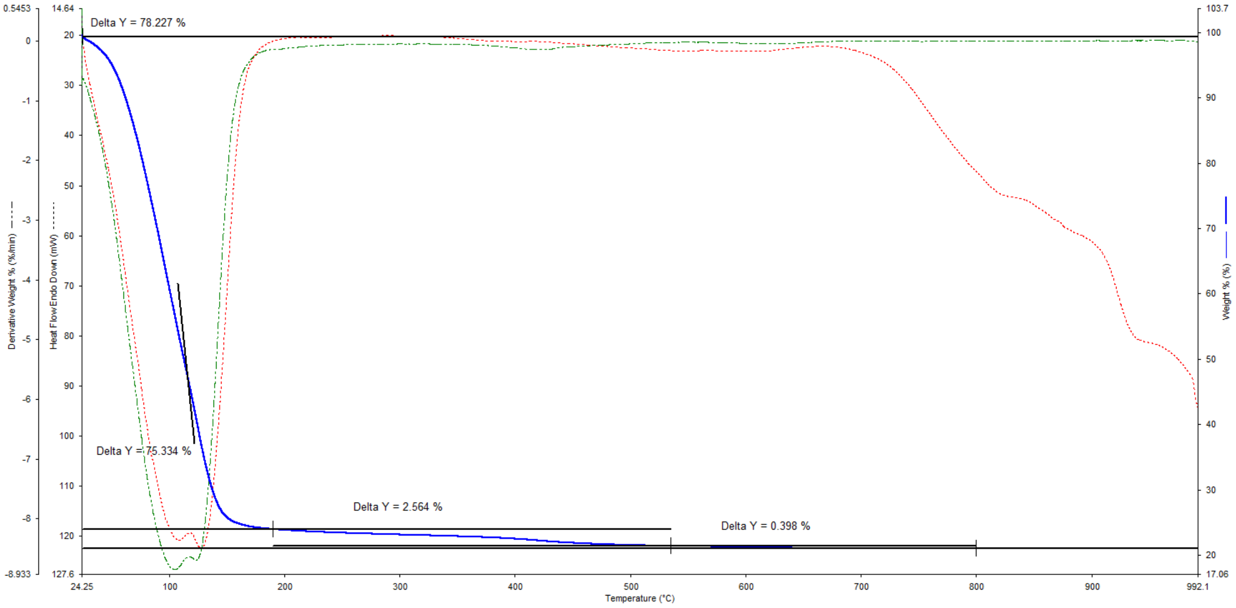

Figure AP 11: TG (blue line), DSC (red line) and rate of weight loss (green) of sample Zn0.4.

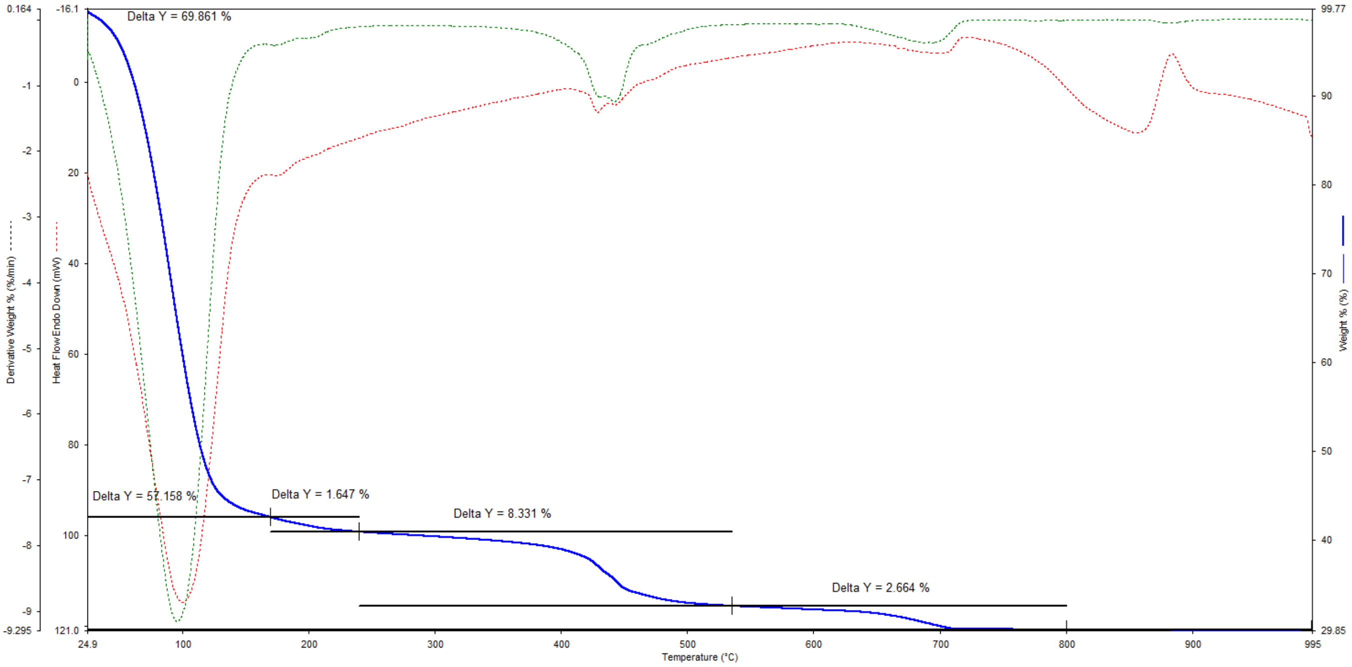

Figure AP 12: TG (blue line), DSC (red line) and rate of weight loss (green) of sample Zn0.1.

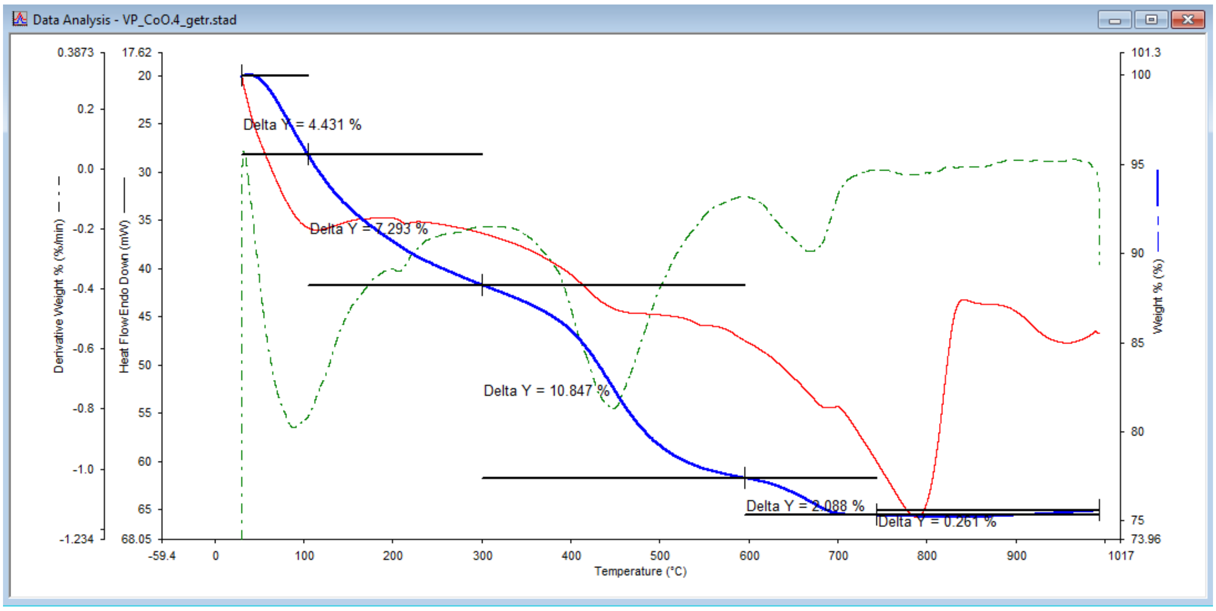

Figure AP 13: TG (blue line), DSC (red line) and rate of weight loss (green) of sample Co0.4.

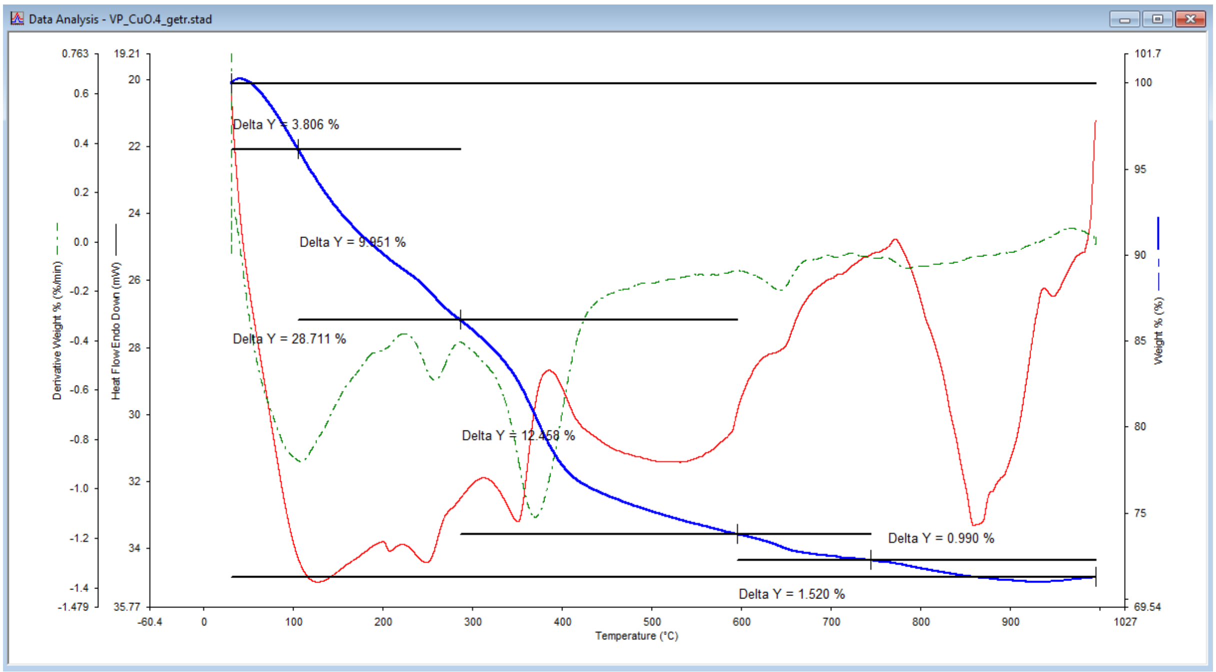

Figure AP 14: TG (blue line), DSC (red line) and rate of weight loss (green) of sample cu0.4.

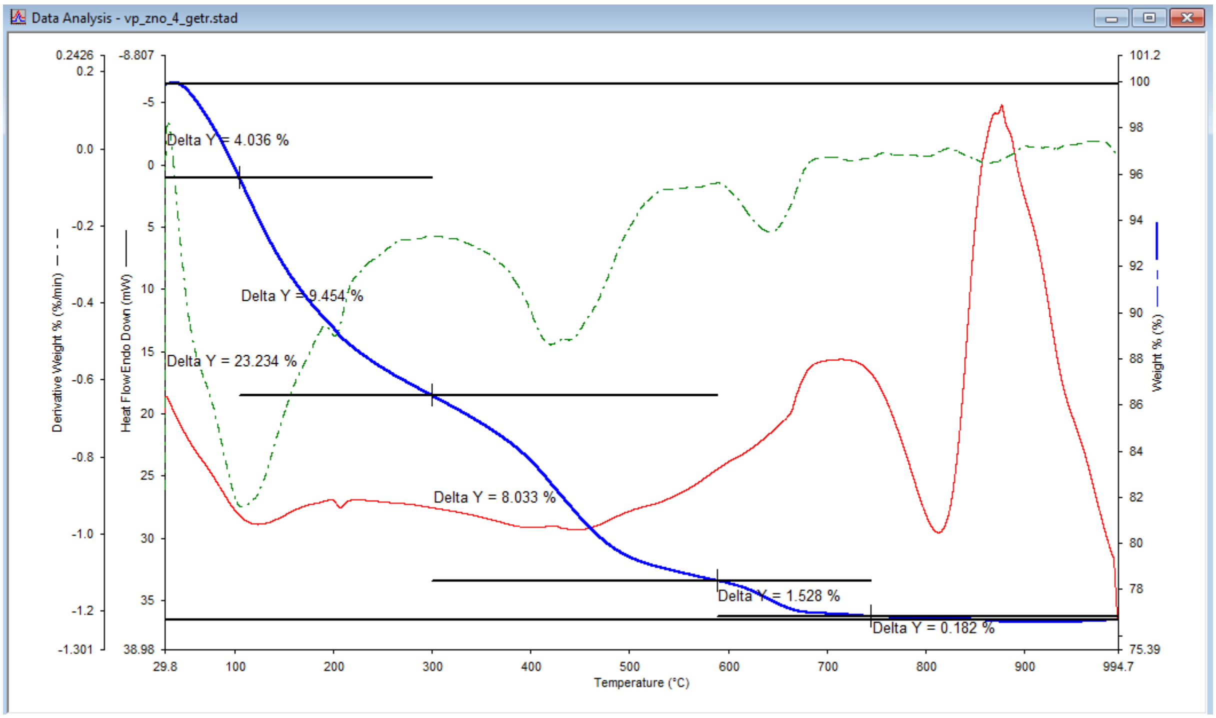

Figure AP 15: TG (blue line), DSC (red line) and rate of weight loss (green) of sample Zn0.4.

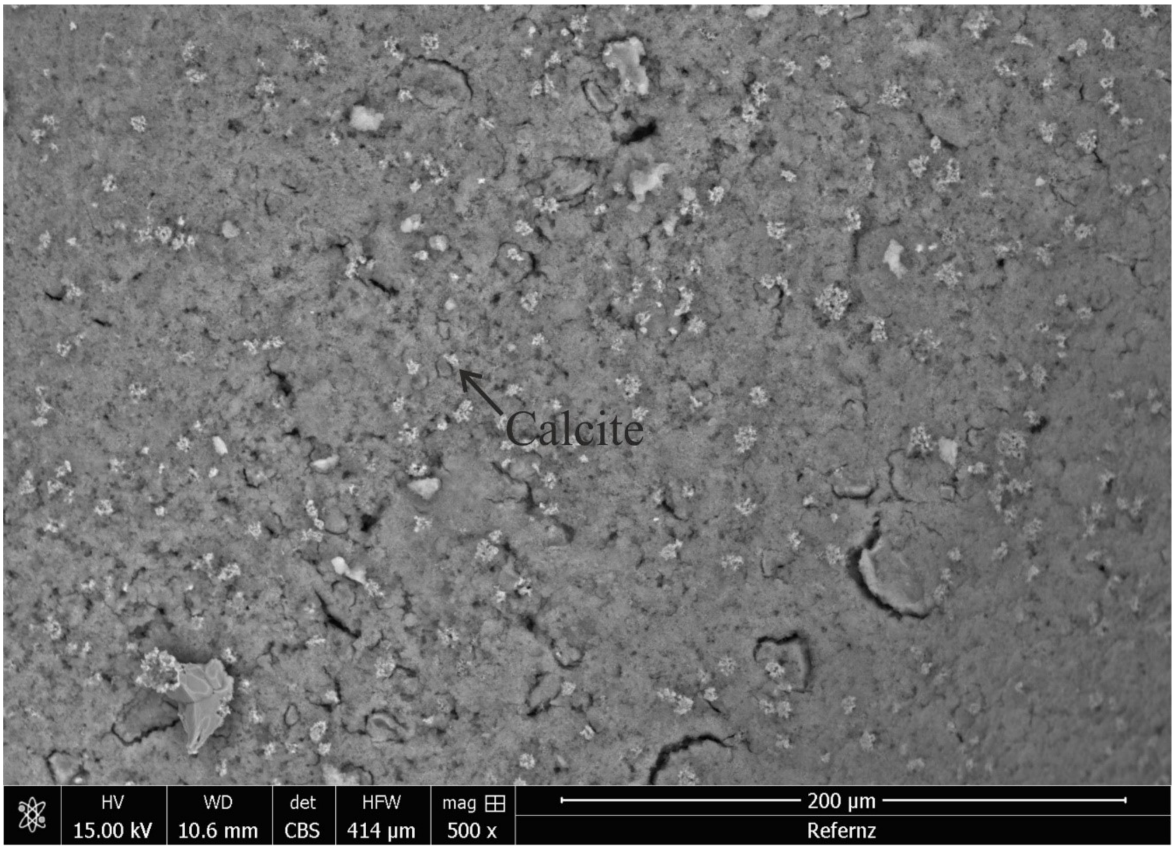

Figure AP 16: The reference material under ESEM with snowflake-shaped calcite crystals attached on its surface.

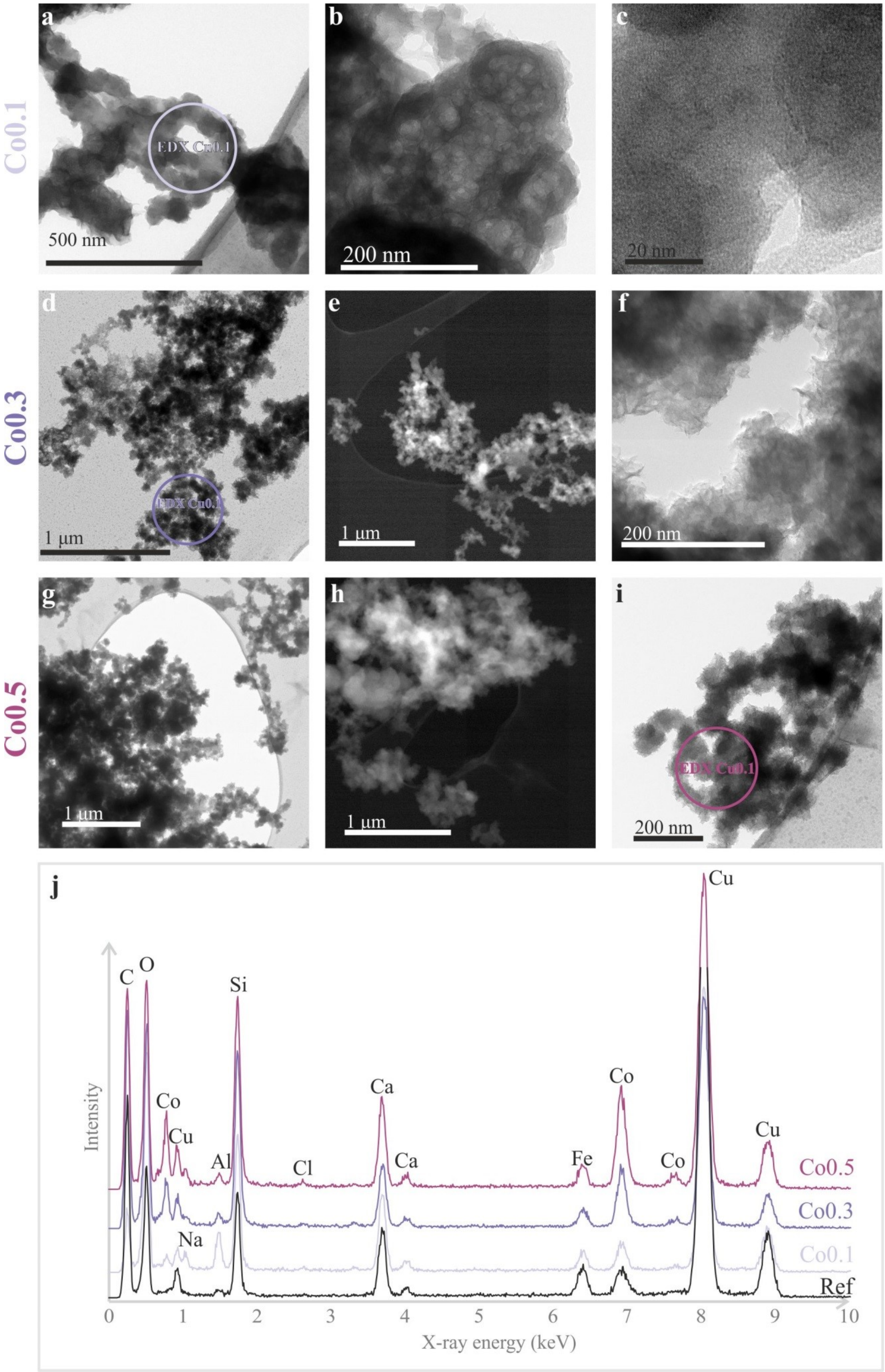

Figure AP 17: TEM images of a-c = Co0.1, d-f = Co 0.3 (e = HAADF image) and g-i = Co 0.5 (h = HAADF image). j = EDS spectra of Co0.1, Co0.3 and Co0.5 compared to the reference.

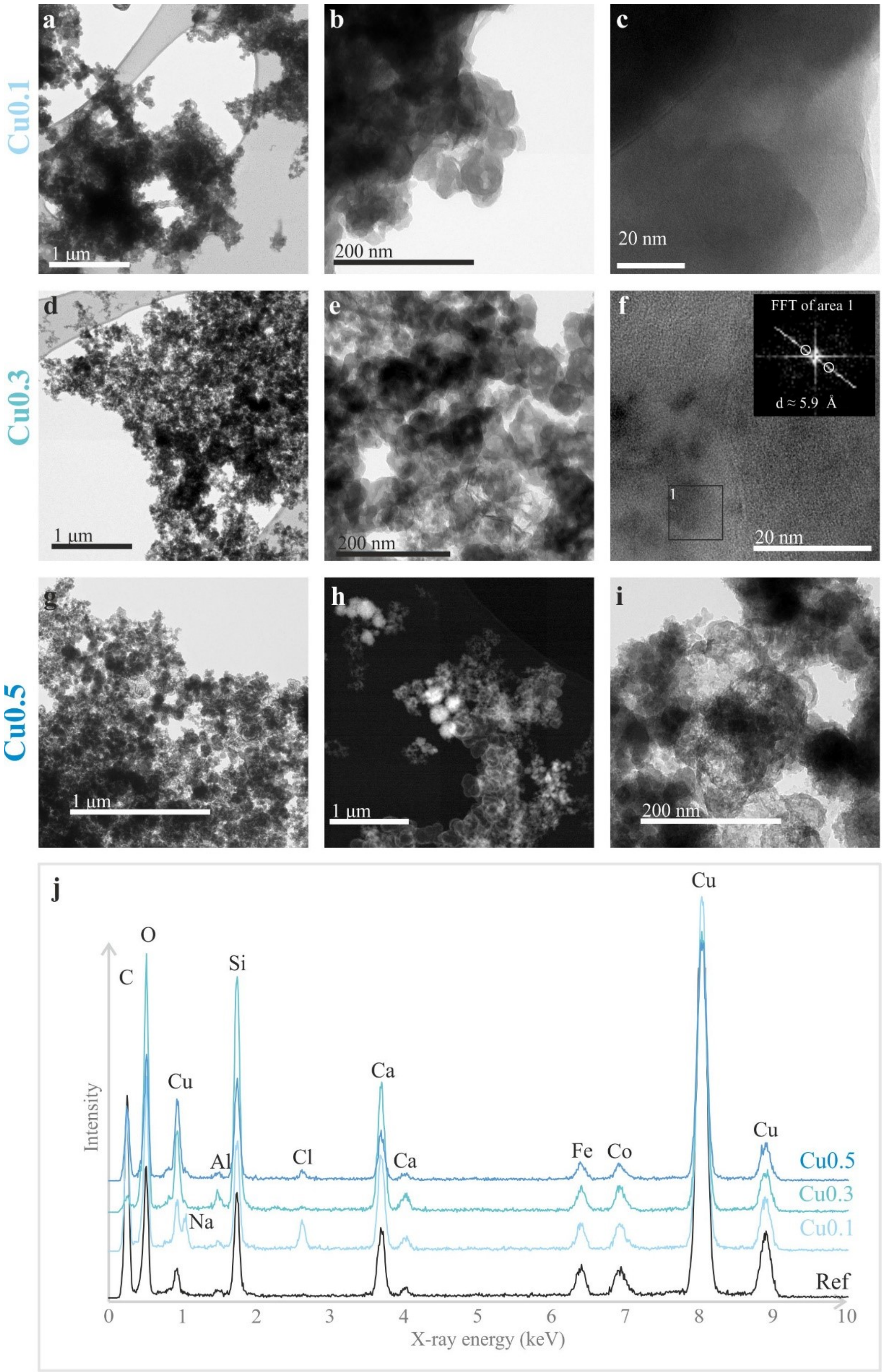

Figure AP 18: TEM images of a-c = Cu0.1, d-f = Cu0.3 and g-i = Cu 0.5. Inserted FFT pattern correspond to C-A-S-H. h = HAADF image of Cu 0.5.

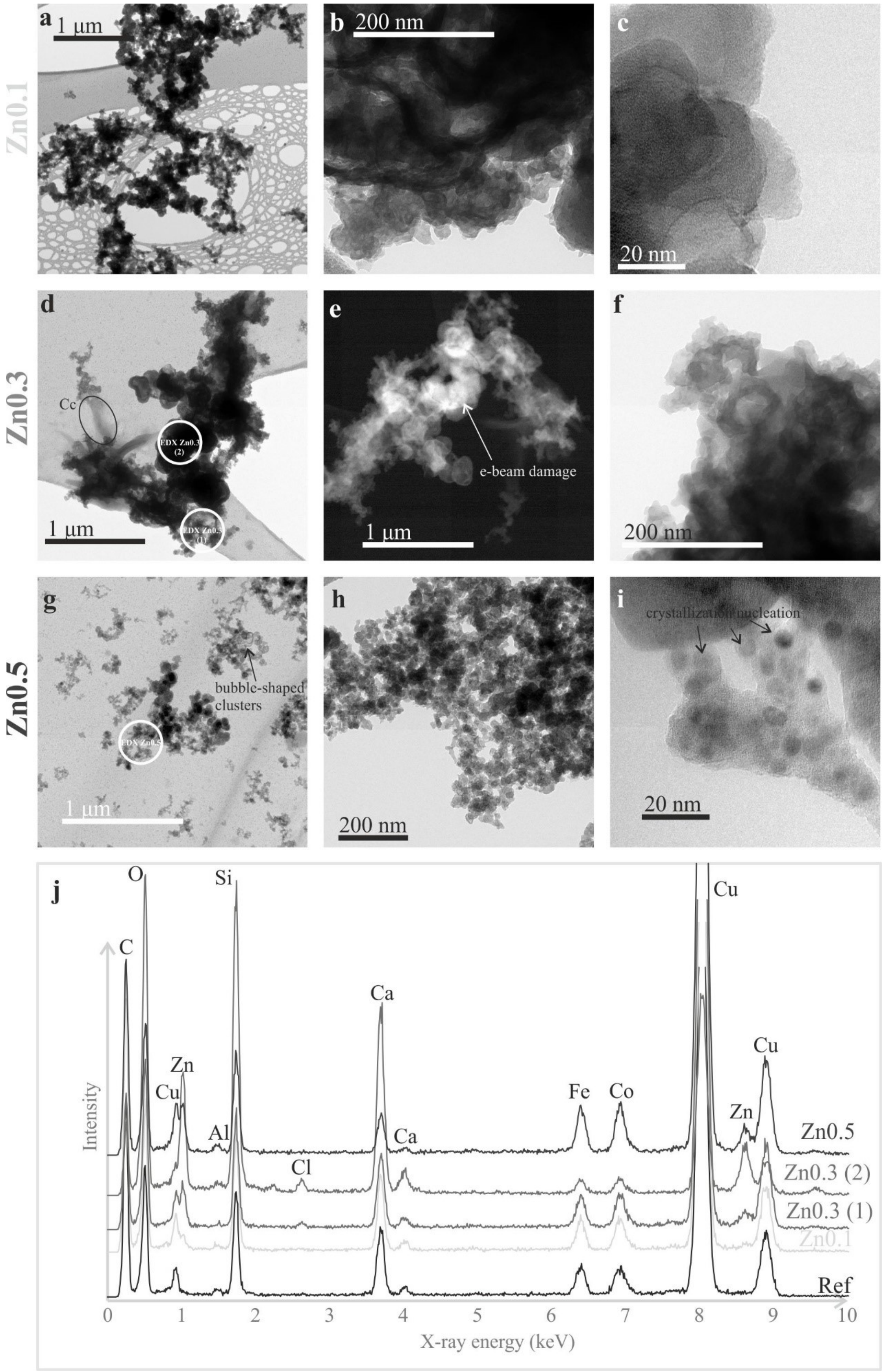

Figure AP 19: TEM images of a-c = Zn0.1, d,f = Zn0.3 (e = HAADF image) and g-i = Zn0.5. j = EDS spectra of Cu0.1, Cu0.3 and Cu0.5 compared to the reference.

Table AP 2: Comparison of data from this study and the literature.

| Target Ca/Si | Target Al/Si | Calculated Ca/Si ratio in C-(A)-S-H | pH | Ca (mM/L) in sol. | Si (mM/L) in sol. | Ca/Si in sol. | Ref. |
|---|---|---|---|---|---|---|---|
| | | 0.88 | 11.77 | 1.80 | 0.17 | 10.59 | [80] |
| | | 0.88 | 11.64 | 1.80 | 0.20 | 9.00 | [80] |
| | | 0.88 | 10.59 | 0.66 | 0.95 | 0.69 | [80] |
| | | 0.88 | 10.65 | 0.63 | 0.91 | 0.69 | [80] |
| | | 0.88 | 11.3 | 1.4 | 0.3 | 4.7 | [81] |
| 1 | 0.05 | 0.88 (Ca/Si+Al) | 11.2 | 9.63 | 1.72 | 5.60 | this study |
| 1 | 0.05 | 0.95 (Ca/Si+Al) | 11.3 | 10.6 | 1.4 | 7.57 | [26] |
| 1 | 0.05 | 0.94 (Ca/Si+Al) | 11.8 | 2.1 | 0.15 | 14.00 | [46] |

Table AP 3: Results from TGA.

| Sample | total wt. loss [wt%] | wt. loss from 25°C to 170°C [wt%] | wt. loss from 170°C to 240°C [wt%] | wt. loss from 240°C to 535°C [wt%] | wt. loss from 535°C to 800°C [wt%] | wt. loss from 105°C to 800°C [wt%] |
|---|---|---|---|---|---|---|
| Ref_filtr | 63.1 | 54.0 | 1.7 | 4.3 | 3.2 | 20.0 |
| Co0.4 | 80.1 | 76.5 | - | 2.9 | 0.5 | 30.9 |
| Cu0.4 | 80.4 | 75.3 | - | 3.8 | 0.7 | 26.3 |
| Zn0.1 | 69.9 | 57.2 | 1.7 | 8.3 | 2.7 | 27.1 |
| Zn0.4 | 78.2 | 75.3 | - | 2.6 | 0.4 | 35.7 |

Table AP 4: Molar weight of respective oxides in g/mol.

| M CaO [g/mol] | M MeO [g/mol] | M $SiO_2$ [g/mol] | M $Al_2O_3$ [g/mol] | M $Ca(CO_3)$ $H_2O$ [g/mol] | M $CaCO_3$ [g/mol] | M $H_2O$ [g/mol] | M $CO_2$ [g/mol] |
|---|---|---|---|---|---|---|---|
| 56 | Zn 81 | 60 | 102 | 119 | 100 | 18 | 44 |
| | Co 75 | | | | | | |
| | Cu 80 | | | | | | |

Table AP 5: Molar portions of the respective oxides in (Me)-C-A-S-H calculated from mass balance.

| Mol CaO | Mol ZnO, CuO, ZnO | Mol $SiO_2$ | Mol $Al_2O_3$ |
|---|---|---|---|
| 0,920 | 0,000 | 1,000 | 0,025 |
| 0,539 | 0,408 | 0,980 | 0,025 |
| 0,539 | 0,408 | 0,980 | 0,025 |
| 0,830 | 0,100 | 1,000 | 0,025 |
| 0,640 | 0,400 | 1,000 | 0,025 |

The weight percentage and molar portion of $H_2O$ in the (Me)CASH materials was calculated as followed, considering Table AP 3 - Table AP 5:

1. Dry mass ($m_d$) is composed of CaO, $SiO_2$, $Al_2O_3$ and MeO.
2. Originating form $m_d = 100\ g$ a theoretical amount of CaO and SiO2 ($m_x$) in *g* was calculated (Table AP 6) according to equation (I) in a further step, whereas $n_x$is the molar proportion of substance *x* in *mol* and $M_x$ is the respective molar mass of *x*, $n_{ox}$ and $M_{ox}$ generally stands for the molar proportion and molar mass of the remaining oxides.

$$m_x = \frac{n_x \cdot M_x \cdot 100}{n_x \cdot M_x + \sum(n_{ox} M_{ox})} \qquad \text{(I)}$$

3. Originating from $m_d = 100\, g$ the theoretical mass (*m*) of the total sample was calculated in *g* according to formula (II), whereas $wt\%_{H_2O}$ is the respective wt. loss from 105°C to 800°C (Table AP 3).

$$m = \frac{m_d}{(100 - wt\%_{H_2O})} \cdot 100 \qquad \text{(II)}$$

4. The theoretical amount of $CO_2$ ($m_{CO_2}$) and $H_2O$ ($m_{H_2O}$) in monohydrocalcite (MHC) in *g* was calculated for the sample Zn0.1, whereas the amount of $CO_2$ was the limiting factor (see equation (III)). $m$ is the mass of the total sample in *g*, $wt\%_{CO_2}$ is the weight loss from 535°C to 1000°C, $n_{CO_2}$ is the theoretical mole portion in *mol* of $CO_2$ and $M_{CO_2}$ is the respective molar weight in *g/mol*, $M_{H_2O}$ is the molar weight in *g/mol* of $H_2O$.

$$m_{CO_2} = \frac{m \cdot wt\%_{CO_2}}{100} \qquad \text{(III)}$$

$$n_{CO_2} = \frac{m_{CO_2}}{M_{CO_2}} \qquad \text{(IV)}$$

$$m_{H_2O\,(MHC)} = n_{CO_2} \cdot M_{H_2O} \qquad \text{(V)}$$

5. The theoretical amount of $CO_2$ in *g* in calcite for the other samples was calculated with formula III.
6. The theoretical amount of $H_2O$ in the (Me)CASH is calculated with equation VI.

$$m_{H_2O\ in\ (Me)CASH} = \frac{m \cdot wt\%_{H_2O}}{100} - m_{CO_2} - m_{H_2O\,(MHC)} \qquad \text{VI}$$

7. The theoretical amount of CASH in *g* has been calculated by VII.

$$CASH = m - m_{CO_2} - m_{H_2O\,(MHC)} \tag{VII}$$

8. The weight percentage of water in the respective CASH in *g* has been calculated by VIII.

$$wt\%_{H_2O\ in\ (Me)CASH} = \frac{m_{H_2O\ in\ (Me)CASH} \cdot 100}{CASH} \tag{VIII}$$

Table AP 6: Calculated weight portions considering a dry mass ($m_d$) of 100 g.

| $m$ [g] | 137.12 | 155.57 | 124.94 | 135.74 | 144.78 |
|---|---|---|---|---|---|
| CASH [g] | 131.98 | 154.95 | 120.99 | 134.76 | 144.00 |
| $m_d = 100\ g$ | Zn0.1 [g] | Zn0.4 [g] | Ref_filtr [g] | Cu0.4 [g] | Co0.4 [g] |
| $m_{\text{CaO}}$ total | 39.70 | 27.40 | 45.20 | 24.87 | 25.25 |
| $m_{\text{SiO}_2}$ total | 51.18 | 45.80 | 52.57 | 49.37 | 50.12 |
| CaO in MHC* | 4.65 | 0.00 | 0.00 | 0.00 | 0.00 |
| CaO in $CaCO_3$ | 0.00 | 0.79 | 5.03 | 1.25 | 1.00 |
| $m_{CO_2}$ in $CaCO_3$ | 0.00 | 0.62 | 3.95 | 0.98 | 0.78 |
| $m_{H_2O\,(MHC)}$ | 1.49 | 0.00 | 0.00 | 0.00 | 0.00 |
| $m_{CO_2}$ in MHC | 3.65 | 0.00 | 0.00 | 0.00 | 0.00 |
| $m_{H_2O\ in\ (Me)CASH}$ | 31.98 | 54.95 | 20.99 | 34.76 | 44.00 |

9. Finally, the molar portions of structurally bond water ($n_{H_2O\ in\ (Me)CASH}$) (see Table AP 7) were calculated by IX.

$$n_{H_2O\ in\ (Me)CASH} = \frac{n_{CaO} \cdot M_{CaO} \cdot m_{H_2O}}{m_{CaO} \cdot M_{H_2O}} \tag{IX}$$

Table AP 7: Calculated molar portions of the respective oxide in the (Me)CASH materials.

| | $n_{CaO}$ [mol] | $n_{MeO}$[mol] | $n_{SiO_2}$ [mol] | $n_{Al_2O_3}$[mol] | $n_{H_2O\ in\ (Me)CASH}$ |
|---|---|---|---|---|---|
| Ref_filtr | 0.920 | 0.000 | 1.000 | 0.025 | 1.331 |
| Co0.4 | 0.539 | 0.408 | 1.000 | 0.026 | 2.926 |
| Cu0.4 | 0.539 | 0.408 | 1.000 | 0.026 | 2.347 |
| Zn0.1 | 0.830 | 0.100 | 1.000 | 0.025 | 2.083 |
| Zn0.4 | 0.640 | 0.400 | 1.000 | 0.025 | 3.999 |

Table AP 8: Overview of Me-C-A-S-H solubility constants for gels with Me/Si molar ratios from zero to 0.4 Co and Cu as well as 0.6 for Zn.

| Chemical equation | log<sub></sub>$_{10}$ $K$ |
|---|---|
| | |
| $C_{0.92}A_{0.025}S_1H_{1.33} + 0.67\ H_2O \leftrightarrow 0.92\ Ca^{2+} + 0.05\ Al(OH)_4^- + 1\ SiO(OH)_3^- + 0.8\ (OH)^-$ | -8.3 |
| | |
| $Co_{0.05}C_{0.88}A_{0.025}S_1H_{1.35} + 0.6\ H_2O \leftrightarrow 0.86\ Ca^{2+} + 0.05Co^{2+} + 0.05\ Al(OH)_4^- + 1SiO(OH)_3^- + 0.82\ (OH)^-$ | -8.6 |
| $Co_{0.11}C_{0.86}A_{0.025}S_1H_{1.4} + 0.68\ H_2O \leftrightarrow 0.86\ Ca^{2+} + 0.11Co^{2+} + 0.05\ Al(OH)_4^- + 1SiO(OH)_3^- + 0.90\ (OH)^-$ | -9.5 |
| $Co_{0.16}C_{0.82}A_{0.025}S_1H_{1.42} + 0.67H_2O \leftrightarrow 0.82\ Ca^{2+} + 0.16Co^{2+} + 0.05\ Al(OH)_4^- + 1SiO(OH)_3^- + 0.91\ (OH)^-$ | -11.4 |
| $Co_{0.20}C_{0.76}A_{0.025}S_1H_{1.41} + 0.63\ H_2O \leftrightarrow 0.76\ Ca^{2+} + 0.2Co^{2+} + 0.05\ Al(OH)_4^- + 1SiO(OH)_3^- + 0.88\ (OH)^-$ | -10.2 |
| $Co_{0.25}C_{0.74}A_{0.025}S_1H_{1.43} + 0.64\ H_2O \leftrightarrow 0.75\ Ca^{2+} + 0.25Co^{2+} + 0.05\ Al(OH)_4^- + 1SiO(OH)_3^- + 0.94\ (OH)^-$ | -10.6 |
| $Co_{0.30}C_{0.73}A_{0.025}S_1H_{1,45} + 0.67\ H_2O \leftrightarrow 0.74\ Ca^{2+} + 0.3Co^{2+} + 0.05\ Al(OH)_4^- + 1SiO(OH)_3^- + 1.03\ (OH)^-$ | -11.3 |
| | |
| $Cu_{0.05}C_{0.9}A_{0.025}S_1H_{1.43} + 0{,}56\ H_2O \leftrightarrow 0.9\ Ca^{2+} + 0.05Cu^{2+} + 0.05\ Al(OH)_4^- + 1SiO(OH)_3^- + 0.86\ (OH)^-$ | -9.1 |
| $Cu_{0.11}C_{0.86}A_{0.025}S_1H_{1.52} + 0.52\ H_2O \leftrightarrow 0.86\ Ca^{2+} + 0.11Cu^{2+} + 0.05\ Al(OH)_4^- + 1SiO(OH)_3^- + 0.88\ (OH)^-$ | -9.7 |
| $Cu_{0.16}C_{0.83}A_{0.025}S_1H_{1.62} + 0.44\ H_2O \leftrightarrow 0.83\ Ca^{2+} + 0.16Cu^{2+} + 0.05\ Al(OH)_4^- + 1SiO(OH)_3^- + 0.92\ (OH)^-$ | -10.5 |
| $Cu_{0.20}C_{0.71}A_{0.025}S_1H_{1,72} + 0.27\ H_2O \leftrightarrow 0.71\ Ca^{2+} + 0.2Cu^{2+} + 0.05\ Al(OH)_4^- + 1SiO(OH)_3^- + 0.78\ (OH)^-$ | -10.1 |
| $Cu_{0.25}C_{0.69}A_{0.025}S_1H_{1.81} + 0.21\ H_2O \leftrightarrow 0.69\ Ca^{2+} + 0.25Cu^{2+} + 0.05\ Al(OH)_4^- + 1SiO(OH)_3^- + 0.84\ (OH)^-$ | -11.0 |
| $Cu_{0.30}C_{0.67}A_{0.025}S_1H_{1.91} + 0.14\ H_2O \leftrightarrow 0.67\ Ca^{2+} + 0.30Cu^{2+} + 0.05\ Al(OH)_4^- + 1SiO(OH)_3^- + 0.90\ (OH)^-$ | -11.6 |
| | |
| $Zn_{0.05}C_{0.88}A_{0.025}S_1H_{1.36} + 0.61\ H_2O \leftrightarrow 0.88\ Ca^{2+} + 0.05Zn^{2+} + 0.05\ Al(OH)_4^- + 1SiO(OH)_3^- + 0.82\ (OH)^-$ | -8.9 |
| $Zn_{0.11}C_{0.87}A_{0.025}S_1H_{1.40} + 0.65\ H_2O \leftrightarrow 0.87\ Ca^{2+} + 0.11Zn^{2+} + 0.05\ Al(OH)_4^- + 1SiO(OH)_3^- + 0.9\ (OH)^-$ | -9.6 |
| $Zn_{0.16}C_{0.81}A_{0.025}S_1H_{1.43} + 0.61\ H_2O \leftrightarrow 0.81Ca^{2+} + 0.16Zn^{2+} + 0.05\ Al(OH)_4^- + 1SiO(OH)_3^- + 0.88\ (OH)^-$ | -10.0 |
| $Zn_{0.20}C_{0.88}A_{0.025}S_1H_{1.46} + 0.70\ H_2O \leftrightarrow 0.88\ Ca^{2+} + 0.2Zn^{2+} + 0.05\ Al(OH)_4^- + 1SiO(OH)_3^- + 1.11\ (OH)^-$ | -11.3 |
| $Zn_{0.25}C_{0.75}A_{0.025}S_1H_{1.50} + 0.57H_2O \leftrightarrow 0.75\ Ca^{2+} + 0.25Zn^{2+} + 0.05\ Al(OH)_4^- + 1SiO(OH)_3^- + 0.94\ (OH)^-$ | -11.2 |
| $Zn_{0.30}C_{0.71}A_{0.025}S_1H_{1,53} + 0.56H_2O \leftrightarrow 0.71\ Ca^{2+} + 0.30Zn^{2+} + 0.05\ Al(OH)_4^- + 1SiO(OH)_3^- + 0.98\ (OH)^-$ | -11.9 |
| $Zn_{0.41}C_{0.64}A_{0.025}S_1H_{1.59} + 0.535H_2O \leftrightarrow 0.64\ Ca^{2+} + 0.41Zn^{2+} + 0.05\ Al(OH)_4^- + 1SiO(OH)_3^- + 1.05\ (OH)^-$ | -13.3 |
| $Zn_{0.51}C_{0.56}A_{0.025}S_1H_{1.66} + 0.49H_2O \leftrightarrow 0.64\ Ca^{2+} + 0.51Zn^{2+} + 0.05\ Al(OH)_4^- + 1SiO(OH)_3^- + 1.09(OH)^-$ | -13.8 |
| $Zn_{0.61}C_{0.46}A_{0.025}S_1H_{1.72} + 0.445H_2O \leftrightarrow 0.46\ Ca^{2+} + 0.61\ Zn^{2+} + 0.05\ Al(OH)_4^- + 1SiO(OH)_3^- + 1.09(OH)^-$ | -14.1 |